Investigation of the lower atmospheric wave forcing on the Mesosphere-Thermosphere-Ionosphere (MTI) system

A thesis submitted to

Department of Earth and Space Sciences,

Indian Institute of Space Science and Technology,
Thiruvananthapuram, India

in the partial fulfillment for the award of the degree of

Doctor of Philosophy (Ph.D.)

by

Reetambhara Dutta

National Atmospheric Research Laboratory, Gadanki, India

September, 2024

सत्यमेव जयते

भारतीय अंतरिक्ष विज्ञान एवं प्रौद्योगिकी संस्थान
(वि.अ.आयोग अधिनियम 1956 की धारा-3 के अधीन मानित विश्वविद्यालय घोषित)
भारत सरकार, अंतरिक्ष विभाग, वलियमला पोस्ट, तिरुवनंतपुरम 695 547 भारत

INDIAN INSTITUTE OF SPACE SCIENCE AND TECHNOLOGY
(A Deemed to be University u/s 3 of the UGC Act, 1956)
Government of India, Department of Space
Valiamala P. O, Thiruvananthapuram 695 547 India

www.iist.ac.in

Certificate

This is to certify that the thesis entitled **"Investigation of the Lower Atmospheric Wave Forcing on the Mesosphere-Thermosphere-Ionosphere (MTI) system"** submitted by **Ms. Reetambhara Dutta** (Reg. No: SC20D011) to the Indian Institute of Space Science and Technology, Thiruvananthapuram, in partial fulfillment for the award of the degree of Doctor of Philosophy, is a bonafide record of the research work carried out by her under our supervision. The contents of this thesis, in full or in parts, have not been submitted to any other Institute or University for the award of any degree or diploma.

Dr. S Sridharan

Supervisor

Dr. P R Sinha

Supervisor

Dr. Rama Rao Nidamanuri
Professor & HOD
Department of Earth and Space Sciences

Place: Thiruvananthapuram
Date: 30/1/2024

आईआईएसटी
IIST

Declaration

I declare that the thesis entitled " **Investigation of the Lower Atmospheric Wave Forcing on the Mesosphere-Thermosphere-Ionosphere (MTI) system**" submitted in the partial fulfillment of the degree of Doctor of Philosophy is a record of original work carried out by me under the supervision of Dr. S Sridharan and Dr. P R Sinha, and has not formed the basis for the award of any other degree or diploma, in this or any other Institution or University. In keeping with the ethical practice in reporting scientific information, due acknowledgments have been made wherever the findings of others have been cited.

Reetambhara Dutta

Thiruvananthapuram-695547

Reetambhara Dutta
(SC20D011)

This thesis is dedicated to my mother

Acknowledgement

My journey as a research scholar in the last four years would not have been possible without the aid of countless people who have extended unvacillating assistance and perpetual motivation in many respects. I take this opportunity to thank earnestly each one of them who helped me in the pursuit of my research.

With great pleasure and reverence, I would like to acknowledge the extraordinary debt I owe to my mentor Dr. S Sridharan, Scientist/Engineer-'SG', National Atmospheric Research Laboratory (NARL), India for worthwhile suggestions, consistent support and indefatigable encouragement, which has left an indelible indentation on my doctoral work. He has also been a benevolent guardian who has guided me in various ways right from the inception of my research career. I would also like to thank his family members for all the love and care they have given me during all these times.

I would like to express my cordial sense of gratitude to Dr. P R Sinha, Assistant Professor, Indian Institute of Space Science and Technology (IIST), India for his comments and suggestions.

I deem it a great privilege to express my cavernous sense of gratitude to Dr. A. K. Patra, Director, NARL who have afforded me an opportunity to pursue my research work in a safe and healthy environment with the excellent lab facilities. His scientific suggestions during academic reviews has truly been the most rewarding experiences of my life.

It is my great pleasure to express my deepest appreciation to Dr. S Unnikrishnan Nair, Director, IIST for providing necessary support and resources to accomplish my work.

I want to extend my sincere thanks to the academic and doctoral committees of NARL and IIST for monitoring my progress from time to time and providing necessary suggestions, which has led to further refinement in my work. I am extremely grateful to Dr. T. Narayan Rao, Dr. K. Raghunath, Dr. T. K. Ramkumar, Dr. Nirvikar Dashora, Dr. Venkat Ratnam, Dr. N. Venkateswara Rao, Dr. Amit P. Kesarkar, Dr. Jyoti Bhate, Mrs. Yashoda, Dr. T. V. C. Sharma, Dr. A Chandrasekar, Dr. Sayantani Ojha, Dr. Govindan Kutty M., Dr. Raju K George, Mr. Ravindra Devakate, Mr. Sreenivasa Guptha, Dr. N. Sreelatha and Mr. Venkatramana K. N. for all kind of cooperation. I *am also thankful to Department of Space, Government of India for the timely disbursal of my fellowship throughout my Ph.D. tenure.*

A debt of gratitude to all the data providers for making the data available in the public domain for the scientific community. I wish to thank the editor and reviewers of the journals for their valuable comments and suggestions. I would like to express my sincere gratitude to NSSS, URSI-RCRS, NCPS, IUGG, AGATA and TROPMET for providing me scientific platforms to present my research articles both nationally and internationally.

I am humbled to express my profound gratitude to my beloved schoolteachers, college and university professors for spending countless hours to prepare me for a better tomorrow.

A good friend is a lifetime achievement that adds on colorful pages in our lives. In this journey, I am truly fortunate to have met Donali, Santhosh,, Dr. Oindrila, Dr. Nanaji, Abhijeet, Dr. Kavita, Arun, Dr. Renju, Dr. Kasturi, Roshan, Amal, Dr. Sritam,, Alex, Dileep, Rohan, Rohit, Vanlalrochana, Krishnanunni, Veenus and Jinee. I am also extremely grateful to have my senior Dr. Meenakshi for her constant motivation. A special thanks to P Venkatesh for always having my back in every vicissitude of life.

Every morning I thank the divine power for blessing me with such beautiful parents, Mr. Biswajit Dutta and Mrs. Sabita Dutta. Words are not enough to inscribe their significance in my life. Thank you for believing in me every time and helping me in pursuing my dreams. My heartfelt thanks also goes to all my family members. Special thanks goes to Late Rama Rani Dutta, Late Amiya Ghosh, Late Anil Kumar Dutta, Mrs. Bimala Biswas, Mr. Pramatha Ranjan Biswas, Mrs. Mamata, Mrs. Jharna, Mrs. Susmita, Mrs. Kakoli, Mr. Tanmoy, Mr. Apurba, Dr. Pravabati, Mrs. Mallika, Mrs. Seema and also Anjana, Arpita, Asmita, Chandrima, Sristinil, Diptarka, Dyutipurba and Dyutipriya for their constant support, love and prayers. I am grateful to Shramana and Srijita for filling my life with selfless love and unconditional support right from my kindergarten days.

I bow and thank Almighty for all.

Reetambhara Dutta

Preface

The atmospheric region above stratopause that includes the combined effect of the complex interplay between the neutrals (mesosphere and thermosphere) and the ionized part of the atmosphere (ionosphere) is referred as the mesosphere thermosphere ionosphere (MTI) system. This region is modulated by the waves, having their source origin mostly in the lower and middle atmosphere. These waves in the course of their propagation (both vertically and horizontally) leads to the changes in the temperature, wind flow, concentrations of chemical constituents and ionospheric parameters in the different parts of the atmosphere. In this thesis, the global changes in the upper mesosphere lower thermosphere (UMLT) dynamics and the generation of low latitude ionospheric plasma irregularities in connection to the polar middle atmospheric events (Antarctic ozone hole and sudden stratospheric warming (SSW)) is investigated using ground-based, space-borne, model and reanalysis datasets.

The long term (2005–2020) meteor radar wind observations in the UMLT region over Rothera (67.5° S, 68.1° W) exhibit westward wind flow during October-November with large year-to-year variability during November-December of 2006–2011, 2015, 2018 and 2020, when the amount of ozone depletion is more in the southern high-latitude stratosphere. The 30 hPa ERA-5 reanalysis horizontal winds over 67.5° S also show large interannual variability in eastward winds during October-November of those years. It is observed that the presence of low meridional heat flux ($-\overline{V`T`}$) over 67.5° S in September, primarily due to Planetary wave (PW) of zonal wavenumber 1, decreases the polar stratospheric temperature. The reduced stratospheric temperature increases the catalytic destruction of ozone by enhancing the formation of polar stratospheric clouds (PSCs). The ozone loss leads to a large horizontal temperature gradient, which may generate strong stratospheric eastward wind with height due to thermal wind balance. It is suggested that the eastward winds may filter the upward propagating waves having westward phase speed and lead to the deposition of westward momentum into the background flow. The increased ozone loss also decreases the SW2 amplitude obtained from the Sounding of the Atmosphere using Broadband Emission Radiometry- Thermosphere Ionosphere Mesosphere Energetics and Dynamics (SABER-TIMED) temperature data at mesospheric heights. Therefore, the results provide an observational evidence for the impact of PW on the catalytic destruction of ozone during austral polar springtime, which leads to the changes in the circulation and tidal amplitude at the polar UMLT heights.

However, during summertime, the wind spectrum in both the polar regions is dominated by solar tides, compared to the PWs and gravity waves (GWs). The diurnal tidal (DT) amplitude exhibits summer enhancement and it also decreases with height. The PW and GW variances show enhancement only in winter and their variances increase with height. Significant correlations between the zonal wind and DT amplitude (−0.74 for Esrange and −0.54 and −0.77 for Rothera) indicate the possible relationship between DT and the mean background zonal flow. The summer maximum of migrating diurnal tide of zonal wavenumber 1 (DW1) over both 60° N and 60° S, similar to the DT variation, indicates that the DT is mostly composed of DW1. Since the DW1 tides propagate westward with the apparent motion of the sun, it is suggested that due to tidal-mean-wind interaction, it can deposit westward momentum into the background flow.

Next, analysis of the Kototabang (0.20º S, 100.3º E, 10.36º S dip latitude) Equatorial Atmosphere Radar (EAR) observations reveals a clear seasonal variation of the type-B 150 km radar echoes, with large percentage of occurrence (PO) during solar minimum year 2019, particularly during September 2019, which is accompanied by an austral Sudden stratospheric warming (SSW) event. The space–time spectral analysis of temperature data obtained from the SABER-TIMED satellite reveals that the dominance of SW2 tide during June-August, when the large PO of the 150-km echoes are observed Quasi-biennial variability of ozone vmr is also observed with larger values during 2017 and 2019. As per the Global Scale Wave Model (GWSM) results, the DW1 tides generated due to solar radiation absorption by stratospheric ozone and tropospheric water vapour have phases opposite to each other. This leads to the suppression of DW1 tide during September 2017 and 2019 and result in the relative dominance of SW2 tide over DW1 tide. The austral SSW of 2019 also resulted in increase of SW2 amplitude over equator because of ozone concentration enhancement and also decrease of DW1 amplitude owing to its interaction with the PWs, that enhances before SSW. The meridional wind shear associated with the relatively dominant SW2 tide may result in an interchange instability on the gradient of daytime descending intermediate ion layer. This plasma instability along with solar minimum conditions of 2019 might have led to high PO of these echoes during 2019.

The meteor radar observations over both the poles reveal the dominance of solar semi diurnal tide (SDT) in the polar UMLT region, compared to the lunar tides and its amplitude increases around the SSW onset days. Additionally, the semi-diurnal tide (SDT) shows a peak enhancement over the antipodes, few days after the onset of the boreal SSW 2013 and immediately after the onset time of the austral SSW 2019. However, no concurrent enhancement of stratospheric ozone is observed except for a gradual increase of PW activity, prior to the SDT enhancement. Moreover, the SDT amplitudes also reveal similar PW periodicity as observed in zonal wind. Therefore, it is suggested that a cross equatorial propagation of PW associated with the SSW events may modulate the solar SDT in the antipodal UMLT region that resulted in a peak in its amplitude after the SSW events.

Table of Contents

List of figures

List of tables

List of acronyms

AO:	Annual Oscillation
ACOM:	Atmospheric Chemistry Observations & Modeling
BDC:	Brewer Dobson circulation
CCM:	Chemistry Climate Model
CESM:	Community Earth System Model
CFC:	Chlorofluorocarbon
CGD:	Climate & Global Dynamics
CPC:	Climate Prediction Center
CPT:	Cold Point Tropopause
CSRT:	Clear Sky Radiative Tropopause
CTM:	Chemistry/Transport Models
DE3:	Eastward propagating non-migrating Diurnal tide with zonal wavenumber 3
DS0:	Diurnal Stationary tide
DT:	Diurnal Tide
DU:	Dobson Unit
DW1:	Westward propagating migrating Diurnal tide with zonal wavenumber 1
EAR:	Equatorial Atmosphere Radar
EEASC:	Equivalent Effective Antarctic Stratospheric Chlorine
ECMRWF:	European Centre for Medium-Range Weather Forecasts
EOS:	Earth Observing System

EPF:	Eliassen–Palm flux
FAI:	Field Aligned Irregularities
FUB CMAM:	Freie Universita¨t Berlin Climate Middle Atmosphere Model
GCM:	Global Climate Model
GMAO:	Global Modeling and Assimilation Office
GOES:	Goddard Earth Observing System chemistry
GOME:	Global Ozone Monitoring Experiment
GSFCDISC:	Goddard Space Flight Center Data and Information Services Center
GSWM:	Global Scale Wave Model
GW:	Gravity Wave
HAMMONIA:	Hamburg Model of the Neutral and Ionized Atmosphere
HAO:	High Altitude Observatory
HCFC:	Hydrochlorofluorocarbon
hPF or h’F:	Virtual height of the bottomside F layer
ICAO:	International Civil Aviation Organization
JPL:	Jet Propulsion Laboratory
LAPAN:	Lembaga Penerbangan dan Antariksa Nasional
LRT:	Lapse Rate Tropopause
MERRA:	Modern-Era Retrospective analysis for Research and Applications
MF:	Medium Frequency
MLS:	Microwave Limb Sounder
MSAO:	Mesopause Semi-annual Oscillation
NAD:	Nitricacid Dehydrate

NAM:	Northern Annular Mode
NAT:	Nitricacid Trihydrate
NCAR:	National Center for Atmospheric Research
NCEP:	National Centers of for Environmental Prediction
NEIS:	Naturally Enhanced Incoherent Scatter
NICT:	National Institute of Information and Communications Technology
NPP:	National Polar-orbiting Partnership
ODS:	Ozone Depleting Substances
OMI:	Ozone Monitoring Instrument
OMPS:	Ozone Mapping and Profiler Suite
PMC:	Polar Mesospheric Clouds
PNA:	Pacific-North American
PO:	Percentage of Occurrence
PRF:	Pulse Repetition Frequency
PV:	Planetary Vorticity
PW:	Planetary Wave
PSC:	Polar Stratospheric Clouds
QBO:	Quasi-Biennial Oscillation
RISH:	Research Institute for Sustainable Humanosphere
RTI:	Range Time Intensity
SABER:	Sounding of the Atmosphere using Broadband Emission Radiometry
SAM:	Southern Annular Mode
SAO:	Semi-Annual Oscillation

SBUV:	Solar Backscatter Ultraviolet Radiometer
SDT:	Semi Diurnal Tide
SEALION:	SouthEast Asia Low-Latitude Ionospheric Network
SNR:	Signal-to-Noise Ratio
SPARC:	Stratosphere-Troposphere Processes And their Role in Climate
SSAO:	Stratopause Semi-annual Oscillation
SSW:	Sudden Stratospheric Warming
STT:	Secondary Tropical Tropopause
STS:	Super cooled Ternary Solution
SW1:	Westward propagating non-migrating Semi diurnal tide with zonal wavenumber 1
SW2:	Westward propagating migrating Semi diurnal tide with zonal wavenumber 2
TIMED:	Thermosphere Ionosphere Mesosphere Energetics Dynamics
TOMS:	Total Ozone Mapping Spectrometer
TTT:	Tropical Thermal Tropopause
UARP:	UARS Reference Atmosphere Project
UARS:	Upper Atmosphere Research Satellite
UH:	Upper Hybrid
UMLT:	Upper Mesosphere Lower Thermosphere
UV:	Ultraviolet
VHF:	Very High Frequency
vmr:	Volume Mixing Ratio
WACCM:	Whole Atmosphere Community Climate Model
WMO:	World Meteorological Organization

List of publications

1. Dutta, R., Sridharan, S., Meenakshi, S., Ojha, S., Hozumi, K., Yatini, C. Y. (2022). On the high percentage of occurrence of type-B 150-km echoes during the year 2019 and its relationship with mesospheric semi-diurnal tide and stratospheric ozone. Advances in Space Research, 69, 80-95. https://doi.org/10.1016/j.asr.2021.08.031.

2. Dutta, R., Sridharan, S., Ojha, S. (2022). Impact of stratospheric planetary wave and ozone variabilities on the austral polar middle atmospheric circulation. Advances in Space Research, 69, 2976-2988 (2022). http://doi.org/10.1016/j.asr.2022.01.025.

3. Dutta, R. & Sridharan, S. (2023). Observational evidence for the influence of diurnal tide in driving winds in the polar upper mesosphere and lower thermosphere. Journal of Geophysical Research: Space Physics, 128(3), https://doi.org/10.1029/2022JA031104.

4. Dutta, R., Sridharan, S., Sinha, P. R. Signature of Sudden Stratospheric Warming in the Pole and its Antipode. (Manuscript under review in Journal of Geophysical Research: Space Physics).

Other collaborative research work

1. Midya, S. K., Pal, S., Dutta, R., Gole, P.K., Chattopadhyay, G., Karmakar, S., Saha, U., Hazra, S. (2021). A preliminary study on pre-monsoon summer thunderstorms using ground-based total lightning data over Gangetic West Bengal. Indian Journal of Physics, 95, p1–9 (2021). https://doi.org/10.1007/s12648-020-01681-y.

Conferences / Symposiums attended

1. **Oral: Impact of stratospheric ozone and mesospheric tides on enhanced occurrence of 150-km echoes in 2019** in 21st National Space Science Symposium (NSSS), 2022, organized by Indian Institute of Science Education & Research Kolkata, India.

2. **Oral: Impact of stratospheric planetary wave and ozone variabilities on the austral polar middle atmospheric circulation and tidal variabilities** in International Union of Radio Science-Regional Conference on Radio Science (URSI-RCRS), 2022, organized by Indian Institute of Technology, Indore, India.

3. **Poster: Observational evidence for the influence of stratospheric planetary wave and ozone variabilities on the middle atmospheric winds and tides over Antarctica** in National Conference on Polar Sciences (NCPS), 2023, organized by National Centre for Polar and Ocean Research, Goa, India.

4. **Oral: Observational evidence for the influence of stratospheric planetary wave on ozone variabilities and middle atmospheric circulation over Antarctica** in the 28th General Assembly International Union of Geodesy and Geophysics (IUGG), 2023, Berlin, organized by GFZ German Research Centre for Geosciences, Potsdam, Germany.

5. **Oral: Observational evidence for the influence of diurnal tides in driving the Arctic and Antarctic UMLT winds** in Antarctic Geospace and ATmosphere research (AGATA) kick-off meeting 2023, held during the 28th General Assembly International Union of Geodesy and Geophysics (IUGG) in Berlin, Germany.

6. **Oral: Observational evidence for the influence of diurnal tides in driving the polar UMLT winds** in National Symposium (TROPMET-2023), held during November 22-24, 2023 in Jaipur, Rajasthan, India. (**Received Best Paper Award**).

Chapter 1: Introduction

1.1. Vertical thermal structure of the atmosphere

The protective layer surrounding the surface of the earth, retained due to gravity, is known as the Earth's atmosphere. Vertically, it is divided into five layers viz., troposphere, stratosphere, mesosphere, thermosphere and exosphere, depending on the variation of temperature with height. Figure 1.1 depicts the vertical thermal structure of the global atmosphere, obtained from US Naval Research Laboratory mass spectrometer and incoherent scatter radar (NRLMSIS)® 2.0 model.

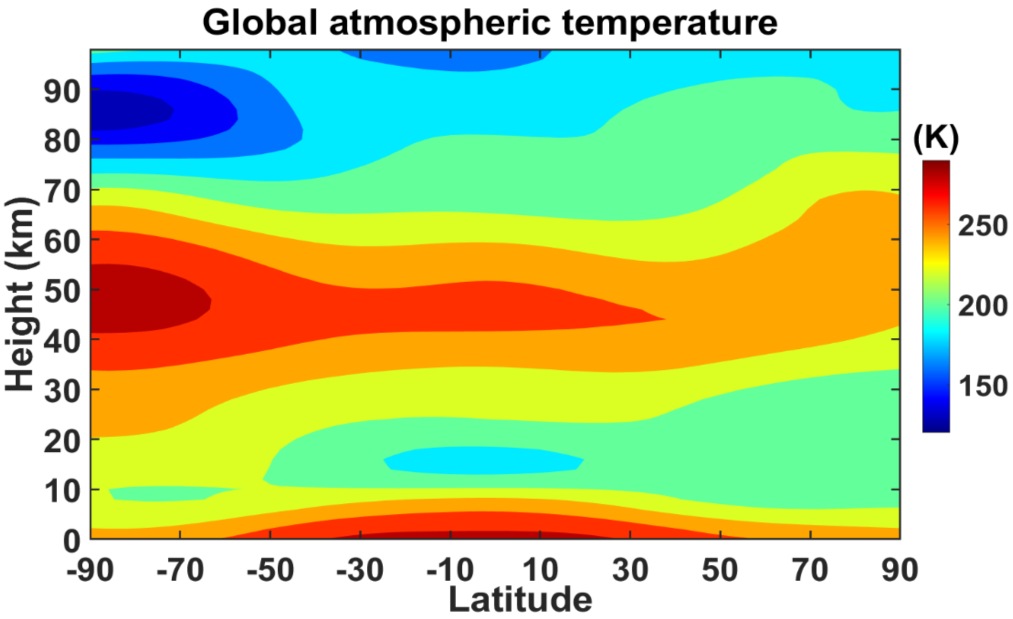

Figure 1.1: Latitudinal variation of temperature of earth's atmosphere obtained from NRLMSIS® 2.0 model

Troposphere

The lowermost part of the atmosphere where temperature decreases with height (6–7^{o}C / km in the lower part to 7–8^{o} C/km in the upper part) and extending from the surface to 16–18 km over tropics and 7–10 km over the poles is known as troposphere. Majority of the climatic and weather variability takes place in this region, as 99% of the water vapor of the atmosphere is there. Sometimes due to the presence of some shallow layers in troposphere, temperature inversion is observed, which inhibits vertical motions. The term 'troposphere' signifies turning or mixing because of the presence of vigorous convective air currents occurring within this layer. At the top of the troposphere, the temperature gradient is zero and the lapse rate becomes 2 K/km (as defined by World Meteorological Organization (WMO)). It is known as tropopause. The tropopause acts as a base of a large inversion layer between the troposphere and the stratosphere and therefore segregates two masses of air having distinct properties (Holton et al. (1995)). However, its height varies with latitude, season and on a day-to-day basis. The highest tropopause (above 18 km) is observed during summer monsoon time over South Asia and also over western equatorial Pacific (Mohanakumar, (2008)). Various terminologies are used to define tropopause, viz., lapse rate tropopause (LRT), cold point tropopause (CPT), tropical thermal tropopause (TTT), secondary tropical tropopause (STT), clear sky radiative tropopause (CSRT).

LRT: The tropopause in which the decrease of temperature is less than 2 K/Km, both in the tropics and extratropics.

CPT: It is identified by the minimum temperature.

TTT: It is in the tropics around 16-17 km.

STT: The level where the maximum convective outflow is observed (typically 11–12 km). Above this, the lapse rate is different from the moist adiabat, which depicts the temperature changes of saturated air on a Skew T-Log P chart, as it rises and cools due to adiabatic expansion.

CSRT: At this level, the clear sky heating becomes zero (typically 14-16 km).

Stratosphere

The second stratum of the atmosphere as one goes upward is the stratosphere, where temperature increases with altitude. It lies between tropopause and stratopause and its upper boundary reaches approximately 50 km where temperature peaks around 273 K. The importance of this layer lies in the fact that it contains a layer of ozone around 25–27 km, which protects the earth's surface by the absorption of harmful ultraviolet (UV) solar radiation. Absence of convection is observed in this layer because of its vertical temperature structure. Hence, air which enters the stratosphere from troposphere remains there stably for months/years. However, horizontal mixing occurs here more hastily than vertical mixing. Also, the water vapor content of this layer is low due to which clouds are rarely seen in this region. Although **i**n the polar winter stratosphere polar stratospheric clouds (PSCs) or mother-of-pearl clouds or nacreous clouds are found, which is one of the essential components facilitating ozone loss over the polar stratosphere.

Mesosphere

Above stratosphere, there exists the third layer of the atmosphere between 60 km to 90 km, known as the mesosphere. Similar to the troposphere, decrement of temperature with altitude is observed in this layer because of the radiative cooling by CO_2 molecules present there. The lowest temperature of the earth is found at the top of the mesosphere, where temperature drops as low as 150 K. This cold temperature therefore sublimates the very little water vapor present in this region into polar-mesospheric clouds (PMCs) or noctilucent clouds. This layer also gained prominence as it burns up the meteors due to friction with the earth's atmosphere. Therefore, abundance of some metallic constituents like Fe+, Mg+, Na+, K+, Ca+, etc. can be found in this region (Krankowsky et al. (1972)). However, this particular region of earth's atmosphere is difficult to study as it is very high for the aircrafts or weather balloons to reach and too low for satellites to accurately monitor this region.

The term 'middle atmosphere' basically defines the combination of these two layers, stratosphere and mesosphere and it extends approximately from 10 km to 100 km.

Thermosphere

The layer above mesosphere is the thermosphere where temperature again increases with height. From 90 km, thermosphere can extend to between 500 km and 1000 km. Absorption of X-rays and ultraviolet (UV) radiation occurs in this region, which causes dissociation of Nitrogen and Oxygen molecules forming electrically charged ions. Temperature in the thermosphere can be as high as 500^{o} C to 2000^{o} C. Both the space shuttle and International Space Station orbits in the thermosphere. The colorful Auroras (Northern and Southern Lights) are also observed in this layer (80–160 km).

The atmosphere below the thermosphere is well mixed due to turbulent mixing of air. So it is occasionally referred to as 'homosphere'. However, the increase of mean free path of the molecules in the thermosphere due to its little density leads to the deposition of heavier molecules in the lower thermospheric part and the lighter ones on its top (Mohanakumar, (2008)). Therefore, this region is also known as 'heterosphere'.

Exosphere

Above thermosphere, the layer where atmospheric density is the least, and which consists of mostly lighter gases like Hydrogen and Helium that can sometimes escape the earth's gravity, is known as exosphere. Exosphere has no clear outer boundary as it gradually fades up to space.

There is another classification of the earth's atmosphere, that is, the neutral atmosphere and the ionosphere. The ionosphere consists of ions and electrons. It starts at 60 km covering parts of mesosphere, thermosphere and exosphere and it is classified into D (60–90 km), E (90–120 km) and F (120–500 km) layers. The F layer is further classified as F_1 and F_2 layers. At night, the D and F_1 layers vanish in absence of sunlight. Above the altitude of the daytime peak electron density to the bottomside of the F region, there is a region observed in the geographical and magnetic equatorial ionosphere, known as the 'ionospheric valley region'. It acts as a boundary between the terrestrial and space weather domain that demonstrates a complex interplay of the electrodynamics, neutral dynamics, and photochemistry. The ionospheric valley region is important to study using rocket (in-situ) experiments and very high frequency (VHF) radar observations as the valley region irregularities such as the daytime 150 km radar echoes are observed over here.

1.2. Vertical structure of atmospheric pressure and density

In the atmosphere, there is a variability of pressure and density with height. Atmospheric pressure is defined as the force exerted per unit area on a surface by a mass of air present above it. Mathematically it is represented as

$$P = Po\ exp(-z/H) \tag{1.1}$$

where P= atmospheric pressure at height z above sea level, P_0= Atmospheric pressure at sea level and H= atmospheric scale height (8.4 km for earth). The equation is only valid for an isothermal atmosphere.

Atmospheric density is defined as the concentration of molecules present in a given volume of air. Both of them decreases exponentially with the increase in altitude and therefore density follows same mathematical equation 1.1.

As per the International Civil Aviation Organization (ICAO), the standard atmospheric sea level pressure is 1013.2 hPa and sea level density is 1.225 kg/m^3.

1.3. Wind structure of the atmosphere

1.3.1. Lower atmospheric wind circulation

In addition to the vertical temperature variability of the atmosphere, the latitudinal temperature difference causes surface pressure differences, which ultimately results in wind flow from tropics to the poles. The amount of heat received at the surface of the earth due to the differential latitudinal solar heating leads to higher temperature over the equator and lower over the poles. The presence of Coriolis force (owing to rotation of earth) then deflects the wind to the right in the Northern hemisphere and to the left in the Southern hemisphere.

Without earth’s rotation and its land-sea contrast, there would have been a single air circulation cell in each hemisphere. However, the rotation of earth as well as the unequal distribution of land and water bodies, there arose a complicated three-cell pattern that exists over each hemisphere. The cells are named as the Hadley cell, the Ferrel cell and the Polar cell as shown in Figure 1.2.

Hadley cell

Air rises over the equator because of the maximum incoming solar radiation received by this region. It then moves poleward at high altitude (12–15 km), descends over the region of subtropics to even mid latitudes (~30^0 latitude). The descended air finally flows towards the equator over the surface (as trade winds).

Ferrel cell

This is the mid-latitude circulation caused by friction and not by temperature. Air in this cell flows opposite to the Hadley cell and it extends between 35° and 60° N/S.

Polar cell

Due to the extreme cold temperature, the cold dense air descends over the poles and moves towards the equator over surface and finally rises up over the subtropics (60^0 latitude) as it warms up. The risen warm air again returns to the poles at high altitude.

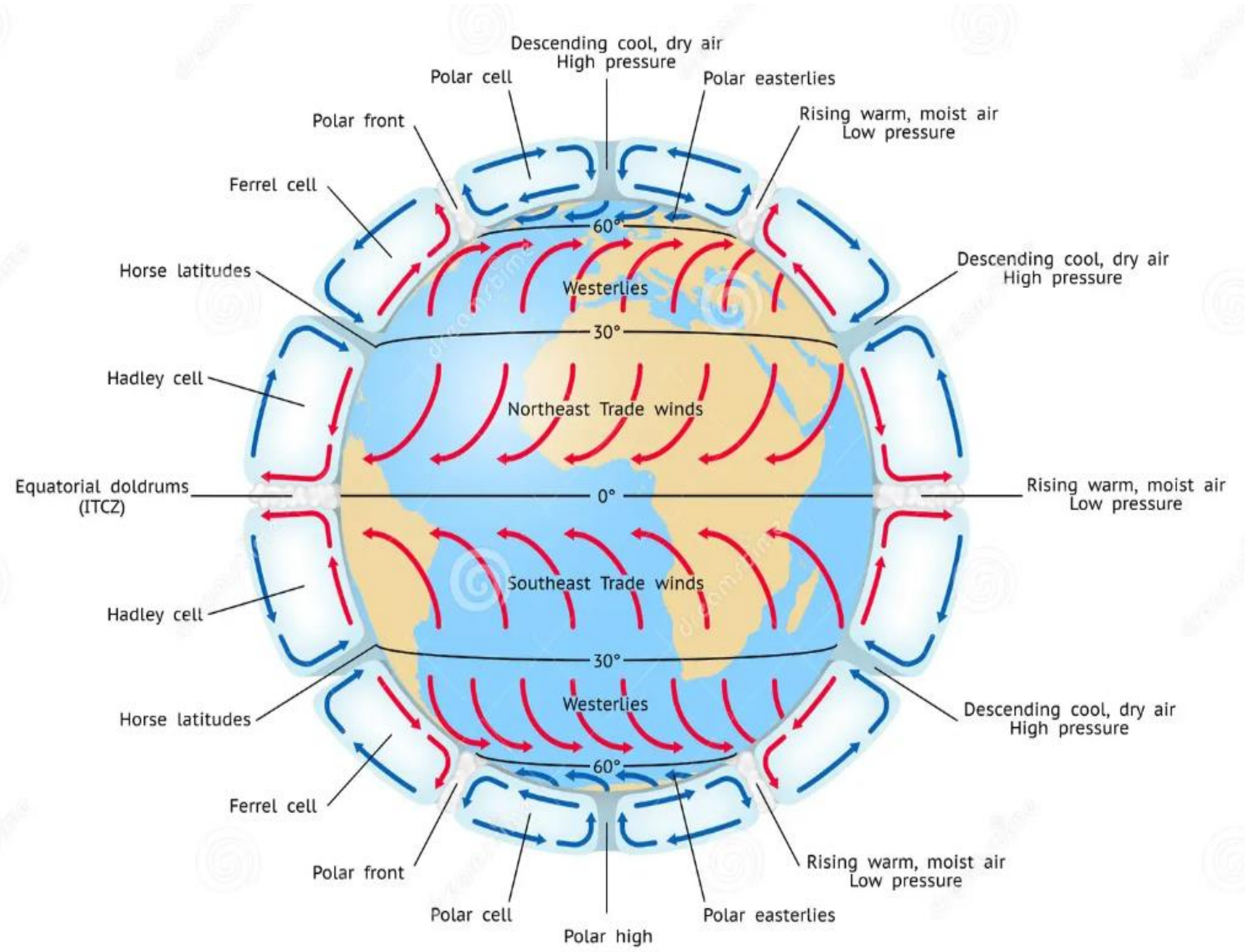

Figure 1.2: Global atmospheric circulation in lower atmosphere (https://www.pinterest.com)

The presence of these circulation cells leads to the formation of semi-permanent areas of high and low pressure on the earth's surface. Therefore, the low pressure belts (equator and subtropics) receive much rainfall compared to the high pressure belt (tropics and poles).

1.3.2. Middle atmospheric wind circulation

The circulation of the middle atmosphere is different from that of the lower atmosphere. The equatorial latitudes are dominated by Quasi Biennial Oscillation (QBO) and Semi-annual Oscillation (SAO), whereas the high latitude wind circulation is governed by Annual Oscillation (AO).

Quasi-Biennial Oscillation

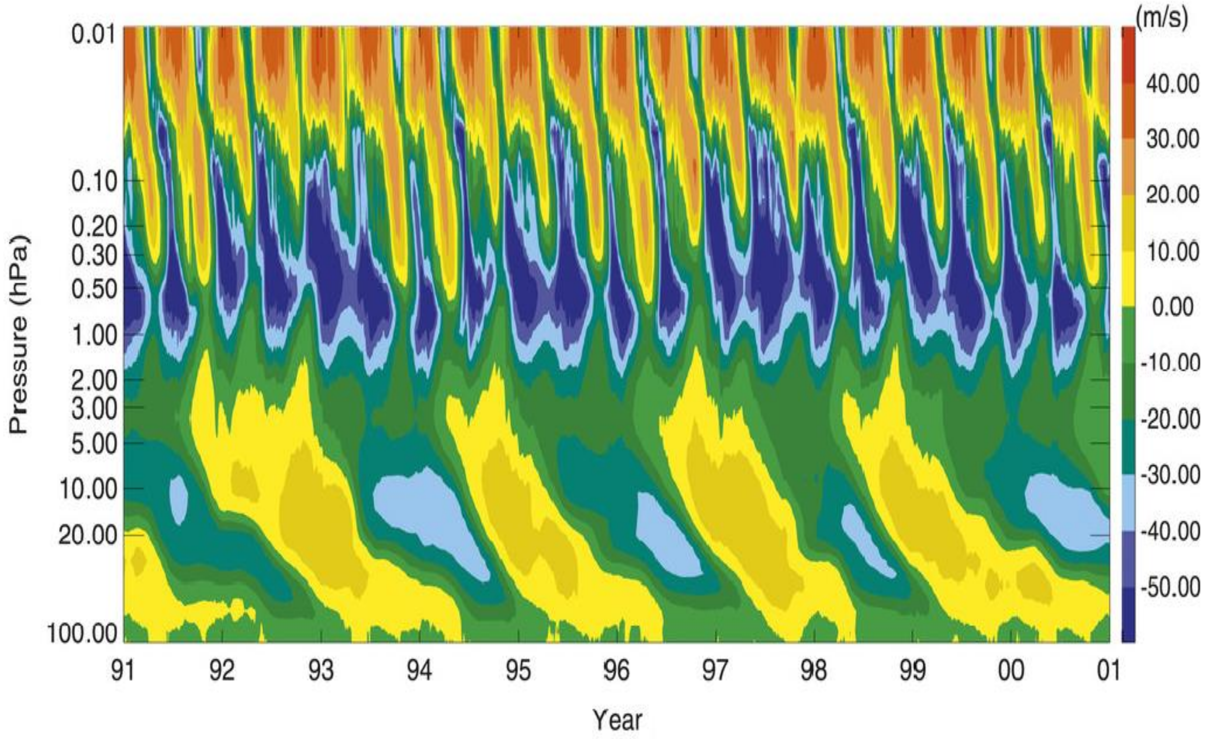

Figure 1.3: Equatorial middle atmospheric winds as per the control run of the climate chemistry model (Reproduced from Shu et al., 2013)

The east west wind oscillation in the stratosphere, that is, the alteration of easterly and westerly winds which is observed every 20–30 months in the tropical stratosphere, extending between 10–

15º latitude on either side of the equator, is known as QBO. Vertically, it is observed between 100 hPa and 2 hPa (Hamilton et al. (2004)). Winds in the QBO descend downward with a speed of 1 km/ month and gradually dissipate in the tropopause region. Atmospheric waves emanating from troposphere and dissipating in the stratosphere, drives the QBO. Easterlies in the QBO possess a wind speed of 30 m/s as observed in Figure 1.3, whereas the westerlies are comparatively weaker (20 m/s). The QBO can be observed in temperature also. The peak amplitude of QBO in zonal winds is observed around 30 km, whereas for temperature it is seen around 25 km (Mohanakumar, 2008).

The QBO affects the interannual variability of total ozone over the tropics. However, its impact can be observed far away from the equator. During Northern Hemispheric winter, the QBO affects the extratropical stratosphere when the planetary wave amplitudes are larger. The easterly phased winds weaken the jet streams, leads to sudden stratospheric warming (SSW) and can cause colder winters in Northern Europe.

Semi-annual Oscillation

Two-year reversal in wind patterns observed in the upper stratosphere and mesosphere extending 30º latitudes on either side of the equator is known as SAO. The SAO near stratopause is known as Stratopause Semi-annual Oscillation (SSAO) and near mesopause is known as Mesopause Semi-annual Oscillation (MSAO). Figure 1.3 illustrates the time series of the zonal-mean zonal winds between 5° S and 5° N, clearly representing the QBO, SSAO and MSAO. The SSAO is out of phase with the MSAO. The SAO is mostly generated due to momentum advection and not by changes in solar declination angles. Particularly, the equatorial westward phase of it is generated by eddy momentum deposition changes to the zonal winds and it occurs after the equinox months (Mohanakumar, (2008)). The QBO amplitude increases in the lower stratosphere and becomes stronger around 30 km and then again decreases in upper stratosphere. However, for SAO, its amplitude is less in the lower and middle stratosphere and it increases in the upper stratosphere. Therefore, the SAO and QBO are also out of phase. It is also observed that the peak amplitude of SAO in temperature at 40 km is much higher than that of QBO at 25 km. The effects of SAO can also be observed in the mean concentration of several long-lived chemical species (like N_2O, CH_4) in the stratosphere.

Annual oscillation

In the extratropical latitudes, the air circulation is dominated by the annual oscillation (AO) in which winds become easterly in summer hemisphere and westerly in winter hemisphere. The maximum westerly (80 m/s) and easterly (50 m/s) winds are observed at 65 km over 40º latitudes. For northern hemisphere, the transition from westerly to easterly winds is observed in the month of May and the reversal during September. The wind change is also observed to start at high latitude and altitude, from where it descends to tropics. Figure 1.4 shows the monthly mean wind velocity covering 0–85 km height combining data for the time period 1992–1997 obtained from the Upper Atmosphere Research Satellite (UARS) Reference Atmosphere Project (URAP).

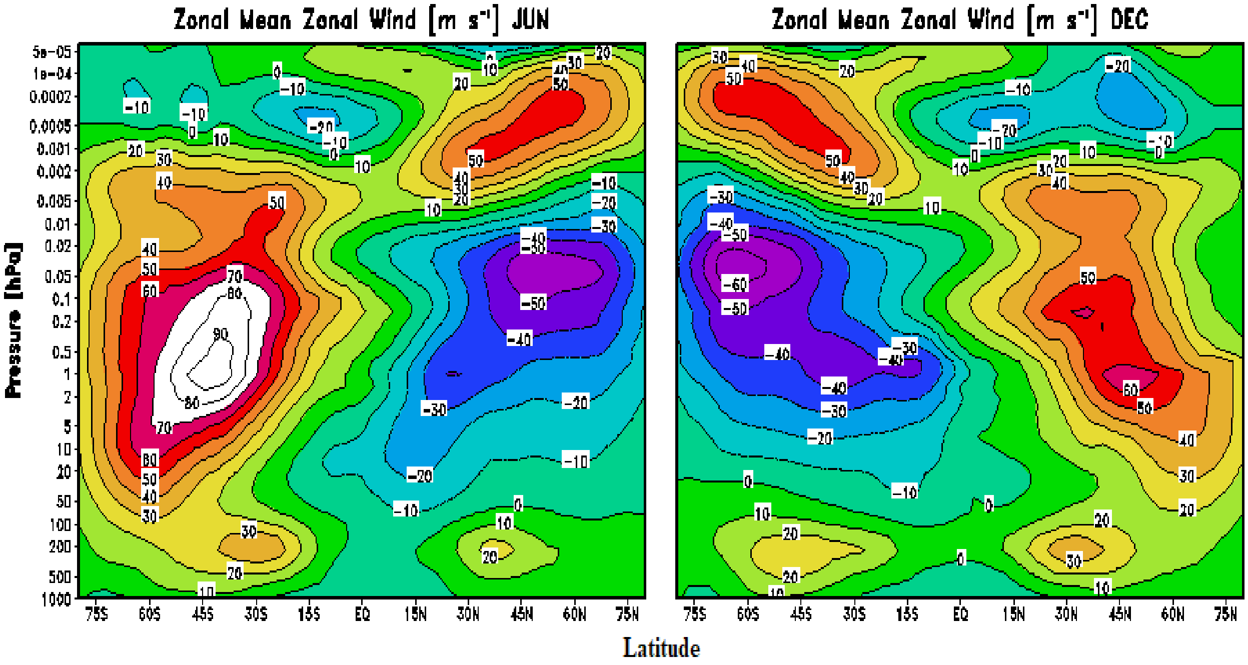

Figure 1.4: Zonal wind observations as a function of height and latitude (https://www.sparc-climate.org)

1.4. Chemical structure of the atmosphere

Although the earth's atmosphere extends up to thousands of miles from earth's surface and comprises of several gaseous constituents like nitrogen (N_2), oxygen (O_2), water vapor (H_2O), Argon (Ar), carbon dioxide (CO_2), etc, the abundance of the gases is mostly observed in the lowest 30 km from the earth's surface. The percentage volume of these gaseous constituents are listed in the following Table 1.1.

Gas	**Chemical Formula**	**Volume (%)**
Nitrogen	N_2	78.084
Oxygen	O_2	20.947
Argon	Ar	0.934
Water vapor	H_2O	0 to 4
Carbon dioxide	CO_2	0.035
Neon	Ne	0.00181
Helium	He	0.000524
Methane	CH_4	0.00017
Krypton	Kr	0.000114
Hydrogen	H_2	0.000053
Nitrous oxide	N_2O	0.000031
Carbon monoxide	CO	0.000010
Xenon	Xe	0.000009
Ozone	O_3	0.000007
Nitrogen dioxide	NO_2	0.00002
Iodine	I_2	0.00001

Table 1.1: Volumetric composition of gases present in Earth's atmosphere

In the context of middle atmosphere, the major two gases discussed in this thesis are ozone and water vapor.

1.4.1. Ozone

Majority (90%) of the total ozone of the atmosphere resides in the stratosphere as ozonosphere or ozone layer, which absorbs the harmful UV radiation emitted from the sun. The following tables classifies the UV radiation reaching the earth based on its wavelength and its impact to human life.

UV	Wavelength (nm)	Effect
UV-C	200-280	Extremely harmful → Damages DNA
UV-B	280-315	Harmful → Sunburn, skin cancer
UV-A	315-400	Less harmful → Skin related damage, premature aging, wrinkles

Table 1.2: Different types of UV radiation and its effects on life

The stratospheric ozone completely absorbs UV-C and most of the UV-B, thereby playing a significant role in protecting the life of this planet by preventing the entry of harmful solar radiation reaching the earth's surface. Although the remaining 10% of the total atmospheric ozone is present in the troposphere, which has an adverse effect on life. Tropospheric ozone reacts with several other molecules and negatively affects the environment as well as public health. Hence, it is important to monitor the ozone in different levels of the atmosphere on a regular basis and know its formation and depletion mechanisms.

Reactions of stratospheric ozone formation and depletion

Ozone is formed naturally in the stratosphere by the photolysis of molecular oxygen. The mechanism was first proposed by Sidney Chapman in 1930s.

Chapman mechanism

$$O_2 + h\upsilon \rightarrow O + O \quad (\lambda \sim 180\text{–}240 \text{ nm}) \qquad (1.1)$$

$$O + O_2 + M \rightarrow O_3 + M \qquad (1.2)$$

where M is a third body (mostly N_2 or O_2).

The ozone which is formed can be further recycled naturally when it reacts with a photon to form molecular oxygen.

$$O_3 + h\upsilon \rightarrow O_2 + O\ (O^1D,\ \lambda < 300\ \text{nm or } O^3P,\ \lambda > 325\ \text{nm}) \tag{1.3}$$

$$O + O_3 \rightarrow 2\ O_2 \tag{1.4}$$

Latitudinal and seasonal ozone variability

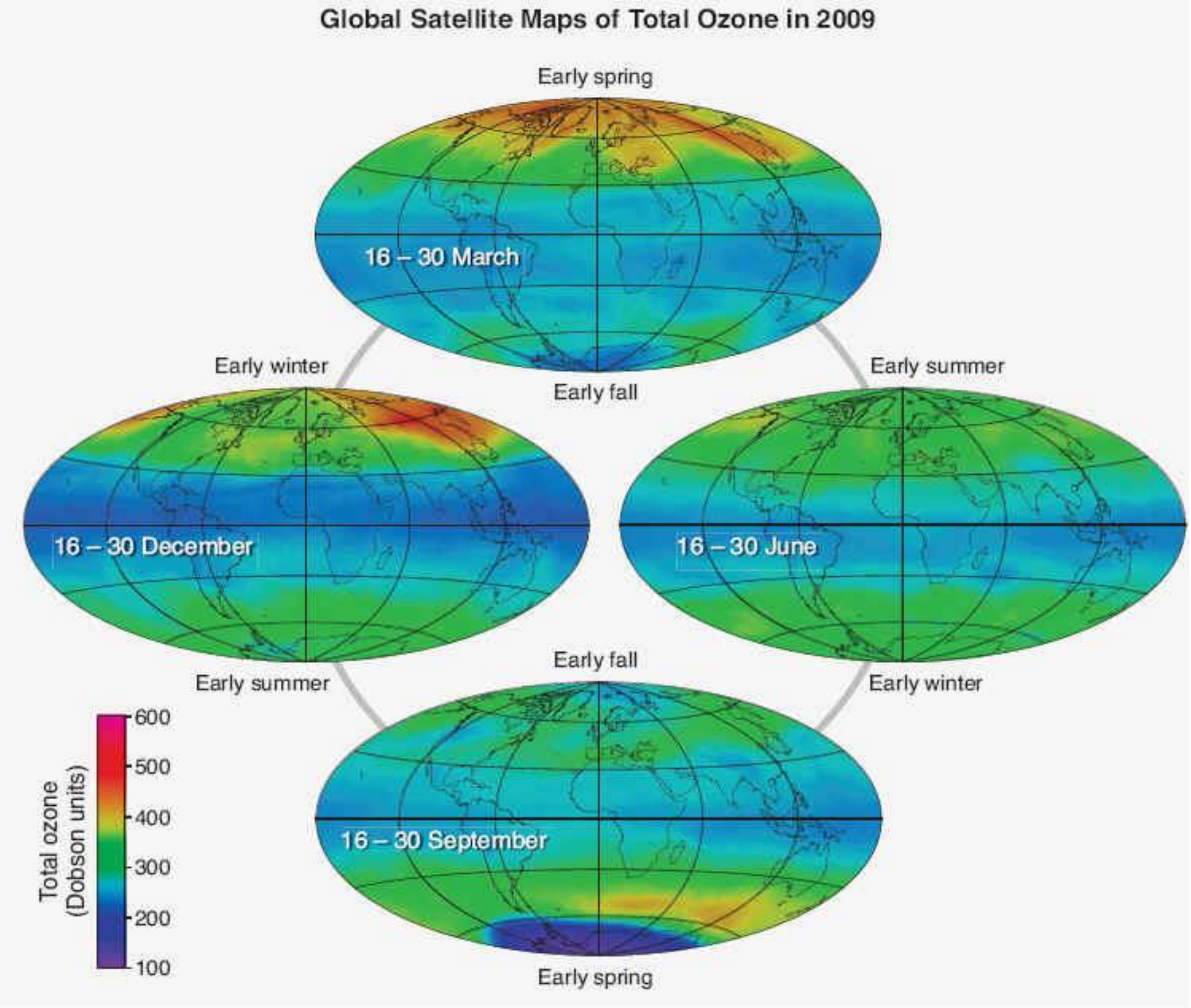

Figure 1.5: Global ozone distribution in different seasons (https://www.theozonehole.org)

Although the Chapman cycle provides the mechanisms, by which ozone is formed and destructed naturally in the atmosphere, yet it lacks to explain the total amount of ozone present globally in different seasons. Models based only on the Chapman mechanism overestimates stratospheric ozone. This is because the Chapman chemistry does not mention the reactions that involve halogens for ozone destruction. Therefore, it was suggested that the additional destruction of O_3 occurs through catalytic cycles (HO_x, NO_x, ClO_x, BrO_x). The following reactions demonstrates ozone destruction occurring through the above mentioned cycles.

HO_x, NO_x, ClO_x, BrO_x cycles:

$$O_3 + X \rightarrow XO + O_2 \tag{1.5}$$

$$XO + O \rightarrow X + O_2 \tag{1.6}$$

$$\text{Net: } O_3 + O \rightarrow 2\,O_2 \tag{1.7}$$

where X = OH, NO, Cl, Br.

Secondly, there exists an equator-to-pole 3D circulation know as Brewer Dobson circulation (BDC), which transports chemical species like ozone from their photochemical production region to the poles. The BDC involves the rising motion in the topics from troposphere to stratosphere (approximately for more than 6 months), then its poleward transport and finally the downward motion in the mid (transported to troposphere) and high (transported up to lower stratosphere) latitudes. In addition to the ozone transport, the BDC also explains why there is lack of water vapor in the stratosphere.

Total ozone also varies with seasons. The changes are much more prominent over the poles compared to the tropics. Springtime ozone maxima is seen poleward of 45° N and between 45° and 60° S in the Northern and Southern hemispheres respectively because of the increased transport of tropical ozone during late autumn and winter (Sato and Hirano, (2019)).

The transport also has an interhemispheric difference. It is however much stronger in Northern hemisphere than in the Southern hemisphere because of the larger planetary wave activity observed in the Northern hemisphere owing to large land sea orographic constant. The seasonal and latitudinal ozone variability is shown in Figure 1.5.

1.4.2. Water vapor

The most abundant greenhouse gas, which is responsible for majority (30–60%) of greenhouse effect due to trapping of heat, is the water vapor. Its major sources are the evaporation from water bodies, transpiration from plants and major sink is its condensation in clouds. Water vapor is a function of air temperature, so hot air is seen to hold more moisture compared to cold air. It has a shorter lifetime compared to other greenhouse gases. The vertical profile of water vapor shows that its average concentration decreases with altitude and it has two main sources in stratosphere. In the upper stratosphere, the high water vapor concentration is due to its formation by methane oxidation. However, in the lower stratosphere, it enters stratosphere from tropical troposphere via cold tropopause, where it dries at around 3.5–4 ppmv. The dominant source of water vapor in the tropical and subtropical upper troposphere is the Hadley circulation and the Walker circulation. In the mid and high latitudes upper troposphere, moisture is supplied from the tropics by convection or extratropical cyclones. Even the lower stratosphere is moistened by horizontal transport across the subtropical tropopause, which is stronger in summer. From the late 20th century, an increasing trend in the stratospheric water vapor has been observed as a response to climate change. It can lead to stratospheric cooling to a similar value if there is stratospheric ozone loss (Forster and Shine, (1999), Smith et al, (2001)).

In addition to the greenhouse effect, water vapor is a source of hydroxyl radical (OH). This hydroxyl radical acts as a sink for several other greenhouse gases (CH_4, HCFCs and HFCs) and several pollutants (CO and non-methane hydrocarbons).

$$O^1D + H_2O \rightarrow 2OH \tag{1. 8}$$

Further, if the amount of stratospheric water vapor increases, it can lead to more polar stratospheric cloud formation, in presence of nitric acid (HNO_3) and sulfuric acid (H_2SO_4). Since PSCs provide the surface on which chlorine depletes ozone, thus increase in stratospheric water vapor can enhance polar ozone depletion processes in polar springtime.

1.5. Important middle atmospheric events

1.5.1. Ozone hole

The gradual reduction of ozone concentration in the polar stratosphere during springtime is known as ozone hole/loss/depletion. Particularly, the term ‘hole’ is used as a metaphor to define the areas where the ozone concentration drops to below 220 Dobson Unit (DU). Due to the increased industrialization from the 1950s, there has been increased production of ozone depleting substances (ODSs) like chlorofluorocarbons (CFCs), hydrochlorofluorocarbons (HCFCs), carbon tetrachloride, methyl chloroform, halons and methyl bromide. These ODSs are very stable in the troposphere and because of their longer lifetime, they are gradually uplifted to the stratosphere. In presence of strong UV radiation in the stratosphere, these ODSs are disintegrated to release halogens (Cl, Br etc). However, the halogen (mostly Cl) freed from the ODS doesnot immediately destroy ozone by reacting with it. Instead, it is converted to long-term reservoirs of chlorine (HCl or $ClONO_2$). These long-term reservoirs, being very stable, are then shifted gradually towards the polar regions.

Over the poles, the presence of circumpolar westerlies, popularly known as polar vortex, isolates the cold polar air from rest of the globe. Under this unusual cold temperature in winter (below 200K), the PSCs are formed, which provides the surface on which the long-term chlorine reservoirs are converted to more active forms of chlorine, like Cl_2 (Solomon et al. (1986)). The PSCs are classified into Type I and II PSCs, based on temperature and chemical composition. The Type I PSC is formed at temperature like 196K. They are further subdivided into Type Ia (crystalline) and Type Ib (liquid). The chemical composition of Type Ia is $HNO_3.3H_2O$ (Nitricacid trihydrate (NAT)) or $HNO_3.2H_2O$ (Nitricacid dehydrate (NAD)) and Type Ib is $H_2O/HNO_3/H_2SO_4$ (super cooled ternary solution (STS)). The Type II PSC is formed approximately below 188 K as ice crystals. The reactions involving the conversion of chlorine from its inactive to active form involving the different kind of PSCs are listed below.

$$ClONO_2 + HCl \rightarrow Cl_2 + HNO_3 \text{ (Type I and II)} \quad (1.9)$$

$$ClONO_2 + H_2O \rightarrow HOCl + HNO_3 \text{ (Type II)} \quad (1.10)$$

$$HOCl + HCl \rightarrow H_2O + Cl_2 \text{ (Type I and II)} \quad (1.11)$$

Now on the arrival of spring, the Cl_2 breaks apart to release Cl, which reacts extensively with the stratospheric ozone and therefore depletes the ozone layer (Molina and Molina, (1987), Solomon, (1999)). Approximately one chlorine atom has the ability to destroy 1,00,000 ozone molecules.

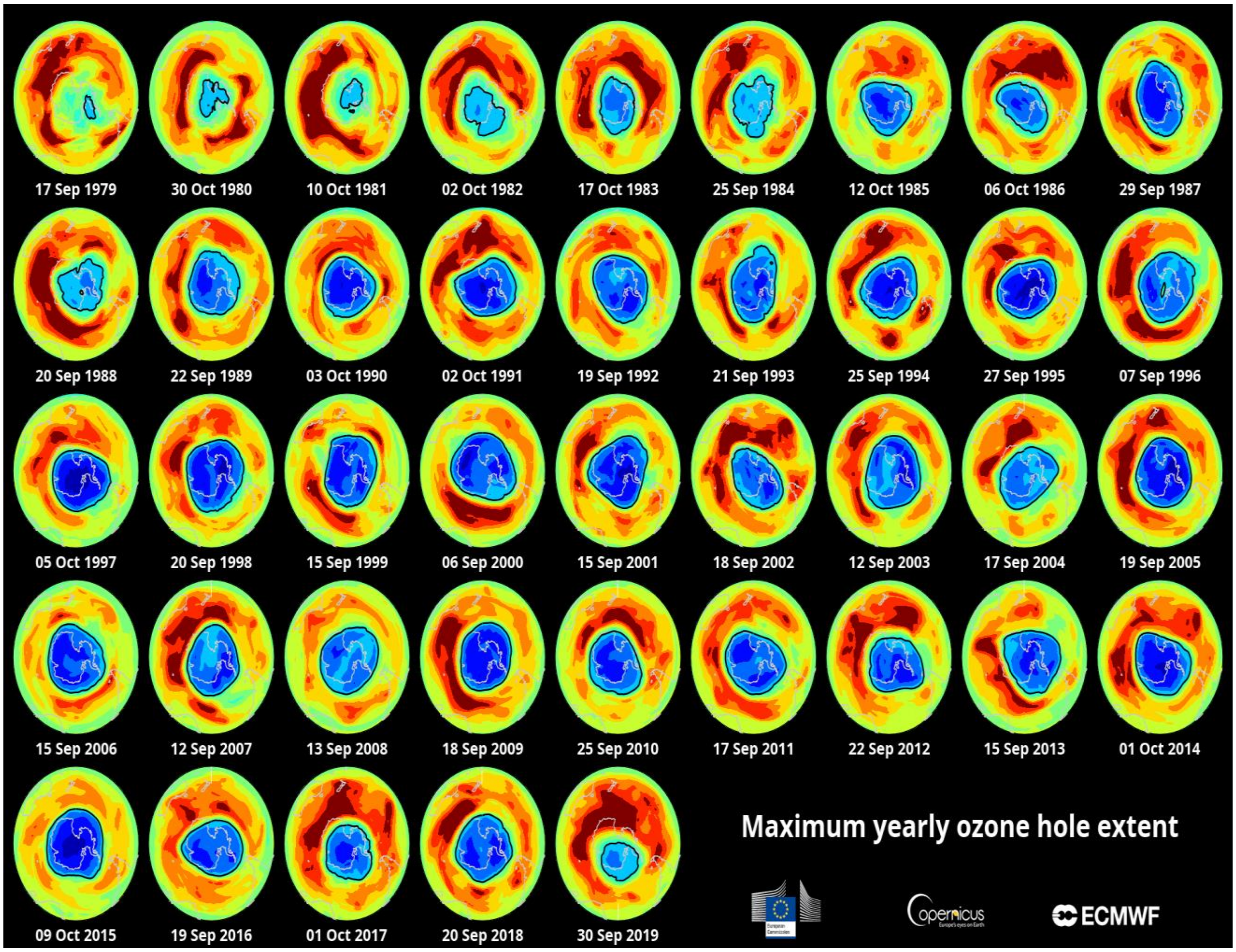

Figure 1.6: Antarctic ozone hole on the days with the lowest ozone concentrations (Credit: Copernicus Atmosphere Monitoring Service)

The ozone hole is observed over the Antarctic in all the years. The Antarctic maintains the extreme low stratospheric temperature owing to its stronger polar vortex. This is because of the weaker wave activity observed over the Southern hemisphere due to lack of land sea contrast, which helps in retaining the stability of the Antarctic polar vortex. Thus, the colder temperature inside the vortex results in the increased formation of PSCs over there, which are the key to the loss process. Even the Type II PSC, which are formed only below 188 K, are found only in the Antarctic. This leads to the abundance of free chlorine atoms over the Antarctic stratosphere that forms the ozone hole. Figure 1.6 depicts the Antarctic ozone hole on the days in which the lowest ozone concentrations were recorded. Ozone hole can be measured by several ozone loss metrics named as ozone hole area, ozone minimum, ozone mass deficit, polar cap ozone, defined as follows

Ozone hole area: It represents the area where the total column values of ozone obtained from the satellite measurement drops below 220 DU due to anthropogenic activity, located to the south of 60º S.

Ozone minimum: It is defined as the minimum value of columnar ozone obtained from the satellite measurement, again to the south of 60º S.

Ozone mass deficit: Its value is determined from the total column ozone that combines effects of the ozone hole area changes and its depth.

Polar cap ozone: It is defined as the averaged total columnar ozone surrounding the polar cap to the south of 63ºS. It combines the satellite measurements and model results.

The impact of polar ozone loss on atmospheric circulation extends from the earth's surface to the UMLT region. Using a set of chemistry-climate models, Son et al. (2010) showed that stronger austral ozone loss processes can result in the enhanced poleward displacement of tropospheric midlatitude jet and its intensification. It can also lead to increased expansion of summertime Southern Hemispheric Hadley cell. Using Whole Atmosphere Community Climate Model (WACCM) simulations, several studies have shown that the changes in the propagation of GW associated with the ozone loss processes that governs the background wind field, can warm the polar mesosphere and cool the lower thermosphere (Smith et al. (2010), Smith, (2012)). Additionally, simulation study by Lubis et al. (2016) shows the contribution of PW (k = 1–3) in generating warming in the mesosphere. They also demonstrated that the radiative effects arising due to the increased greenhouse gases associated the ozone hole can lead to cooling of the lower thermosphere.

However, with the implementation of Montreal Protocol and its amendments, Newman et al. (2006) showed that by 2068, the complete recovery of the ozone hole can be expected. Recent study by Pyle et al. (2022) anticipated the ozone recovery (at least to its historic threshold as that of 1960) to be around mid-2070s as shown in Figure 1.7. The black line in the Figure represents the value of the total columnar ozone based on chemistry climate model (CCM) calculation, if the Montreal Protocol is followed. The blue curve represents the scenario if some additional emissions of a long-lived ODS occur. The red curve denotes the emission of a short-lived halocarbon. They mentioned that the recent threat to the ozone hole could be attributed to either illegal breaches of the Montreal Protocol or the emissions of short lived species of anthropogenic origin.

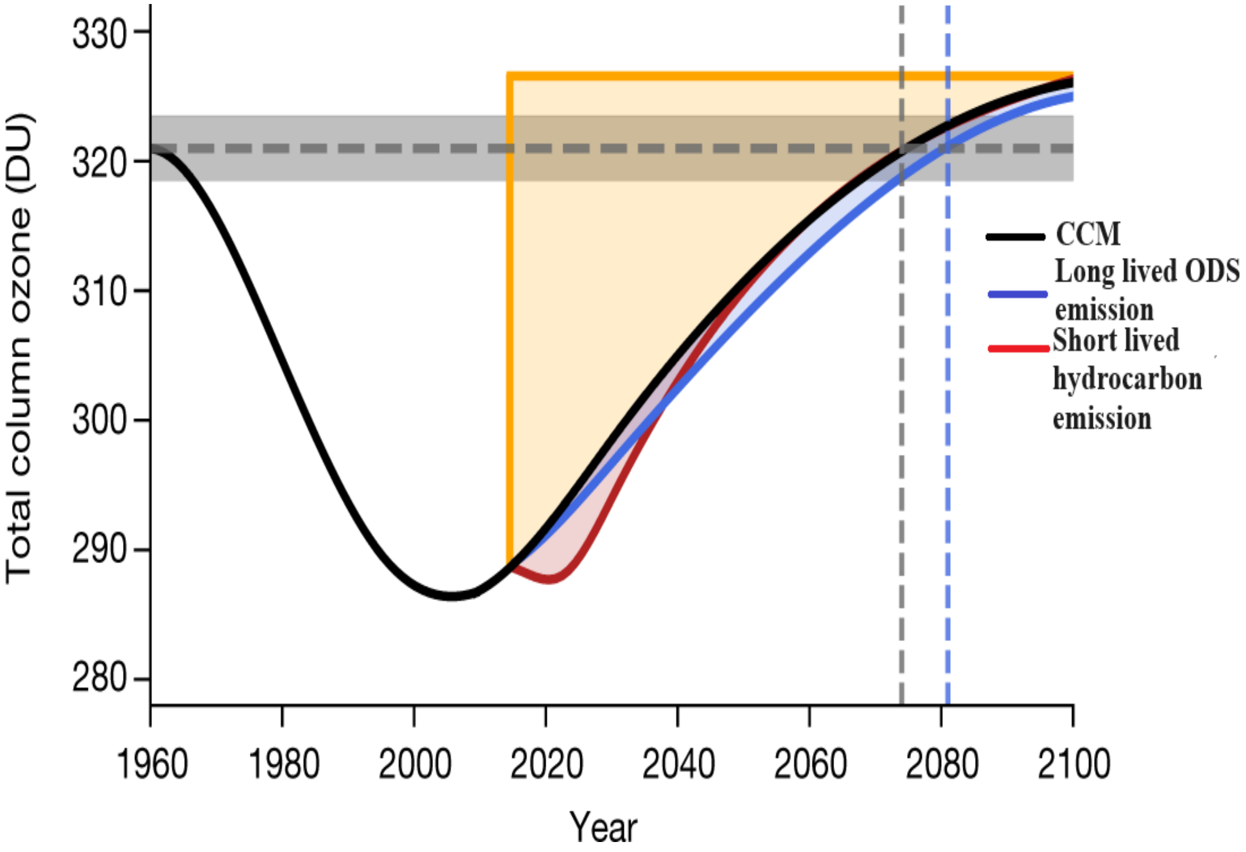

Figure 1.7: Projection of the global mean columnar ozone amounts (DU) from 1960 to 2100 (Reproduced from Pyle et al., 2022)

1.5.2. Sudden stratospheric warming

Next, another important phenomenon in the context of middle atmosphere is the sudden stratospheric warming (SSW) defined as the sudden amplification of the stratospheric temperature by several tens of Kelvin within a span of few days. This was first observed by Richard Scherhag in the year 1952. SSW occurs when there is large increase of the extratropical planetary waves that results in the disruption of the stratospheric polar vortex. In 1971, Matsuno suggested that owing to tropospheric forcing, there is an excitation of the free wave mode of Rossby waves that may result in SSWs. The warming effect is observed within 10–50 km above the surface of the earth and is classified into major and minor warming based on the changes in wind direction within the polar vortex.

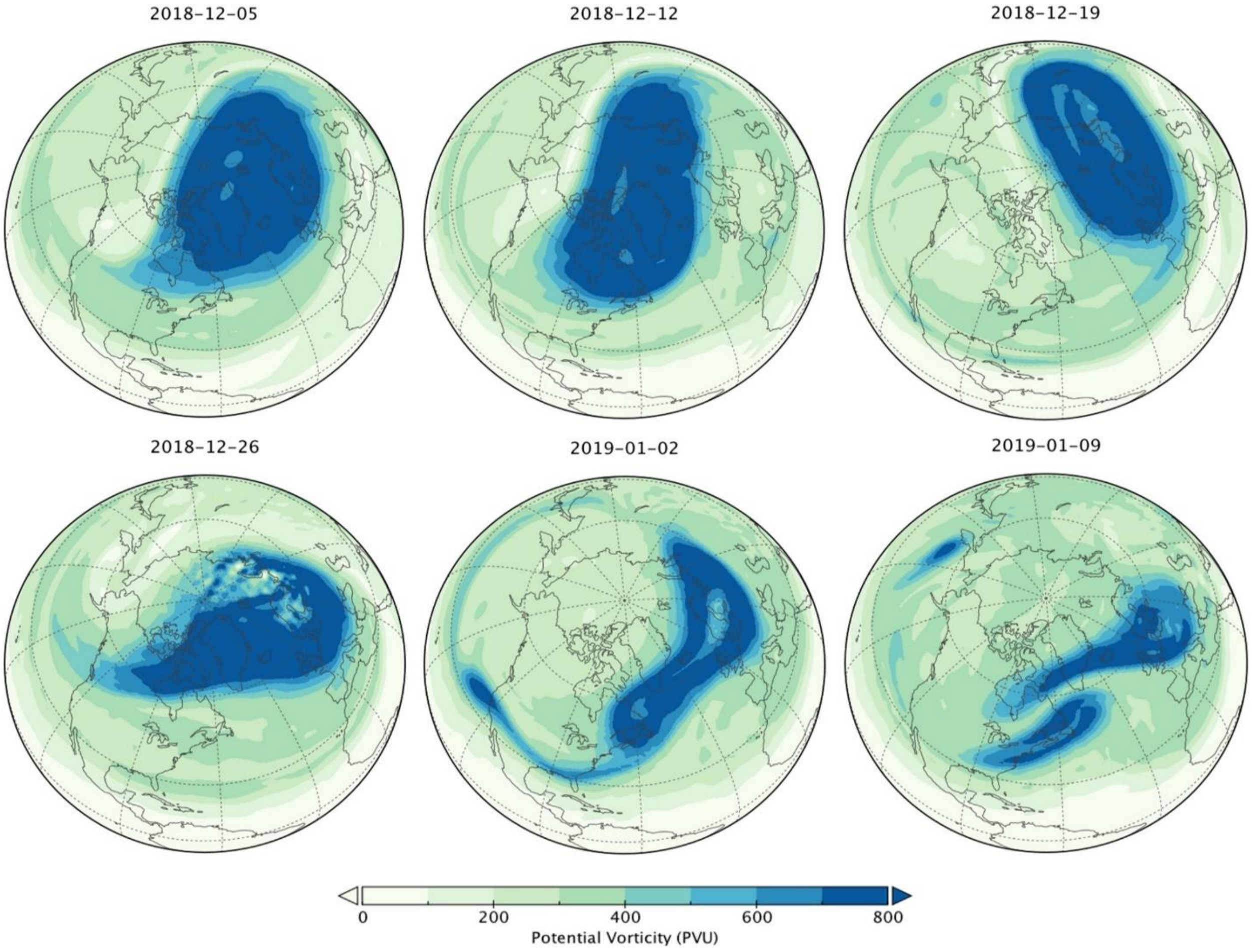

Figure 1.8: Illustration of the Potential Vorticity on the 850-K isentropic surface representing the displacement followed by splitting of polar vortex during an 2018-2019 boreal SSW (Reproduced from Baldwin et al., 2021)

The minor warming does involve the rise in stratospheric temperature within the polar vortex, but there is no wind direction reversal (westerly to easterly) associated with it. However, the strength of the westerlies are observed to diminish within the vortex. The major warming events are identified as when there is an increase in latitudinal mean temperature and a reversal of westerly winds to easterly at 60 degrees latitude and 10 hPa. There is another mode of classification of the SSW events. One only involves equatorward displacement of the vortex, called as displacement event. The other involves the splitting of the vortex into some daughter vortices, which is known as splitting event. The horizontal maps of potential vorticity (PV) can portray the displacement or the split events as shown in Figure. 1.8. After the total displacement of the vortex (botton middle), splitting is observed (bottom right).

Zonal wavenumber (mostly wave 1 and 2) classification of the tropospheric precursor patterns can also determine the type of SSW (Cohen and Jones, (2011), Garfinkel et al. (2010), Tung and Lindzen, (1979a), Woollings et al. (2010)). Wave number 1 precedes displacement event, while both wave number 1 (initially) and 2 (finally) can drive the split events (Martius et al. (2009), Castanheira and Barriopedro, (2010)).

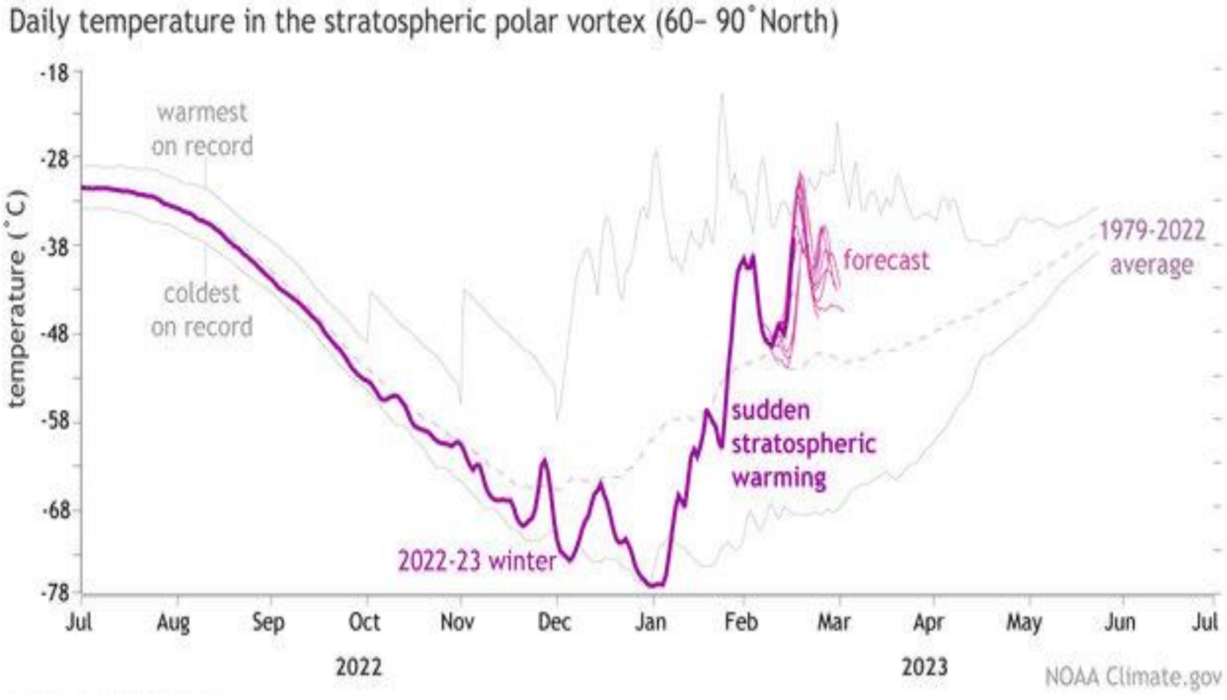

Figure 1.9: Average daily temperatures at 10 hPa pressure level in the Northern Hemisphere (Credit: NOAA Climate Prediction Center)

SSW events can impact on tropospheric weather. The downward transmission of easterly winds generated due to SSW affects the jet stream. This leads to the reduction of the strength of the tropospheric vortex and cold outbreaks in Northern Europe. In the upper atmosphere, the SSW events can lead to more high latitude adiabatic cooling (Limpasuvan et al. (2016)), zonal mean zonal winds changes from easterly to westerly in the UMLT and decrease in the PMC occurrence (Karlsson et al. (2007)). It also inhibits the heterogeneous ozone depletion processes (Lim et al. (2019), Thompson et al. (2005)) occurring in Southern Hemisphere.

Almost all the Arctic winters have at least one SSW event, although the frequency differs based on the criteria considered to classify the type of warming (Kuttippurath and Nikulin, (2012), Roy and Kuttippurath, (2022)). Even multiple SSWs are observed in the Arctic during 1998/99, 2001/02, 2007/08 and 2009/10 (Labitzke and Kunze, (2009)) . However, only two (2002 and 2019) are observed in southern hemisphere until this date. This is because of the orography and the more land sea thermal contrast in the northern hemisphere that causes stronger planetary waves over there, compared to the southern hemisphere.

One example of the temperature changes associated with the recent boreal SSW of 2023 is shown in Figure 1.9. The gray lines indicate the warmest and coldest temperatures recorded between 1979 and 2022 respectively. The dashed purple line represents the average temperature. Model forecast (pink lines) shows that the warming will exhibit a new peak in coming days.

1.6. A spectrum of waves

Atmospheric wave is a disturbance that propagates (or stands still) in the atmosphere as a function of space and time and therefore it is manifested in the spatio-temporal changes of concentration, temperature, pressure and wind flow in the atmosphere. They originate when an air parcel is displaced from its equilibrium. Due to the decrease of atmospheric density with height, atmospheric waves grow in amplitude as they travel upwards. After attaining the maximum amplitude in the UMLT region, the large-scale waves dissipates over there. Based on the horizontal scale of motion, wave scan be classified as sound waves, mesoscale waves and planetary waves as shown in Figure 1.10.

However, in the context of the middle and upper atmospheric study, the thesis will focus on the generation, propagation and dissipation of the three types of waves, namely, GW, atmospheric tide and PW, as they largely dominate the UMLT dynamics.

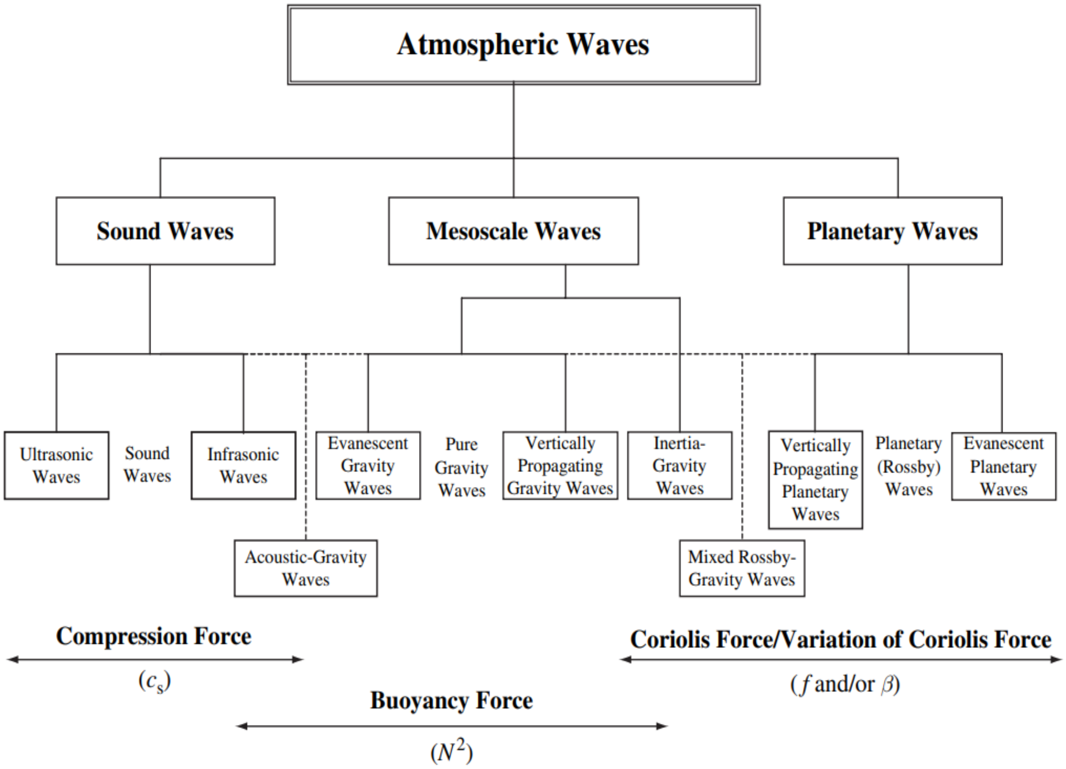

Figure 1.10: Classification of atmospheric waves (Reproduced from Lin., 2007)

1.6.1. Gravity waves

Gravity waves are meso-scale waves occurring in a stably stratified fluid and having periods ranging between ~5 minutes to several hours (from Brunt-Väisälä frequency to inertial period). They transfer momentum from lower to upper atmosphere and the restoring force acting for it is the buoyancy. It is formed when the Earth's gravity and the atmospheric density gradients (restoring force) become comparable with compressibility forces. From various sources like topography, wind shear, convective systems, frontal systems, tidal waves, earthquakes, volcanic eruptions, Kelvin-Helmholtz instability around the jet stream GW can generate (Fritts and Alexander, (2003)). While propagating (horizontally and vertically), their spectrum encounter a number of factors, like background wind, temperature, etc. The atmospheric constituents and middle atmospheric circulation are also affected by the GW on a global basis.

In the context of linear wave theory, let us consider a monochromatic GW in an adiabatic, frictionless, stably stratified atmosphere. Using the basic equations of atmospheric motions, the variation of small perturbations are expressed by a harmonic function as

$$m^2 = k^2 (N^2-\omega^2) / (\omega^2-f^2) \tag{1.12}$$

$$\omega = k (c-\bar{u}) \tag{1.13}$$

where, ω is the frequency, k is the horizontal wavenumber in the vertical propagation direction, m is the vertical wavenumber, N is the Brunt–Väisälä frequency, f is inertial frequency due to Coriolis force and $\bar{u}$ is the background horizontal wind velocity. For vertical propagation of the waves, $m^2 > 0$, so that the frequency lies in the range $N > \omega > f$.

GW becomes unstable when their amplitude (in the direction of their horizontal wave propagation) becomes greater than their intrinsic phase speed. In case of high frequency GWs, the dominant instability is the convective instability and for low frequency GW, it is the dynamical instability (Fritts and Rastogi, (1985)). The convective instability develops as the temperature perturbations induced by the waves forms localized unstable regions in the atmosphere. However, the dynamical instability is formed when the wave induced vertical shear in the horizontal winds exceeds a certain value. The GW dissipation can cause energy dissipation, turbulence and also small scale mixing in the atmosphere.

1.6.2. Atmospheric tides

Atmospheric solar tides or thermal tides are global scale oscillations having periods, which are sub-harmonics of a solar day, that is, 24, 12, 8, 6 hr and so on. The periodic solar heating of the atmosphere results in its generation. It’s lunar diurnal and semi-diurnal periods are about 24.8 h and 12.4 h respectively. This is in contrast to gravitational tides or oceanic tides, which are generated due to gravitational forcing of the moon on the earth and its centrifugal acceleration. The oceanic tides have comparatively smaller amplitude (~5–20% of solar tides).

Bartels (1926) first observed semi-diurnal variation in barometric surface pressure measurement with a periodicity, which is harmonic of a solar day. Almost 16% of the solar radiation, which is absorbed by atmospheric ozone, water vapor and molecular oxygen, can lead to the generation of this kind of surface air tide. Gradually, with the decrease of the atmospheric density with height, these tides propagate upward (indicated by downward phase progression) and exhibits large amplitudes (several tens of m/s) in the UMLT region.

The vertical, latitudinal and diurnal heating profile is shown in Figure 1.11 which illustrates a ‘square wave’ heating profile in local time is generated as the solar heating takes place only during the day and the heating is also more over the equator. The Fourier analysis of this heating curve provides a mean component, a diurnal (24h) component, a smaller semi-diurnal (12h) component and successively smaller significant 8h and 6h components. Additionally, the maximum heating at the equator suggests the presence of larger tidal amplitudes at the equator. Although it is true for only the diurnal tide because of its short vertical wavelength (resulting in destructive interference) compared to the depth of the atmosphere where it is forced. The semi-diurnal tide maximizes at mid-latitudes.

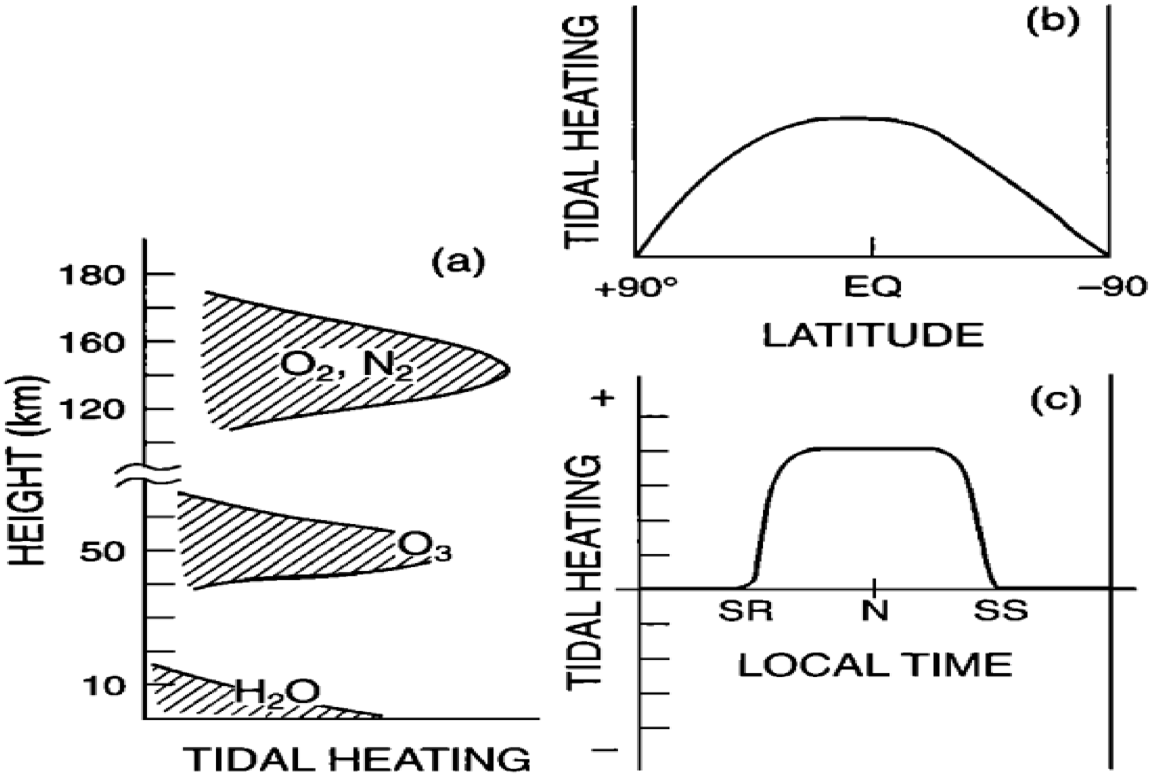

Figure 1.11: Schematic of tidal heating with (a) height, (b) latitude and (c) local time (Reproduced from Forbes, 1995)

Tidal field equations

Classical Tidal Theory describes the basic characteristics of atmospheric tides. The primitive equations (conservation of momentum, continuity equation, hydrostatic approximation, ideal gas law, first law of thermodynamics) are linearized for an isothermal atmosphere to get the Laplace's tidal equations in spherical polar coordinates, as follows

$$\mathrm{H}\frac{\partial^2 \mathrm{G}^{\sigma,S}}{\partial z^2}+\left(\frac{\mathrm{d}H}{\mathrm{d}z}-1\right)\frac{\partial \mathrm{G}^{\sigma,S}}{\partial z}=\frac{g}{4\,a^2\omega^2}F\left[\left(\frac{\mathrm{d}H}{\mathrm{d}z}+k\right)\mathrm{G}^{\sigma,S}-\left(\frac{k.\mathrm{J}^{\sigma,S}}{\gamma g H}\right)\right] \qquad (1.14)$$

where, $G=-\left(\frac{1}{\gamma\,p_0}\right)\frac{\mathrm{D}p}{\mathrm{D}t}$,

$\left(\frac{\mathrm{D}p}{\mathrm{D}t}\right)=\frac{\partial\,\delta p}{\partial t}+\mathrm{w}\,\frac{\mathrm{d}\,p_0}{\mathrm{d}\,z}=\gamma g H\frac{\mathrm{D}\rho}{\mathrm{D}t}+(\gamma-1)\,\rho_0 .\,\mathrm{J}$,

ρ_0, p_0 = initial density and pressure, $\delta\rho, \delta p$ = tidal perturbation in density and pressure, t = time, γ = ratio of specific heats of air of constant pressure to constant volume, k = R / specific heats of air of constant pressure, z = vertical coordinate, H = scale height, g = acceleration due to gravity, a = earth's radius, ω = angular frequency of earth's rotation, s = zonal wavenumber. It is assumed that the tidal fields are linear and varying harmonically in longitude and time. The above equation can be solved using separation of variables and the solution is as follows

$$\mathrm{G}^{\sigma,S}=\sum_{n=1}^{\infty}\mathrm{L}^{\sigma,S}(z)\,\Theta^{\sigma,S}(\theta) \quad \text{and} \quad \mathrm{J}^{\sigma,S}=\sum_{n=1}^{\infty}\mathrm{J}^{\sigma,S}(z)\,\Theta^{\sigma,S}(\theta) \qquad (1.15)$$

where G is the response of the forcing J. $\mathrm{L}^{\sigma,S}$ is vertically dependent and $\Theta^{\sigma,S}$ is latitudinally dependent. Using the above two solutions, equation (1.14) is divided into two parts as follows

$$\mathrm{F}\,(\,\Theta^{\sigma,S})=-\frac{4\,a^2\omega^2}{g\,\mathrm{h}^{\sigma,S}}\,\Theta^{\sigma,S} \qquad (1.16)$$

$$\mathrm{H}\frac{\mathrm{d}^2\mathrm{L}^{\sigma,S}}{\mathrm{d}z^2}+\left(\frac{\mathrm{d}H}{\mathrm{d}z}-1\right)\frac{\mathrm{dL}^{\sigma,S}}{\mathrm{d}z}+\frac{1}{\mathrm{h}^{\sigma,S}}\left(\frac{\mathrm{d}H}{\mathrm{d}z}+k\right)\mathrm{L}^{\sigma,S}=\frac{k}{\gamma g H\,\mathrm{h}^{\sigma,S}}\mathrm{J}^{\sigma,S} \qquad (1.17)$$

where $\mathrm{h}^{\sigma,S}$ are the Eigen values and $\Theta^{\sigma,S}$ are the Eigen functions or Hough functions.

Classification of tides

Tides can be classified as migrating and non-migrating components. Tides that propagate longitudinally westward with the apparent motion of the sun, are known as migrating tides.

Therefore, they vary only with local time. They are generated due to the absorption of solar radiation by water vapour in the troposphere, ozone in the stratosphere, and nitrogen and oxygen in the thermosphere. Migrating tides are expressed as Hough modes in the form (s,n). The latitudinal structure of the tides is defined by the Hough functions. Here, s denotes the oscillation frequency or zonal wavenumber and n is the latitudinal index. For diurnal tide, s=1 and for semi-diurnal tide, s=2. Positive values of n indicates vertically propagating tidal modes and its negative values refers to the trapped or evanescent modes.

Sl No.	Hough mode	Vertical wavelength (km)
1	(1,1)	28.19
2	(1,2)	16.14
3	(1,3)	11.36
4	(1,5)	7.18
5	(2,2)	292.30
6	(2,3)	81.24
7	(2.4)	54.43
8	(2.5)	41.32
9	(2.6)	33.75

Table 1.3: Vertical wavelengths of different Hough modes

Examples of propagating symmetric diurnal tidal modes are (1,1), (1,3),…. and anti-symmetric are (1,2), (1,4),… The trapped symmetric and anti-symmetric modes are denoted as (1,-2), (1,-4),… and (1,-1), (1,-3),…respectively. The vertical wavelengths of different Hough modes in an isothermal atmosphere is given in table 1.3.

There is another component of tide, which depend on both longitude and local time, known as non-migrating tide. They propagate either eastward or westward or remain stationary (Miyahara and Miyoshi, (1997), Smith, (2012)) owing to the longitudinal asymmetry of its heat sources. Eddy heat transfer in the boundary layer, convective processes, or non-linear interaction between global scale waves can lead to the generation of these non-migrating tidal modes.

Tides acts to couple the lower atmosphere to the ionosphere by transmitting energy from its source origin. They can also modulate the upward propagating GW and can themselves be modified due to PW activity (Pedatella et al. (2012)). Mostly after reaching their maximum amplitude in the UMLT region, they undergo dissipation owing to turbulence that are generated by GW and DT. The dissipation can either be thermal dissipation, like thermal conduction and infrared cooling or mechanical dissipation, like viscosity and turbulence (Teitelbaum and Vial. (1981)). The damping of these tides results in the deposition of the net momentum and energy into the mean wind flow. It then modifies the mean wind and temperature of the UMLT region (Forbes et al. (2008)).

The nomenclature of the tides is as follows: the first letter represents the tidal periodicity, D=diurnal, S=semi-diurnal, T=ter-diurnal, and Q=quarter-diurnal with periodicities of 24h, 12h, 8h and 6h respectively; the second letter represents the direction of propagation (W-westward, E-eastward, S-stationary) and the third character represents the zonal wavenumber.

1.6.3. Planetary waves

Another global scale undulation that can cause horizontal (zonal) motion of air parcels is known as planetary wave. These waves are generated due to earth's rotation and restoring force of it is the poleward gradient of planetary vorticity. PWs have an integral number of cycles wrapped around a full longitude circle (2,5,10 and 16) and they not only play a dominant role in the spatial and temporal variability of the stratospheric dynamics, but also make major contributions up to the UMLT region. PWs are responsible for transferring heat between equator and poles. Therefore, it keeps the atmosphere in balance.

The PW generation can be illustrated in the following way. Let us assume if an air parcel is moving eastward in the Northern Hemisphere (shown in Figure 1.12) and has no rotation about the vertical axis, the relative vorticity will be zero. On poleward displacement, the planetary vorticity ($2\Omega \sin \varphi$) of the parcel will increase, resulting in the decrease of the relative vorticity if the absolute vorticity is conserved. Therefore, the parcel will exhibit clockwise rotation about the vertical axis. The combination of the clockwise and eastward movement results in the southward (equatorward) flow of the parcel. Finally, the parcel will reverse back and result in an oscillation along the equilibrium position.

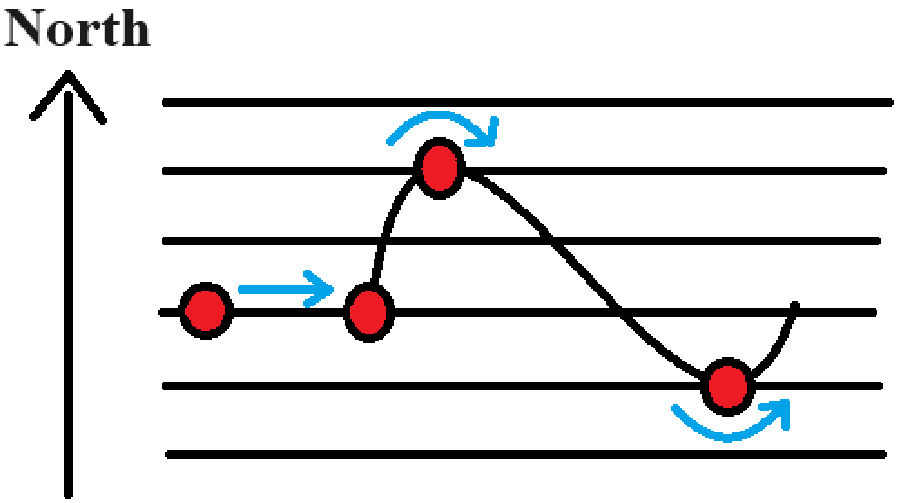

Figure 1.12: A schematic of an air parcel when displaced by PW in the Northern Hemisphere

A range of periods have been identified for PWs, viz., 1.9 to 2.2 days (for 2 days), 4 to 7 days (5 days) and 10 to 20 days (10 and 16 days). The quasi-2 day wave have been studied extensively using meteor radar observations (Muller and Nelson, (1978), Kal'chanko and Bulgakov, (1973)) in the upper mesosphere. They can reach amplitudes over 50 m/s. Tsuda et al. (1988) observed that its amplitude generally decreases between 82 and 104 km. Although the quasi-16 day wave has a smaller westward phase speed and it only propagates upward in winter when there is eastward stratospheric background wind as per the observational and modelling studies (Luo et al. (2002)). However, observations revealed the maximization of this wave is seen during high latitude summer near to the mesopause (Epsy et al. (1997)).

The mathematical representation of PW can be done using the following dispersion relation

$$c = -\frac{\omega}{k} = \bar{u} - \frac{\beta}{k^2+l^2} \tag{1. 18}$$

where c is phase velocity of the wave, ω is frequency, k, l and m are wavenumbers, $\bar{u}$ is the mean flow, β is change of Coriolis force in y-direction. To satisfy the equation 1.18, (c - $\bar{u}$) has to be negative as the Rossby critical velocity ($\frac{\beta}{k^2+l^2}$) is positve. This indicates that Rossby waves propagate westward with respect to the background flow.

For three dimensional dispersion relation, equation 1.18 becomes

$$c = -\frac{\omega}{k} = \bar{u} - \frac{\beta}{k^2 + l^2 + \frac{m^2 f^2}{gN}} \tag{1. 19}$$

For the vertical propagation of a stationary PW, c=0 and m^2 has to be positive. Therefore, a new condition is set as

$$0 < \bar{u} < \frac{\beta}{k^2 + l^2} \tag{1. 20}$$

This indicates that stationary waves propagate vertically only if the background flow is moderately eastward. This is known as Charney-Drazin criterion (Charney and Drazin, (1961)).

1.7. The polar atmosphere

Most of the portion of the thesis discusses how the polar atmospheric events affects the global middle and upper atmosphere. The polar region is a least explored area in comparison to the low and mid latitudes because of its limited satellite coverage and also because of its hostile environment that results in the lack of in-situ measurements. There are several commonalities and interhemispheric differences in the dynamics of the Arctic and the Antarctic. The wave activity in the Northern hemisphere is larger in comparison to the Sothern hemisphere owing to large land sea contrast over the Northern hemisphere. This leads to more SSW events in the Arctic (only two SSWs are recorded till date in the Antarctic) due to its weaker vortex strength. On the other hand, ozone hole is seen only in the Antarctic owing to extremely low temperature maintained by the stratospheric polar vortex during austral springtime. The upshot of these polar atmospheric events, viz., ozone hole and SSW is observed to extend well beyond the polar latitudes and it influences different atmospheric layers on a global scale. Therefore, using ground-based, space-borne, model and reanalysis datasets, atmospheric events in the Arctic and Antarctic, their impacts on the pole, equator and antipodal regions are discussed in connection to the different kinds of waves, which have mostly their source origin in the lower and middle atmosphere.

1.8. Scope of the thesis

The large-scale atmospheric waves and tides act as a coupling agent between different atmospheric layers and it leads to the changes in circulation, thermal structure, chemical composition and plasma irregularities in the middle and upper atmosphere associated with the atmospheric processes originating in the lower and middle atmosphere. In this thesis, we particularly focus on the impact of polar atmospheric events (Antarctic ozone hole and SSW) on the UMLT winds, wave and tidal propagation, non-linear interaction between waves and tides and generation of ionospheric plasma irregularities associated with solar thermal tides. The changes are observed from the lower to the upper atmosphere and from one hemisphere to the other, indicating both the vertical and horizontal coupling.

The objectives of the thesis are as follows:

1. To study the impact of stratospheric wave activity in controlling the springtime polar UMLT winds and tides associated with Antarctic ozone depletion.
2. To investigate the role of waves and tides in driving the summertime polar westward UMLT winds.
3. To unravel the relationship between SSW events and equatorial valley region irregularities, owing to the changes in the low latitude tidal amplitudes.
4. To extend the investigation of the impact of the SSW events and their corresponding changes in tidal amplitudes of the antipodal UMLT region.

Chapter 2: Data and Methodology

Introduction

The thesis describes different ground based instruments, satellite datasets and reanalysis products used for probing the middle and upper atmosphere. The ground-based instruments include meteor radars, very high frequency radars, ionosonde; space-borne instruments include Microwave Limb Sounder (MLS), Sounding of the Atmosphere using Broadband Emission Radiometry (SABER), whereas National Centers of for Environmental Prediction/ National Center for Atmospheric Research (NCEP/NCAR) and ERA-5 provides the reanalysis products. Also, the Specified Dynamics-Whole Atmosphere Community Climate Model (SD-WACCM) model outputs are used in this thesis and compared with the reanalysis products and satellite data measurements. In this chapter, the instruments, datasets and the methodology are described concisely.

2.1. Equatorial Atmosphere Radar

The Very High Frequency Equatorial Atmosphere Radar (EAR) in Kototabang, Indonesia (0.20° S, 100.32° E, 10.36° S dip latitude) is routinely operated at 47-MHz with peak and average powers of 100 kW and 5 kW respectively, to study the Valley region FAIs at ~3 m scale size during day times (0600–1800 LST).

Figure 2.1: Equatorial Atmosphere Radar (EAR), Kototabang (Reproduced from Fukao et al., 2003)

The EAR has a quasi-circular active phased array consisting of 560 three-element Yagi antennas, each containing a transmitter-receiver module as shown in Figure 2.1. It is a collaborative project between Research Institute for Sustainable Humanosphere (RISH) under Kyoto University and Lembaga Penerbangan dan Antariksa Nasional (LAPAN) under Indonesia. It covers the height region of 90–200 km with a height resolution of 1.2 km (Fukao et al. (2003)). It is designed in such a way that it can steer the antenna beam 360º on a pulse-to-pulse basis within 30° from zenith in order to observe the detailed 3D structured small-scale processes of the equatorial atmosphere. It can also provide wind information from 1.5 to 20 km, temperature altitude profile using radio acoustic sounding system, etc. The system specifications are given in table 2.1.

Item	**Specification**
Operating frequency	47 MHz
Antenna	Quasi-circular array of 560 three-element Yagi
Aperture	110 m in diameter
Beam Width	3.4º
Gain	33 dBi
Number of TR modules	560 units
Single TR module's power	180 W/unit
Pulse width	0.5-256 µs
IPP	200 µs-10 ms
Receiver type	Single super heterodyne
Noise Figure	5 dB (TR modules)
Pulse compression	Barker, complementary and Spano codes (1-16 bits)
Subpulse width	0.5, 1.0, 2.0, 4.0, 8.0, 16.0 µs
Dynamic range	70 dB
A/D converter	14 bits
Number of range gates	256

Table 2.1: Specifications of EAR, Kototabang

Using the EAR data, the 150-km radar echoes are detected visually from the range-time intensity (RTI) plots having SNR > -8 dB in the height region 130-180 km during geomagnetic quiet days (Ap index value less than or equal to 12).

2.2. SKYiMET VHF Meteor Radar over Esrange and Rothera

The wind data of the polar UMLT region (80–100 km) are acquired from two opposite polar latitude meteor radars installed at Esrange (67.90° N, 21.10° E) and Rothera (67.5° S, 68.1° W).

The SKYiMET meteor radar located at Esrange (Figure 2.2) in northern Sweden, about 30 km east of Kiruna, operates at a central frequency of 32.5 MHz ($\lambda = 9.23$ m), peak power of 6 kW, with a pulse repetition frequency (PRF) of 2143 Hz and a pulse length of 13.3 µs. The radar consists of one transmitter and five receiver (Rx1–Rx5) antennas over an area of 2000 m^2. The radar has been operated continuously since October 1999, except during the winter of 2009/2010, when the radar was non-operational due to some noticeable hardware problems.

Figure 2.2: Meteor radar over Esrange (https://people.bath.ac.uk/eesnjm/old_pages)

Similarly, the SKYiMET meteor radar at Rothera (Figure 2.3), located in the Adelaide Island off the Antarctic Peninsula, uses a solid-state transmitter and operates at a radio frequency of 32.5 MHz, with a peak power of 6 kW, PRF of 2,144 Hz and with a duty cycle of 15%. The radar has been operational since February 2005. It works in All-sky configuration, transmits signal through one 3-element Yagi transmitter and receives through five 2-element separate receivers (Hocking et al. (2001)), to provide horizontal wind data in the 80–100 km height region. However, in 2019, with the replacement of old antennas, that degraded due to weather conditions, the reduction in the ambiguous meteor detection was observed (Dempsey et al., 2022). In addition, the wind data for the periods January 2005, December 2009–January 2010, December 2010 are not considered, as there was an increased spread of meteor height distribution observed at those periods due to radio interference.

Figure 2.3: Meteor radar over Rothera (https://people.bath.ac.uk/eesnjm/old_pages)

The meteors ablates after entering the atmosphere. The meteor radar detects the coherent backscatter from each individual electron on the meteor trail drifting with the wind, orthogonal to its direction of propagation. With an assumption that wind drifts the meteor trails, the least square method is used to fit the azimuth and horizontal component of drift velocity to obtain the horizontal wind velocities from both radars (Sandford et al. (2010)).

In the thesis, two different windows are selected in this study for calculating the tidal amplitudes. At first, the 5-day composite mean wind measurement is used in order to remove the small scale fluctuations generated due to gravity waves. The composite mean is shifted by one day for obtaining the daily tidal amplitudes. No further data smoothing is performed. It is then fitted to the equation 2.1 and the amplitudes are estimated using the least square method.

$$u(t), v(t) = a_0 + \sum_{i=1}^{i=3} \left(a_i \, sin(\frac{2\pi}{T_i} t + \phi_i) \right) \tag{2.1}$$

where, a_0 denotes the prevailing mean wind, a_i, and ϕ_i are the amplitude and phase of the tidal components with i=1,2,3 corresponding to 24-hr,12-hr,8-hr tides. The technique is described in Thayaparan et al. (1995) and Hocking and Thayaparan, (1997).

However, for distinguishing the closely spaced solar (12-hr) and lunar (12.42 hr) SDT amplitudes, the fitting window length (N) must 1/N*24 < 1/12-1/12.42, which is N>14.78. Therefore, the lunar SDT amplitude is calculated using least square method by considering a 30-day bins in wind measurement (shifted by one day) and is fitted to equation 2.2

$$u(t), v(t) = a_0 + \sum_{i=1}^{i=3} \left(a_i \, cos(\frac{2\pi}{T_i} t - \phi_i) \right) \tag{2.2}$$

where i=1,2,3 corresponding to 24-hr,12-hr,12.42-hr tides. The technique is employed by Stenning et al. (1997) and Sandford et al. (2006).

Using the horizontal wind data, the variances for GW is measured by taking summation of the square of the amplitudes extracted from the spectral analysis of winds (within the inertial period) after removing the major tidal components (Beldon & Mitchell, (2009); Mitchell & Beldon, (2009)). Similar to the GW variance, the PW variance is calculated here by considering the PW having period greater than 2 days and less than 20 days. Alternatively, planetary wave is calculated by summing the power corresponding to the periods 2-31 days from the wavelet spectra (using Morlet as the mother wavelet) of the winds. The interannual variability of the winds and tides used in the thesis is calculated from the standard deviation of the wind and the tidal amplitudes. The wind data over Esrange and Rothera are available from August 2002 to November 2019 and from February 2005 to September 2024, respectively.

2.3. Kototabang ionosonde

The ionosonde present at Kototabang, Indonesia broadcasts a sweep of frequencies in the range 2-20 MHz, with a peak power of 20W. Here, the data is received every 5 minutes and is an ionosonde of frequency modulated-continuous wave (FM-CW) type. The ionosonde is a part of Southeast Asia low-latitude ionospheric network (SEALION) and is operated by National Institute of Information and Communications Technology (NICT) (Maruyama et al. (2007)), September 2004 onwards. From the reflected signal, the electron density profile in ionosphere is obtained. The virtual height is calculated by measuring the time taken by the signal to reflect back to the receiver and the frequency at which it is reflected is called the critical frequency (f_0) of the year. It is expressed mathematically as

$$f_0 = 8.98 \sqrt{N_e} \tag{2.3}$$

The virtual height is higher than the real height. True height analysis can be done to obtain the real height from the virtual height information. The observation parameters obtained from this ionosonde are listed in the following table

System	**FM-CW with pseudo-random Tx/Rx switching**
Average Tx power	10 W
Peak Tx power	20 W
Sweep rate	100 $kHzs^{-1}$
Sweep repetition period	5 min

Table 2.2: Specifications of Kototabang ionosonde

In this thesis, we have used virtual height of the bottomside F layer (hpF or h'F) data and some sample ionogram observations for observing the presence of the intermediate layers at the equatorial valley region.

2.4. TIMED-SABER

For studying the variation of ozone and temperature in the middle atmosphere, data is obtained from the Sounding of the Atmosphere using Broadband Emission Radiometry (SABER) instrument onboard the polar orbiting Thermosphere Ionosphere Mesosphere Energetics Dynamics (TIMED) satellite (Russell et al. (1999)). The SABER instrument is a space-borne limb scanning broadband radiometer that makes measurement from ~628 km height, at 74.1° inclination in 97 min orbital period. The latitudinal coverage of the instrument is from 83° N to 52° S or 83° S to 52° N (not covering full day at poles) with a duty cycle of 100%. The viewing angle reverses once every 60 days performing 180° yaw maneuvers, needed for the satellite to evade facing the Sun directly. Hence, the 24-hour measurement is obtained by combining the data from the ascending data taken during the yaw cycle (60 days).

The SABER also provides ozone measurements in the spectral range of 1010 to 1150 cm^{-1} (9.9–8.7 μm) and it is retrieved autonomously from two channels: 9.6 μm and 1.27 μm. In the height region 10-65 km, ozone measurement has a precision of ~2% and in the mesosphere, it is about ~5%. The limb radiances of 15 μm and 4.3 μm channels of CO_2 are used to retrieve kinetic temperature in the stratosphere, mesosphere and lower thermospheric region, with an error of 3.3–5.4 K (Garcia-Comas et al. (2008)). From the temperature data, the amplitude and phases of migrating and non-migrating solar tidal modes are calculated in the following way. First, the SABER temperature data are binned for 65° N – 55° N and 65°S – 55°S in order to extract temperature values for the latitudes 60° N and 60° S between 20 and 120 km. Then, for the yaw, the temperature data for 60 days are arranged according to local time for the longitudes 0^o–30^o E, 30^o E–60^o E, 330^o E–360^o E. The temperature values centering on 12 longitudes (15^oE, 30^oE,.....345^oE) are thus obtained. These two dimensional temperature data are subjected to space-time spectral analysis by applying the following equation

$$T = A_{n,s}\, cos(n\Omega t + (s-n)\,\lambda - \ \phi_{n,s}) \tag{2.1}$$

where T is temperature which is a function of longitude (λ) and local time (t), t(LT)=t(UT)+λ/Ω, UT is universal time, n=1,2,3 corresponds to sub-harmonics of tides with periods 24 h, 12h, and 8h, s < 0 (s > 0) corresponds to eastward (westward) propagating tides, ϕ is phase, and Ω is angular frequency of Earth's rotation (Forbes et al. (2008), Jones et al. (2013)). The tides are referred to as 'migrating', if s = n, when there is no longitude variability at a fixed local time around a constant latitude circle and the tide propagates westward with the apparent motion of the Sun. When $s \neq n$ they are referred to as 'non-migrating' and these non-migrating tides can be either stationary or propagating eastward or westward. The phase is the time of maximum at zero longitude (the local time at Greenwich). The term (s–n) instead of s appears due to the space-based perspective, which is quasi-sun-synchronous, where the t (local time) is constant. In this perspective, a tide having frequency nΩ will have (s–n) maxima and minima around the globe. The 60-day window is moved further by successive days and the procedure is repeated to get the variations of amplitudes of the migrating and non-migrating tidal components. The diurnal tides are referred to by the notation

DWk, DEk and DSk to denote a westward propagating or eastward propagating or stationary tide, respectively, with zonal wave number k. For the semidiurnal tide, D is replaced by S.

2.5. MLS-AURA

To study the ozone and temperature variations at certain pressure levels, the data from Earth Observing System (EOS) Microwave Limb Sounder (MLS) instrument on board the NASA's Aura spacecraft is used. It was launched on 15th July 2004. The spacecraft orbits at ~705 km height with an inclination near to polar (98.2^o), probing 15 orbits coverage in a day by staying fixed relative to the sun (sun synchronous). The MLS measures the vertical profile (55 pressure levels) of several chemical constituents. The MLS Level 2 data can be obtained from NASA Goddard Space Flight Center Data and Information Services Center (GSFCDISC,http://disc.gsfc.nasa.gov/). The instrument scans the atmosphere by thermal emission in the millimeter and submillimeter wavelength, even in the presence of aerosols, cirrus or polar stratospheric clouds The useful range for usage of the MLS products used in this thesis are given in the following table

No.	Product	Useful vertical range
1	O_3	100 – 0.001 261 – 121
2	Temperature	83 - 0.00046 261 - 100

Table 2.3: Summary of vertical useful range for each MLS product

The instrument contains several radiometers for measuring five spectral regions and 36 sub-bands viz., 118 GHz, 190 GHz, 240 GHz, 640 GHz and 2.5 THz. Strong lines of ozone are measured by 240 GHz radiances in between the upper troposphere and mesosphere with a data accuracy of 4–9% (Livesey, (2017)). Temperature data is retrieved from the bands present near O_2 at 118 GHz (stratosphere and above) and 239 GHz (troposphere), measured by R1A/B and R3 radiometers. The data accuracy for temperature at 31.6 hPa is found to be -2 to 0 K.

2.6. NCEP/NCAR Reanalysis 1

A comprehensive coarse grid model of the atmosphere is provided by National Centers of for Environmental Prediction (NCEP) of National Oceanic and Atmospheric Administration and National Center for Atmospheric Research (NCAR) from 1948 to the present (Kalnay, (1996)). Using spectral statistical interpolation, the NCEP data and global spectral model are integrated. The system has three major modules, viz., data decoder and quality control pre-processor, data assimilation module and archive module. The data has a horizontal grid size of 2.5°, which is approximately 280 km in North-South direction and 200 km in the West-East direction. Data is provided at 17 pressure levels from 1000 hPa to 10 hPa, with a temporal resolution of 6 hours. Here, horizontal wind and temperature products at polar stratospheric heights are obtained due to the scarcity of ground and space based observations over there. The output from NCEP is variable in nature because of the addition of different datasets from different models. After data assimilation, reanalysis is carried out by blending observations with global circulation models (GCM).

SSW events mentioned in this thesis are identified from the temperature and zonal wind products obtained from this reanalysis. The positive polar zonal mean temperature difference at 10hPa between the latitudes 90º and 60º during the winter month along with the reversal (or deceleration) of eastward zonal mean zonal wind at 10hPa, indicate the onset day of a SSW onset event. Changes in the PW activity associated with the SSW events are also calculated from the spectral analysis of the temperature product obtained from this reanalysis dataset.

2.7. ERA-5

The ERA-5 is the latest fifth-generation reanalysis of the European Centre for Medium-Range Weather Forecasts (ECMWF), which is the world’s preeminent international weather forecasting organization. It includes detailed data from 1950, split into preliminary back extension (1950–1978) and recent datasets (since 1979) and it replaces the previous ERA-Interim reanalysis, providing higher spatial resolution datasets (Hersbach et al. (2020)). Here, data is regridded to 0.25º regular latitude–longitude grid for the reanalysis and has four main subsets: monthly and hourly products of pressure levels (upper air fields) and single levels (atmospheric, oceanic and land surface). The ERA-5 is providing data globally with a vertical coverage of 1000–1 hPa in 37 pressure levels, and this reanalysis product covers more vertical pressure levels compared to that of NCEP/NCAR.

The ozone, horizontal winds and temperature products at stratospheric heights are extracted to calculate a term called ‘meridional heat flux’ ($-\overline{V`T`}$) that acts to serve as a proxy for PW activity in the stratospheric southern polar region. It is calculated from the daily zonal average of the product of meridional wind perturbation (meridional wind at each longitude subtracted from zonally averaged meridional wind) and temperature perturbation. The negative sign arises because the poleward wind is negative (southward) in the southern hemisphere. In order to identify the relative contribution of PW of zonal wavenumbers (k) 1 and 2 in meridional heat flux, the perturbations with k = 1 and k = 2 are extracted from the spectral analysis of the meridional wind and temperature anomaly in the space domain. The meridional heat flux corresponding to the first (second) harmonics represent the contribution of PW of k = 1 (2).

2.8. WACCM

The Whole Atmosphere Community Climate Model (WACCM) results provides comprehensive numerical output of different atmospheric parameters from the earth’s surface to ~500 km (88 pressure levels) with a horizontal resolution of 0.942º (latitude) and 1.25º (longitude) from 0º E to 358.75º E (providing 192 latitude points and 288 longitude points). Details of the latest version of WACCM is described in Marsh et al. (2013). It is a collaboration that includes the modeling of the upper atmospheric High Altitude Observatory (HAO), middle Atmospheric Chemistry Observations & Modeling (ACOM), tropospheric Climate & Global Dynamics (CGD) using the NCAR Community Earth System Model (CESM). Anthropogenic emissions used in this simulation are obtained from latest Community Atmosphere Model (CAM) inventory. 6-hourly WACCM specified dynamics (SD-WACCM) output provides model output at 88 pressure levels globally from 20th August 2019 in netcdf format (https://www.acom.ucar.edu/waccm/download.shtml).

Chapter 3: Influence of wave forcing in driving the austral polar middle atmospheric circulation in spring

3.1. Introduction

One of the classical examples of the detrimental anthropogenic effect on the environment is the global thinning of ozone layer during springtime in the polar stratosphere, widely termed as ‘‘ozone hole”, first detected over Antarctica in the 1980s (Stolarski and Cicerone, (1974), Molina and Rowland, (1974), Farman et al. (1985)). Owing to the strict implementation of the Montreal Protocol (United Nations, 1987), the onset of the ozone recovery was observed from late 1990s, approximately at the rate of 1–1.5% per year (Montzka et al. (1996), Engel et al. (2002), de Laat and Van Wheele, (2011)). Using model simulation, Pyle et al. (2022) predicted that at about mid-2070, the retrieval of the Antarctic hole can be expected.

In addition to chemistry, the ozone variability in the atmosphere is governed by dynamics. Several studies have revealed that severity of ozone hole are anti-correlated with Planetary Wave (PW) activity (Huck et al. (2005), Salby et al. (2012)). If the PW activity is less, the colder temperature in the polar stratosphere leads to the prevalence of lower stratospheric vortex condition until the end of spring, both in the Arctic (Zurek et al. (1996), Coy et al. (1997)) and the Antarctic (Waugh and Randel, (1999)). This results in an increased latitudinal temperature gradient and a prolonged persistence of strong wintertime eastward winds in lower stratosphere because of the thermal wind balance. Therefore, it can be said that the variability in the stratospheric ozone can result in the alteration of the global energy budget, temperature gradient, chemical structure and atmospheric circulation. Modeling studies have shown that the stratospheric winds can influence the mesospheric winds via selectively filtering the upward propagating waves (Smith et al. (2010), McLandress et al. (2010), Lossow et al. (2012), Xu et al. (2011)). However, very few observational studies have explored the relationship of middle atmospheric winds with the ozone hole occurring during the polar springtime. Moreover, the stratospheric ozone variability is known to influence tidal amplitude in the mesosphere (Hoffmann et al. (2007)). The role of atmospheric tides on vertical coupling between troposphere and upper atmosphere has also been studied using various models (Forbes and Wu, (2006), Wang et al. (2016)) and observations (Oberheide et al. (2009), Hausler et al. (2010), Pancheva and Mukhtarov, (2011)). Therefore, in this chapter, we use 19 years (2002–2020) dataset of ozone to identify its role in regulating wind variabilities of the stratosphere and mesosphere via the upward propagation of waves and tides traversing through the middle atmosphere. Earlier, Venkateswara Rao et al. (2015) used medium frequency (MF) radar and MERRA-2 reanalysis products to show the relation between stratospheric and mesospheric zonal wind variations associated with the springtime ozone loss in the austral polar stratosphere for the years 2002–2014. We have extended that study for a larger period of time and investigated how the stratospheric PW activity governs the wind circulation up to UMLT heights during the ozone loss period and its further connection with the tidal variability at the upper mesospheric heights.

3.2. Data used

For measuring the UMLT winds over Antarctic Peninsula, data is obtained from meteor radar over Rothera. ERA-5 reanalysis products provide measurements of stratospheric winds, ozone and temperature. With the meridional wind and temperature data, a term ‘meridional heat flux ($-\overline{V`T`}$) is calculated which serves as a proxy for the stratospheric planetary wave activity. In order to identify the relative contribution of PW of zonal wavenumbers (k) 1 and 2 in meridional heat flux, the perturbations with k = 1 and k = 2 are extracted from the longitudinal variations of meridional wind and temperature and then the southward meridional heat flux is calculated. Stratospheric temperature and ozone values obtained from the reanalysis product are compared with data from MLS-AURA satellite. Temperature from SABER-TIMED satellite is used for the calculation of amplitude of migrating SW2 tide at upper mesospheric heights over 60° S. Details of the instruments are provided in chapter 2. Data for monitoring ozone parameters (Ozone hole area, ozone minimum and ozone mass deficit) are obtained from NASA Ozone Watch. It consists of a collection of data from various satellites viz., NASA Total Ozone Mapping Spectrometer (TOMS), Aura Ozone Monitoring Instrument (OMI), Suomi National Polar-orbiting Partnership (NPP), Ozone Mapping and Profiler Suite (OMPS), NASA Global Modeling and Assimilation (GMA), ESA Global Ozone Monitoring Experiment (GOME), Solar Backscatter Ultraviolet Radiometer (SBUV/2), NASA Jet Propulsion Laboratory (JPL), MLS and NASA South Pole Balloon Sondes.

3.3. Results

3.3.1. Seasonal and interannual variability of UMLT winds

To start with, Figure 3.1 shows height-time cross section of monthly mean zonal and meridional winds and their anomalies as observed by meteor radar over Rothera Station for the years 2005–2020, between 82 and 98 km.

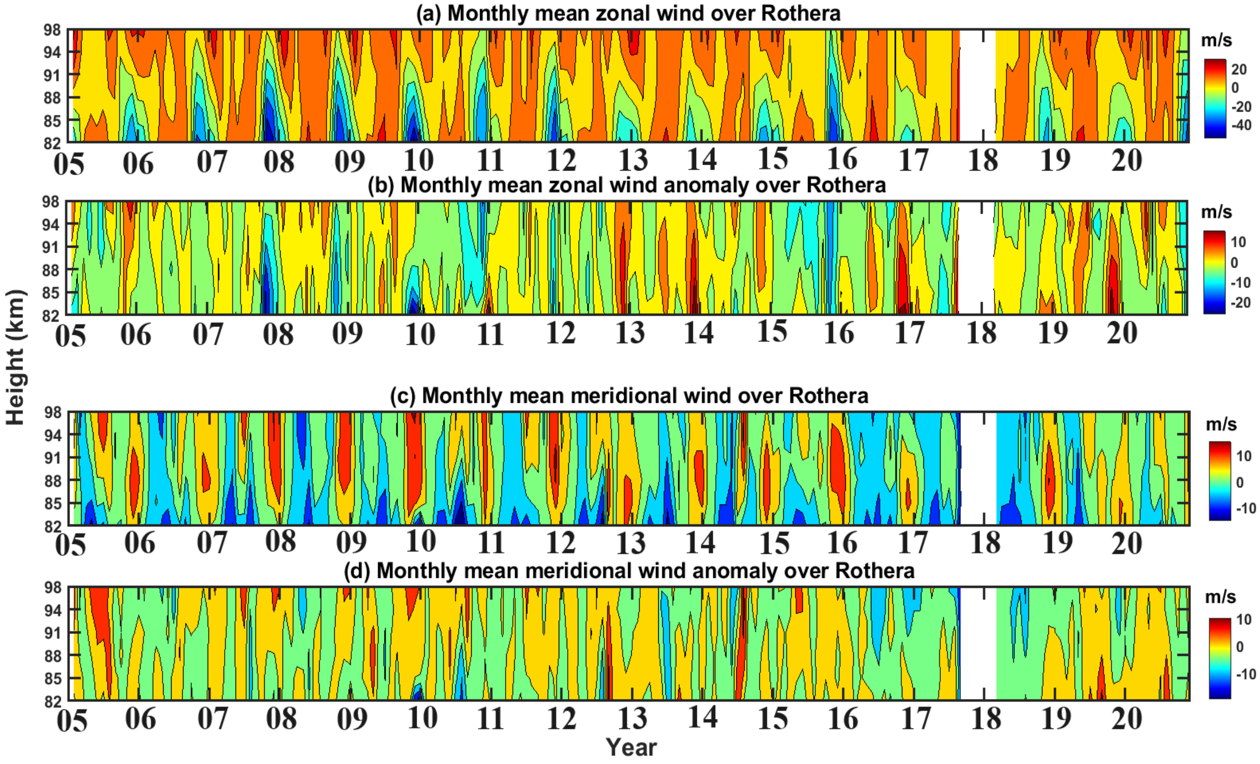

Figure 3.1: Monthly mean (a-b) zonal wind (m/s) and zonal wind anomaly (m/s) and (c-d) meridional wind (m/s) and meridional wind anomaly (m/s) using Rothera VHF meteor radar in the height region 82–98 km for the years 2005–2020

As seen from the Figure 3.1 a, that the zonal wind shows an annual variation with eastward flow during March/April and September/October and westward flow during October/ November - February/March. Westward wind regime (indicated by blue color) is seen to increase with height during 2005–2011. Again, it becomes large during 2015, 2018 and 2020. The monthly wind anomaly (Figure 3.1 b) is calculated by subtracting monthly mean wind (2005–2020) from the monthly wind variation of each year at the respective heights. Negative zonal wind anomaly is observed during 2007 (-20 m/s), 2009 (-26 m/s) and 2015 (-15 m/s). Positive zonal wind anomaly is observed for 2005 (14 m/s at 98 km), 2011 (17 m/s at 82 km), 2012 (13 m/s at 82 km), 2013 (19 m/s at 82 km), 2016 (16 m/s at 82 km) and 2019 (17 m/s at 82 km) during the summer months.

Figure 3.1 c depicts meridional wind, which also shows annual variation, with northward wind prevailing during October/November-February/March (summertime) and the northward wind regime increases with height in the years 2007–2009, 2011 and 2015. Southward flow prevails during March/April–September/October. In some years, strong northward wind regime is observed in the middle of the year, viz., 2005 (14 m/s at 98 km in July), 2012 (12 m/s at 88 km in September) and 2014 (16 m/s at 94 km in August), with an anomaly of 9 m/s, 10 m/s and 11 m/s respectively. Therefore, due to the large year-to-year variation of the horizontal winds, we aim to study the interannual variability of the zonal and meridional winds.

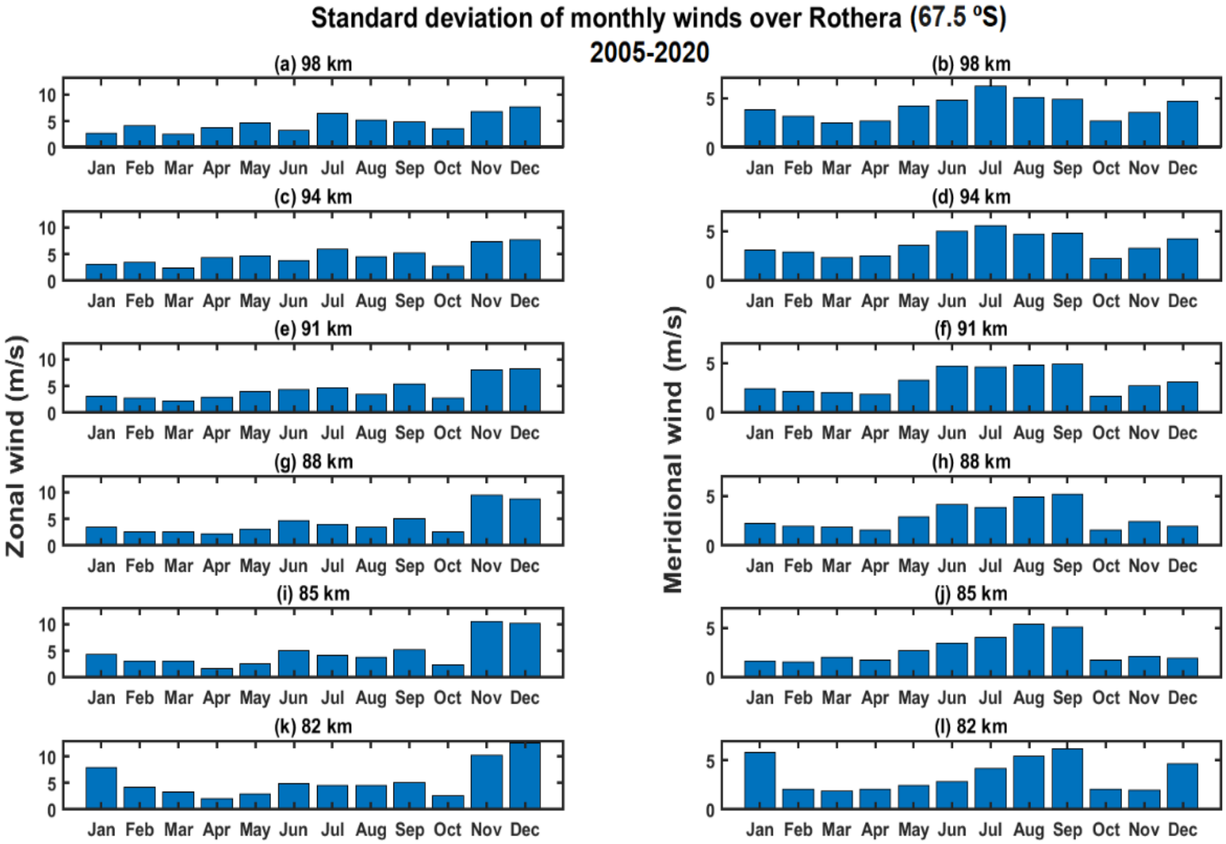

Figure 3.2: Standard deviation of monthly mean (a,c,e,g,i,k) zonal and (b,d,f,h,j,l) meridional winds in the height region 82–98 km using VHF meteor radar over Rothera for the time period 2005–2020

The standard deviation of the horizontal winds at each height, which represents the interannual variability of winds, are presented in Figure 3.2. The zonal winds show large standard deviation in the month of November-December. However, for meridional winds, it is during July to September and also the standard deviation are smaller in magnitude compared to zonal winds. An additional large variability in meridional winds is observed in December–January (except for 82 km).

3.3.2. Seasonal and interannual variability of stratospheric winds

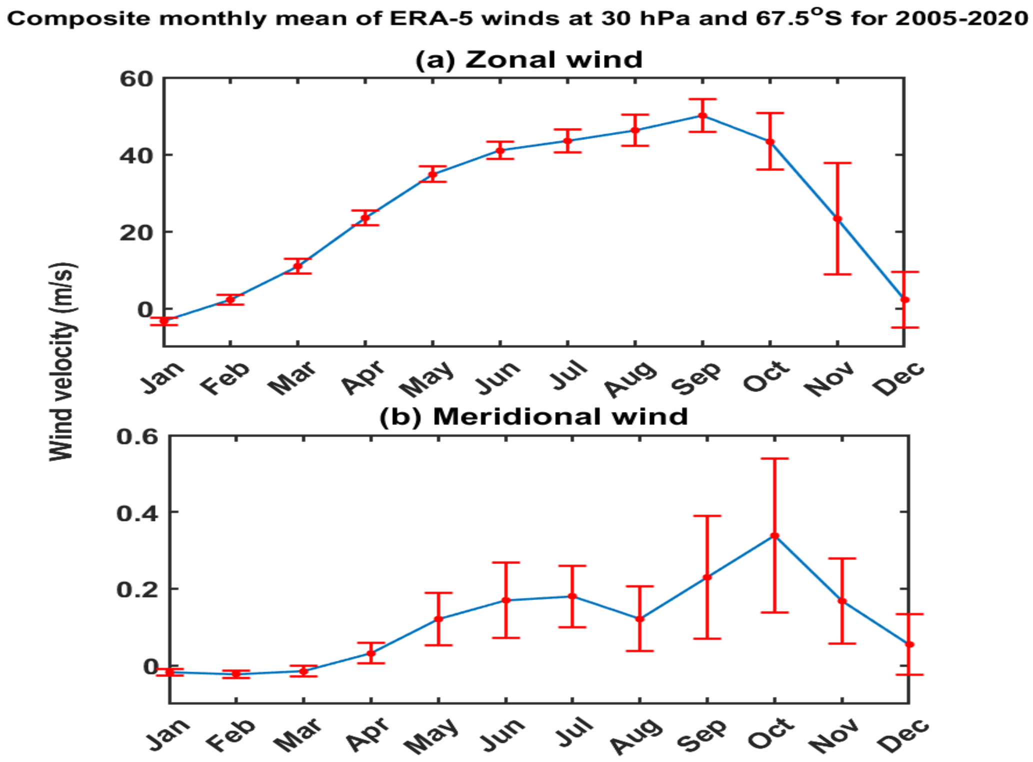

Figure 3.3: Monthly mean and standard deviation of 30 hPa ERA-5 reanalysis (a) zonal wind (m/s) and (b) meridional wind (m/s) at 67.5 S for the time period 2005–2020. The blue line denotes the mean wind velocity and vertical red line denotes the standard deviation of winds for each month

Modeling studies have shown that the winds in the UMLT region are influenced by changes in the underlying stratospheric wind field (Smith et al. (2010), McLandress et al. (2010), Lossow et al. (2012), Xu et al. (2011)). Therefore, in order to find the relation between the two, at first we studied the seasonal and interannual variability of stratospheric winds obtained from ERA-5 reanalysis product, near the region of highest ozone concentration (30 hPa) over Rothera (Figure 3.3).

The composite monthly mean is shown with the blue line and standard deviation is shown with red bars. As seen from the figure, the zonal wind shows eastward maximum in September (50 m/s) and westward maximum in January (-3 m/s). However, the value of the monthly mean meridional wind is close to zero in most of the months. The maximum year-to-year deviation of it is recorded in the month of November (15 m/s) in case of zonal winds and in the month of October (0.2 m/s) in the case of meridional winds. Hence, we have considered the period October-November as the period in which the maximum horizontal stratospheric wind variability is observed. It is well known that this period is popularly known as the ozone loss time in the austral polar stratosphere. Therefore, to investigate further whether ozone loss is driving the winds of this region, the correlation analysis, for measuring the strength of a linear relationship between the winds and ozone during the two months (October–November), is performed.

The scatter plots of some ozone metrics, that is, ozone hole area, ozone minimum, ozone mass deficit and MLS stratospheric ozone volume mixing ratio (vmr) difference (1–68 hPa) between 57.5^{o} S and 77.5^{o} S latitude (centering Rothera station) with stratospheric wind fields are shown in Figure 3.4 for the month of October- November (2005–2020) at 30 hPa. The calculated Pearson's correlation coefficient (R) between stratospheric zonal wind and ozone hole area is 0.95, ozone minimum is -0.95, ozone mass deficit is 0.92 and ozone vmr difference is 0.97. For testing the significance of the correlation analysis, the p value corresponding to a correlation coefficient are calculated. The p-value defines the probability of a null hypothesis to be true. That is, the values greater than 0.05 or the values outside the 95% confidence interval are unlikely to be true. It is observed that for all four correlation coefficients, the p value is close to 0, that is, they are statistically significant. While the R values between stratospheric meridional winds and the ozone loss factors are very less and also are not significant. The highest correlation value of 0.97 between the ozone vmr difference and stratospheric zonal wind suggests that the ozone loss over Rothera station can be best represented with the latitudinal difference of ozone between 57.5^{o} S and 77.5^{o} S, and its larger value causes strong eastward wind flow in the stratosphere. Therefore, ozone vmr difference can be used as the most suitable ozone loss parameter, compared to the other ozone loss metrics.

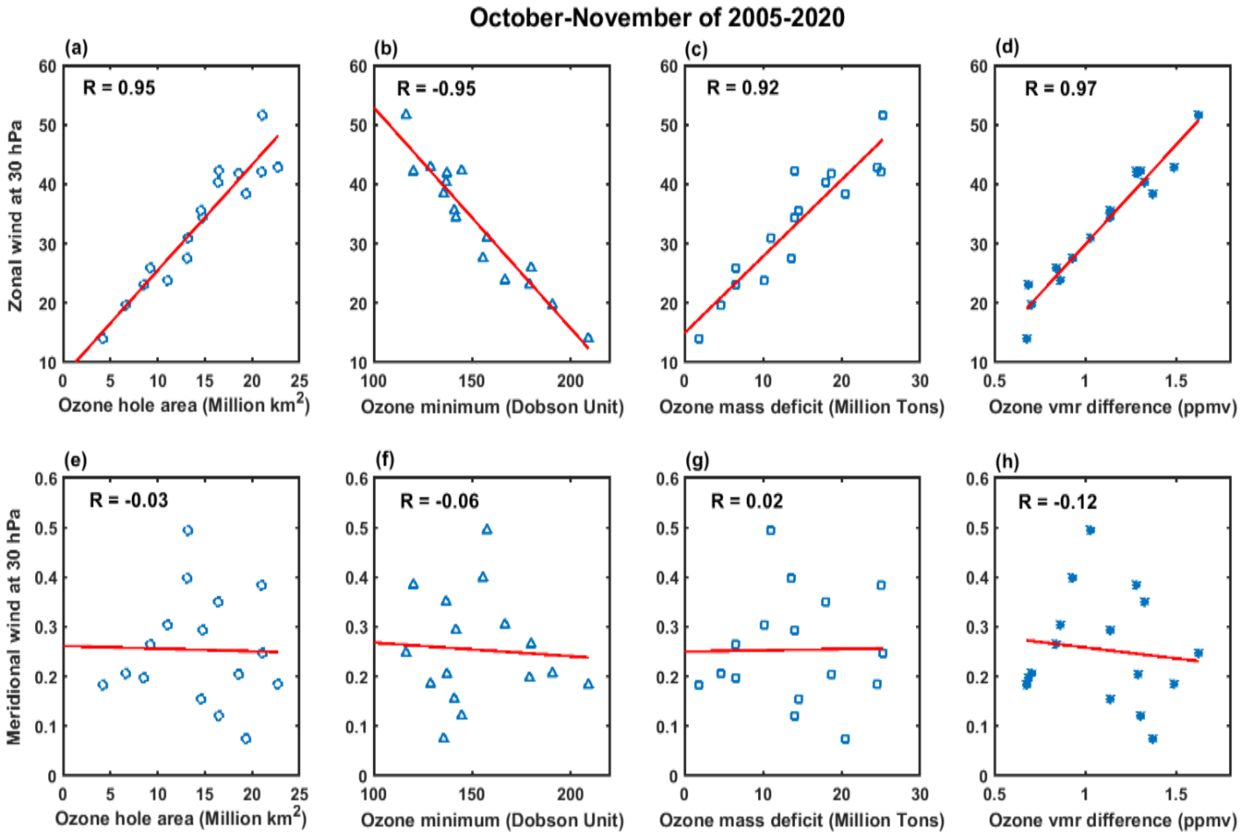

Figure 3.4: (a-d) Scatter plots of ozone hole area, ozone minimum, ozone mass deficit and MLS ozone volume mixing ratio (vmr) difference between 57.5ºS and 77.5ºS (1–68 hPa) with 30 hPa ERA-5 reanalysis (a-d) zonal wind (m/s) and (e-h) meridional wind (m/s) during October-November of 2005–2020

Next, the R values are calculated for ozone vmr difference between 57.5º S and 77.5º S and zonal winds of UMLT heights and the scatter plots are shown in Figure 3.5. The values are -0.48 ($p = 0.05$) for 82 km, -0.59 ($p = 0.01$) for 85 km, -0.7 ($p = 0$) for 88 km, -0.81 ($p = 0$) for 91 km, -0.8 ($p = 0$) for 94 km and -0.62 ($p = 0$) for 98 km. Significant correlations are also obtained between stratospheric ozone loss and UMLT zonal wind. That is, more westward winds observed during the years of large stratospheric ozone loss. Similar to the stratospheric meridional winds, the meridional winds in the UMLT region are also observed to possess no significant correlation with the ozone loss parameter.

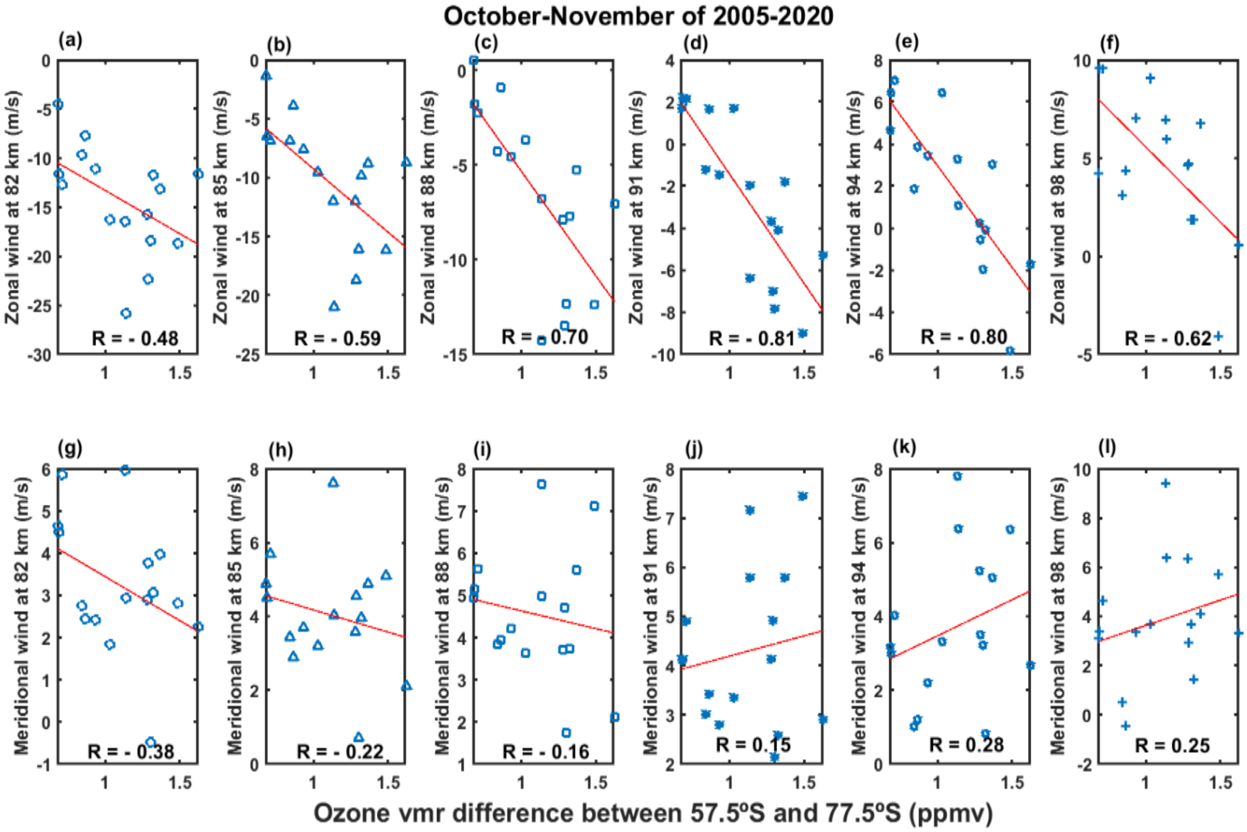

Figure 3.5: Scatter plots of MLS ozone vmr difference (ppmv) between 57.5ºS and 77.5ºS with Rothera VHF meteor radar (a-f) zonal wind (m/s) and (g-l) meridional wind (m/s) at 82 km, 85 km, 88 km, 91 km, 94 km and 98 km during October-November of 2005–2020

3.3.3. Relation among meridional heat flux, temperature, ozone loss, stratospheric and mesospheric winds and SW2 tide

Next, to investigate the role of dynamics in controlling the austral polar ozone loss processes, the long-term variability of meridional heat flux ($-\overline{V`T`}$), which acts as a proxy for the PWs, is shown in Figure 3.6 a. The meridional heat flux includes the contribution from wave perturbations of almost all scales and it also signifies the heat transfer from low to high latitudes. The heat flux at 30 hPa is calculated for the month of September, just prior to the ozone loss season, to investigate its impact on the ozone loss processes. The ERA-5 (30 hPa) and MLS (31.6 hPa) temperature in September, ozone vmr difference between 57.5º S and 77.5º S in October-November, ERA-5 (30 hPa) zonal wind in October-November, UMLT zonal wind anomaly obtained from Rothera meteor radar in October-November and SW2 amplitude anomaly calculated from TIMED-SABER temperature data in October-November are respectively shown in Figures 3.6 b-f. Data from ERA-5, MLS and SABER are available for the years 2002–2020, 2005–2020 and 2003–2020 respectively.

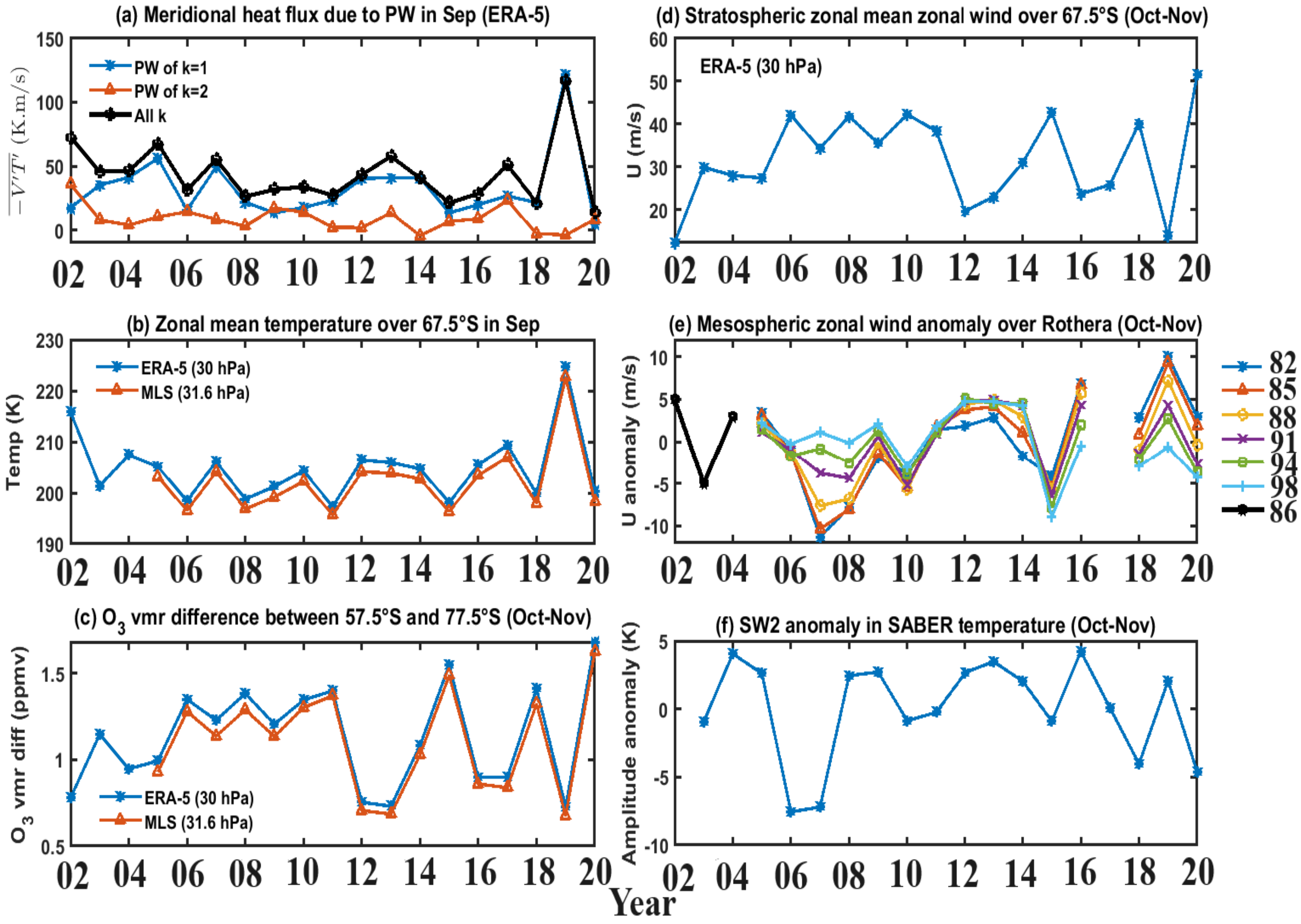

Figure 3.6: (a-b) Variations of meridional heat flux (ERA-5) and zonal mean temperature (ERA-5 and MLS) at ~30 hPa over 67.5ºS during September, (c-f) ozone volume mixing ratio (ERA-5 and MLS) difference between 57.5ºS and 77.5ºS at ~70-1 hPa; stratospheric (30 hPa) zonal mean zonal wind (ERA-5) over 67.5S; mesospheric zonal wind (Rothera meteor radar) anomaly at altitudes 82–98 km; SW2 tidal amplitude anomaly in TIMED-SABER temperature in the height region 84–88 km for October-November. The ERA-5, MLS and SABER data sets are shown for the years 2002–2020, 2005–2020 and 2003–2020 respectively. See text for more details

As seen from the figure, in the month of September, the meridional heat flux varies between 10 and 70 K.m/s in most of the years. The lowest value of meridional heat flux is observed during

2020 (13.63 K.m/s) and the highest in 2019 (116.91 K.m/s). A small peak (72.3 K.m/s) is observed in 2002. The variation of meridional heat flux due to PW of k = 1 is found to be quite similar to the variation of the total meridional heat flux. For 2019, the value of meridional heat flux is similar to the variation of heat flux due to PW of k=1 (121.98 K.m/s) and for 2002, it is similar to that of PW of k = 2 (35.96 K.m/s). The above mentioned enhancements in meridional heat flux are associated with the two austral SSW events, observed till date. However, the correlation coefficients between the total heat flux and the heat flux due to PW of k = 1 comes out to be 0.86 (p = 0) and that due to PW of k = 2 is 0.09 (p = 0.70), which signifies that the total meridional heat flux is mostly contributed by PW of k = 1.

The temperature at stratospheric heights (30 hPa and 31.6 hPa) in September (Figure. 3.6 b) obtained from ERA-5 and MLS datasets respectively exhibit minimum temperature values corresponding to the years having enhanced ozone loss viz., 2006 (198.43K, 196.56 K), 2008 (198.76 K, 196.85 K), 2011 (197.32 K, 195.7 K), 2015 (198.08 K, 196.35 K), 2018 (199.87 K, 197.94 K) and 2020 (200.24 K, 198.21 K). This also correspond to the years having low meridional heat flux in September.

Next, the latitudinal difference of ozone vmr between 57.5º S and 77.5º S in October-November (Figure. 3.6 c) is observed to possess inverse relation with temperature and meridional heat flux in September. It shows higher values during 2003 (1.15 ppmv), 2006–2011 (greater than 1.21 ppmv from Era-5 and 1.13 ppmv from MLS), 2015 (1.55 ppmv from ERA-5 and 1.49 ppmv from MLS), 2018 (1.41 ppmv from ERA-5 and 1.32 ppmv from MLS) and 2020 (1.68 ppmv from ERA-5 and 1.62 ppmv from MLS), indicating the years of large ozone loss. It can be due to the fact that lower temperature in stratosphere resulting from lower wave activity (indicated by low meridional heat flux) can cause more PSC formation and hence more ozone loss over that region.

Almost corresponding to the years of larger ozone loss, the zonal wind in October-November around 30 hPa (Figure. 3.6 d) represents the largest eastward winds, which represent stronger polar vortex. From the figure the strongest eastward winds are observed during 2003 (29.95 m/s), 2006–2011 (greater than 35 m/s), 2015 (42.74 m/s), 2018 (40.22 m/s) and 2020 (51.57 m/s). The strong eastward wind may be attributed to thermal wind balance, as higher ozone loss can causes more pole-to-equator temperature gradient.

Next, for obtaining the monthly zonal wind anomaly during October–November over Rothera, the composite monthly mean at each height for 16 years (2005–2020) is calculated and it is deducted from the monthly zonal wind variation of each year at the respective heights. The thick black line shows the approximately digitized zonal wind anomaly values at 86 km for the period 2002–2005 (November) taken from Figure 4a (Venkateswara Rao et al., 2015). From the figure, it can be observed that the zonal winds at stratospheric heights show anti correlation to zonal wind anomalies observed at UMLT heights, which is nearly similar to the results presented earlier by Venkateswara Rao et al. (2015) and is also valid for a larger period of time. The wind anomaly is found to be largely negative during the years 2007 (-11.3 m/s for 82 km), 2015 (-9 m/s for 98 km) and 2020 (-4.3 m/s for 98 km). Hence, it can be said that there exist a relationship between the stratospheric and UMLT winds, which is further governed by ozone loss processes during October-November.

Figure. 3.6 f shows the variation of SW2 tidal amplitude anomaly in the height region (84–88) km over 60º S during October-November. As observed from the figure, there is a major negative anomaly in SW2 amplitudes during the years 2006 (-7.55 K), 2007 (-7.20 K), 2018 (-4 K) and 2020 (-4.62 K). Therefore, it can be said that the mesospheric SW2 amplitude anomaly varies inversely to the stratospheric latitudinal ozone vmr difference between 57.5º S and 77.5º S, which may be possible as the generation of SW2 tide is associated with the solar radiation absorption by stratospheric ozone. Therefore, it can be summarized as, there exist a relationship between meridional heat flux in September and middle atmospheric circulation and tidal activity via the ozone loss processes occurring in October-November over austral polar latitudes.

3.4. Discussion

In this chapter, we have presented the seasonal and interannual variabilities of the long-term (16 years) middle UMLT winds over Rothera station, located in the Antarctic Peninsula, which exhibits westward flow during October/November-February/March and eastward flow during March/April-September/October. Particularly, large westward winds are observed during November–December of the years 2006–2011, 2015, 2018 and 2020. The meridional wind shows annual variation with northward flow during October/November–February/March and southward flow during rest of the months. However, compared to zonal wind, the meridional wind exhibits less interannual variability. The highest interannual variability in zonal and meridional winds are observed in the month of November-December and July–September, respectively (except for 82 km where an additional large interannual variability in meridional winds is seen in December-January). Earlier over Rothera, Sandford et al. (2010) observed also maximum westward wind of 50 m/s during November–December nearly at 80 km and maximum eastward wind of 20 m/s during August nearly at 97 km, with largest variability in zonal winds at the end of springtime (November). For meridional winds, they observed maximum northward wind of 14 m/s above 94 km during December–February. Similar to our results, large interannual variability in meridional winds was also observed by them at lower heights during December and upper heights during July.

Previous studies have also shown that the winds in the UMLT region are largely governed by the underlying stratospheric wind variability from mid to high latitudes (Xu et al. (2011), de Wit et al. (2014, 2015)). Over Trondheim, Norway (63.4º N, 10.5º E), de Wit et al. (2014) showed the commencement of the mesospheric zonal wind reversals before the stratospheric wind reversal using meteor radar and MERRA reanalysis datasets during sudden stratospheric warming events. They attributed it to the gravity wave forcing, simulated using the WACCM specified dynamics (WACCM-SD) model. However, the connection of these middle atmospheric wind variations during the austral springtime stratospheric ozone loss has been least explored. In this chapter, the analysis of ERA-5 stratospheric winds at 30 hPa over 67.5º S showed large interannual variability of zonal wind in November and meridional wind in October. Moreover, during October–November of 2006–2011, 2015, 2018 and 2020, large eastward winds with large interannual variability at stratospheric heights coincides with the time of large ozone loss and also large westward winds in the austral polar UMLT region. Earlier, during 2002–2014, Venkateswara Rao et al. (2015) reported that the springtime polar eastward winds in the stratosphere are associated with a large westward wind anomaly observed in the mesospheric region using the Rothera MF radar data. The results from the present study using Rothera meteor radar observations and ERA-5 Reanalysis datasets for an extended period of time (2002–2020) are in good agreement with the results of Venkateswara Rao et al. (2015). They also pointed out that the ozone difference between 57.5º S and 77.5º S latitudes has a major influence in driving the stratospheric zonal wind field. Using Freie Universita¨t Berlin Climate Middle Atmosphere Model (FUB CMAM) simulations and NCEP/NCAR reanalysis datasets, Langematz et al. (2003) also discusses how the upper stratospheric temperature from low to high latitudes can be affected by radiative effects owing to the changes in concentrations of ozone and carbon dioxide. Using chemistry/transport models (CTM), Goddard Earth Observing System chemistry/climate models (GOES CCM) simulations, Stolarski et al. (2006) also showed the dynamical effect of the changes in stratospheric wind field due to radiative perturbation associated with Antarctic ozone hole. Therefore, in this chapter, it is suggested that the ozone loss in the Antarctic stratosphere led to large pole-to-equator temperature gradient, which might have resulted in the generation of strong eastward wind flow with height in the polar stratosphere via thermal wind balance.

In addition to the radiative effects, the PWs also play an important role in the determining the temperature and wind circulation in the polar stratosphere (Li et al. (2021)). Earlier, based on NCEP Climate Prediction Center (CPC) data, Newman et al. 1997 showed that reduced PW over the Arctic can generate stronger, colder and stable stratospheric vortex. In this chapter, the role of PW in driving the ozone loss in Antarctic is investigated by calculating a term "meridional heat flux" before the onset of ozone depletion season, that is, in September. The term "meridional heat flux" acts as a proxy for planetary wave activity, which signifies the latitudinal heat flow. It is observed that in all the years (2002–2020) the variation of meridional heat flux due to PW of k = 1 mostly matches with the variation of the total meridional heat flux. Further, it is observed that the amount of stratospheric ozone loss increases with the decrease of meridional heat flux (particularly PW of k = 1). It may be because due to the decrease of meridional heat flux, the temperature at 30 hPa pressure level decreases because of less stratospheric wave activity. Studies have shown that PSCs, that are formed in low temperatures, denoxify and denitrify the lower polar stratosphere and activate chlorine radicals leading to significant loses of ozone during polar spring (Coy et al. (1997), David et al. (2005)). Hence, the low temperature in the stratosphere (~ 195 K), owing to dynamics, rather than radiative forcing, makes it favorable for the enhanced formation of PSCs during September, which in turn can facilitate the ozone destruction over the Antarctic continent during spring time (October–November). Therefore, it can be said that there is a significant role of meridional heat flux due to PW activity during springtime in driving the ozone loss processes at Southern high latitudes.

The period 2002–2020 includes two impactful austral SSW events, one occurred in 2002 and another in 2019. In September 2002, the Antarctic ozone hole split in two due to an unprecedented major austral SSW, occurred due to strong planetary wave of zonal wavenumber-2 (Varotsos, (2002), Sinnhuber et al. (2003)). In 2019, moderate El-Nino along with Madden-Julian oscillation (phase 4–6) led to the formation of extratropical Pacific-North American (PNA) response, which enhanced the extratropical planetary wave activity and disrupted the polar vortex. This along with easterly phased QBO and solar minimum conditions of 2019 caused an exceptionally strong stationary wave of zonal wavenumber 1, resulting in a mixed (displacement to split) type SSW in 2019 (Rao et al. 2019). In this study also it is observed that the meridional heat flux due to PW of k = 2 is larger in 2002, whereas that meridional heat flux due to PW of k = 1 is larger in 2019. That is, the meridional heat flux can serve as a good proxy to determine the PW of different zonal wavenumbers.

Further, studies have shown that the UMLT region is highly linked to the stratosphere and even troposphere by upward propagating waves and tides (Hibbins, 2005). It is suggested that the eastward stratospheric winds prevailing during the spring ozone loss period can filter the eastward propagating GW. Therefore, the upward propagation of westward phased GW in their critical level interaction with the background flow might have deposited their westward momentum leading to westward acceleration (Wu et al. (2013), Smith et al. (2010)). This might have caused the large interannual variability in the zonal winds in the UMLT region with large westward acceleration during October–December.

In addition to that, present study also reveals that there is considerable reduction in the amplitude of the SW2 tidal anomaly at 60º S in the upper mesospheric heights in the years of large Antarctic ozone loss. Earlier**,** Hoffmann et al. (2007) also noted the enhancement of the semi-diurnal tidal amplitude over Andenes (69º N, 16º E) during SSW of 2006, which is in accordance with our results. This might be because the SW2 tide is generated primarily by the absorption of solar radiation by stratospheric ozone, so it showed less activity in the years of larger ozone loss. Thus, results from the present study indicate a possible role of meridional heat flux signifying PW activity in controlling the Antarctic ozone loss changes during springtime, which further regulates both the middle atmospheric wind circulation and the tidal activity at Southern high latitudes extending vertically up to the UMLT heights.

Chapter 4: Role of solar tides in driving the polar UMLT circulation in summer

4.1. Introduction

The dynamics of the polar UMLT region is largely governed by atmospheric solar tide, GW and PW that vary at different spatial and temporal scales. In addition to the GW and PW, atmospheric tides are also responsible for the energy and momentum transmission from the lower atmosphere to the UMLT region. Therefore, they act to couple lower atmosphere to the upper atmosphere. When they propagate upward, their amplitudes increase exponentially because of the decrease of atmospheric density with height. After the attainment of maximum amplitude in the UMLT region, they undergo dissipation. The 12-hr tide (SDT) dominates over the high latitudes, while the 24-hr tide (DT) dominates over the low latitudes. High latitude studies have shown that the SDT amplitudes maximizes during autumn and winter (Avery et al. (1989), Mitchell et al. (2002), Pancheva et al. (2020)) and factors like solar flux variations, phase of the QBO and Southern Annular Mode (SAM) could contribute its year-to-year variability. Still compared to SDT, studies are less regarding interannual variability of DT over high latitudes. This is probably because its smaller amplitude over there. However, low-latitude migrating diurnal tide (DW1) shows maximum amplitude during equinox months and a summer minima (Sridharan, (2019)). The energy and momentum deposition by the tides into the background flow have been studied extensively using both numerical models and observations (Griffith and Mitchell, (2022), Lieberman and Hays, (1994), Teitelbaum and Vial, (1981)) as they can cause large wind, temperature and density fluctuations. On account of the dissipation of diurnal tides (especially the (1,1) mode) in the lower thermospheric wind flow over low latitudes, Miyahara, (1978a,b) estimated that the tidal induced wind perturbations of the orders of tens of meters per second, both theoretically and numerically. The authors further showed that this wind anomaly could be contributed by the DT below 120 km and SDT above 120 km. Becker, (2017) also estimated the energy deposition by upward propagating waves and the contribution of thermal tides in depositing energy in the lower thermospheric region, using a mechanistic middle-atmosphere Global Climate Model (GCM). Recently, Sridharan, (2020) suggested the role of DW1 in the height range 80–91 km, in driving large westward winds over Kototabang (0.2°S, 100.3°E) during the strong La Niña years. Fritts and Alexander, (2003) demonstrated that tides could modulate the upward propagation of GW momentum fluxes and therefore could influence the wave forcing on circulation. Additionally, Becker, (2017) also observed the negative (westward) Eliassen–Palm flux (EPF) divergence owing to tides in the high latitude UMLT region during summer months.

Therefore, it can be said that the role of DT in driving the UMLT winds has been well recognized, but mostly the studies are concentrated over low latitudes. Hence, in this chapter, we aim to investigate the role of diurnal tides in driving the UMLT winds over the polar latitudes.

4.2. Data used

Wind data from ground-based meteor radar data over two opposite polar latitude stations, Esrange and Rothera, for the years 2005–2019, are used in this chapter. DT and SDT amplitudes in winds are extracted from the spectral analysis of the wind data. Although the data has good time and height resolution, however they are unable resolve the migrating and non-migrating tidal modes. For that, SABER-TIMED temperature data is used, from where the amplitude of the different tidal modes are calculated. The GW and PW variances are extracted from the spectral analysis of the meteor radar wind observations. Details of these datasets and methodology are discussed in chapter 2.

4.3. Results

4.3.1. Seasonal variation of winds and tides over Esrange and Rothera

Figure 4.1 depicts the seasonal variation of winds, SDT and DT amplitudes over Esrange and Rothera. The monthly mean zonal winds over Esrange (Figure 4.1 a) show similar seasonal variation like Rothera (Figure 4.1 g), with strong westward winds below 91 km during the summer months, that is, April-September over Esrange and October-February over Rothera. The meridional wind shows southward (equatorward) flow (−2 to −14 m/s) over Esrange (Figure 4.1 b) and northward (equatorward) flow (5–12 m/s) over Rothera (Figure 4.1 h) during May–August and November–February, respectively at all heights. Although, stronger westward winds with height are observed over Rothera.

The SDT amplitude over Esrange (Figures 4.1 c,d) shows a gradual increase with height (from 82 to 98 km) during December–March and August–September. However, over Rothera (Figures 4.1 i,j) it increases more prominently than over Esrange.

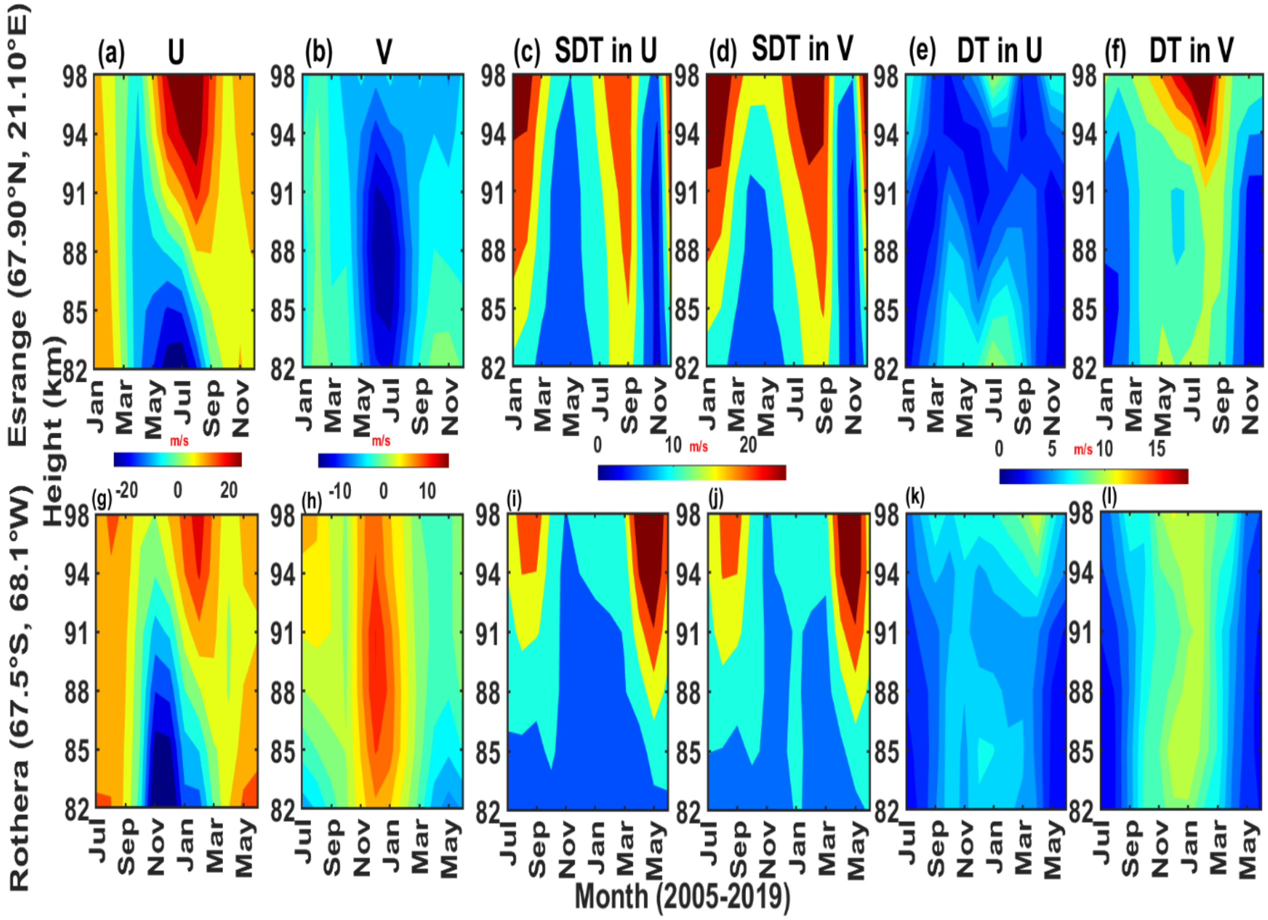

Figure 4.1: Seasonal variation of (a, g) monthly mean zonal wind, (b, h) meridional wind, (c, d, i, j) semi-diurnal tidal (SDT) amplitude and (e, f, k, l) diurnal tidal (DT) amplitude using meteor radar over (top panel) Esrange (67.9°N, 21.1°E) and (bottom panel) Rothera (67.5°S, 68.1°W) between 82 and 98 km averaged for the years 2005–2019

Next, the large DT amplitudes (6–10 m/s) are observed over Esrange during boreal summer months (Figures 4.1 e,f) and they are also found to decrease with height. Minimum amplitude (2–3 m/s) in both zonal and meridional winds are observed from November to February. Over Rothera, minimum DT amplitudes (2–3 m/s) are observed during May–August (Figures 4.1 k,l) and larger amplitudes during December–February (summer months). Similar to Esrange, the DT amplitudes over Rothera are observed to diminish with height. However, amplitudes in meridional winds are found to be more than that in zonal components, over both Esrange and Rothera.

Briefly, decrease of large DT amplitudes are observed with height over both the poles during summer, when strong westward and equatorward winds prevail in the background flow. However, the SDT amplitudes are observed to increase with height over both locations.

4.3.2. Year-to-year variability of monthly mean winds over Esrange and Rothera

Next, the variabilities of monthly mean zonal winds in the height region 82–98 km for the period 2005–2019 over Esrange and Rothera are presented in Figure 4.2.

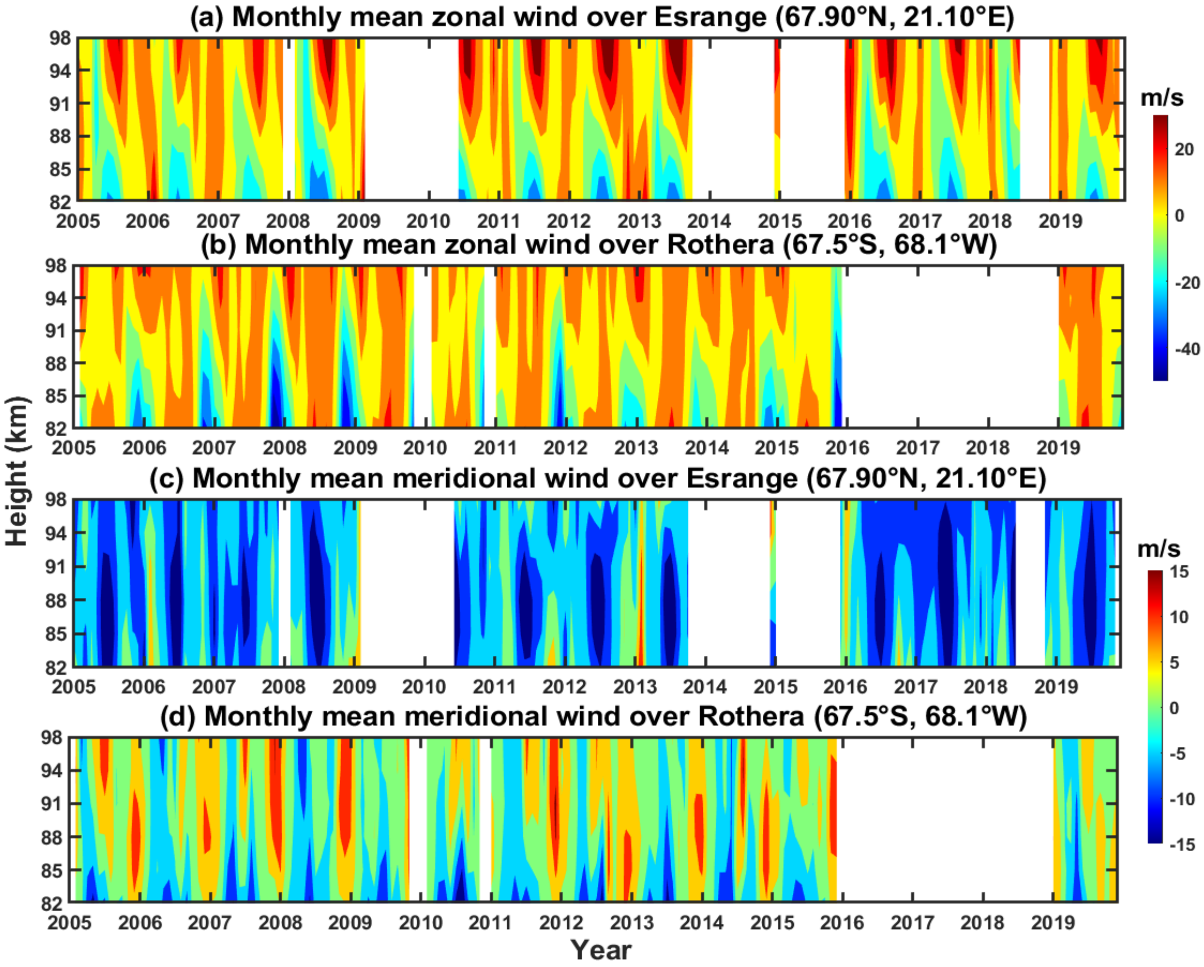

Figure 4.2: Monthly mean (a, b) zonal and (c, d) meridional winds over (a, c) Esrange (67.9°N, 21.1°E) and (b, d) Rothera (67.5°S, 68.1°W) in the height region 82–98 km for the years 2005–2019

Compared to Rothera, the year-to-year zonal wind variation shows little changes over Esrange. That is, the summertime zonal wind is strongly westward below 85 km and strongly eastward above 91 km except for 2005–2007. The zonal winds over Rothera show larger interannual variability during the austral summer months. This may be attributed to the variability in underlying stratospheric wind field associated with austral ozone loss. Stronger summertime westward wind regimes (∼−20 to −55 m/s) with height are observed over Rothera, particularly during 2005–2008, 2012 and 2015. However, the eastward winds over 91 km are stronger over Esrange. Therefore, it can be concluded that both the strength and interannual variability of westward winds are less over Esrange.

For the meridional winds, large interannual variability over both the stations is observed during the winter months (in February over Esrange and in August over Rothera).

4.3.3. Year-to-year variability of monthly mean tides over Esrange and Rothera

Figure 4.3 depicts the year-to-year variabilities of the SDT (left panel) and DT (right panel) amplitudes observed in zonal and meridional winds over Esrange and Rothera. As seen from Figures 4.3 a–d, the SDT amplitudes increase with height over both the stations, however larger amplitudes are observed over Esrange below 88 km, compared to that over Rothera. The SDT amplitude maxima in September over Esrange is observed to be weaker (9–16 m/s) in the years 2005, 2007, 2016, and 2019, whereas it is in the range of ∼22–32 m/s in other years. Over Rothera the SDT amplitudes are smaller (∼5 m/s) during 2010–2012 and 2016.

The summertime DT amplitudes over Esrange (Figures 4.3 e,f) show large values (∼10–12 m/s) below 91 km in the years 2008, 2011, 2013, 2016, and 2017, compared to Rothera. Particularly in meridional winds, the DT amplitudes above 91 km show larger values over Esrange and they persist for a longer time than at lower heights. Over Rothera (Figures 4.3 g,h), large DT amplitudes in meridional winds at all heights are observed during summer (10–12 m/s) and the decrease in the DT amplitude with height (below 91 km) is prominent except for 2012 and 2016.

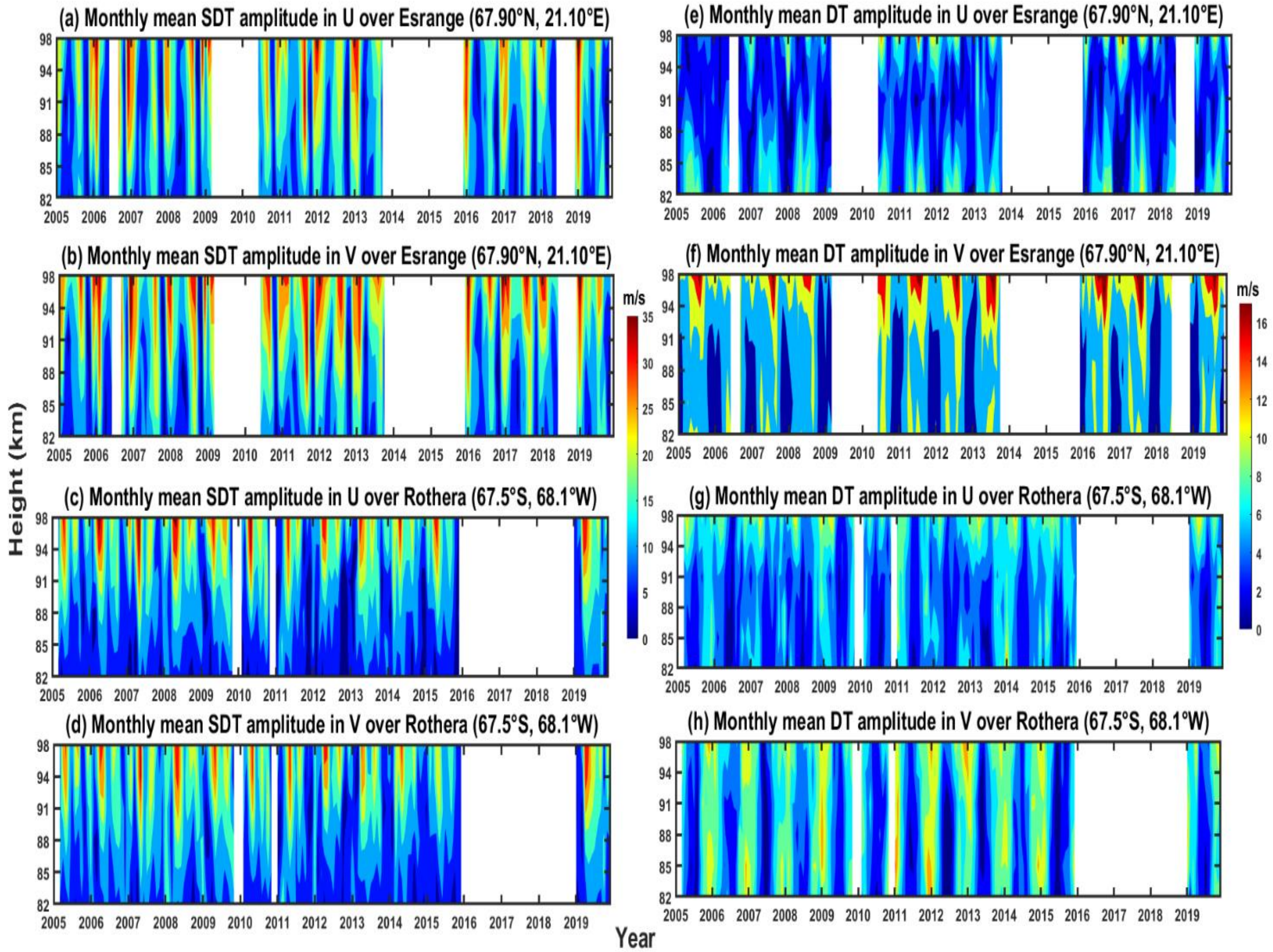
(a) Monthly mean SDT amplitude in U over Esrange (67.90°N, 21.10°E)

(b) Monthly mean SDT amplitude in V over Esrange (67.90°N, 21.10°E)

(c) Monthly mean SDT amplitude in U over Rothera (67.5°S, 68.1°W)

(d) Monthly mean SDT amplitude in V over Rothera (67.5°S, 68.1°W)

(e) Monthly mean DT amplitude in U over Esrange (67.90°N, 21.10°E)

(f) Monthly mean DT amplitude in V over Esrange (67.90°N, 21.10°E)

(g) Monthly mean DT amplitude in U over Rothera (67.5°S, 68.1°W)

(h) Monthly mean DT amplitude in V over Rothera (67.5°S, 68.1°W)

Figure 4.3: Monthly mean (a–d) semi-diurnal and (e–h) diurnal tidal amplitude in (a, c, e, g) zonal wind and (b, d, f, h) meridional wind over (a, b, e, f) Esrange (67.9°N, 21.1°E) and (c, d, g, h) Rothera (67.5°S, 68.1°W) in the height region 82–98 km for the years 2005–2019

4.3.4. Interannual Variability of winds and tides over Esrange and Rothera

Quantification of the interannual variability of winds and tidal amplitudes over Esrange and Rothera is presented in Figure 4.4. The blue line represents the 15 years composite mean (2005–2019) and the red bars indicate the interannual variability calculated from the standard deviations of each month. Large interannual variability in zonal winds is observed during February (13 m/s) over Esrange when there is strong eastward background wind and during November–December

(10 m/s) over Rothera when there is strong westward background wind (−27 m/s). Similar to the zonal winds, the meridional winds over Esrange exhibit high interannual variability during January–February (6–7 m/s), but in case of Rothera it is in the month of August-September (5–6 m/s).

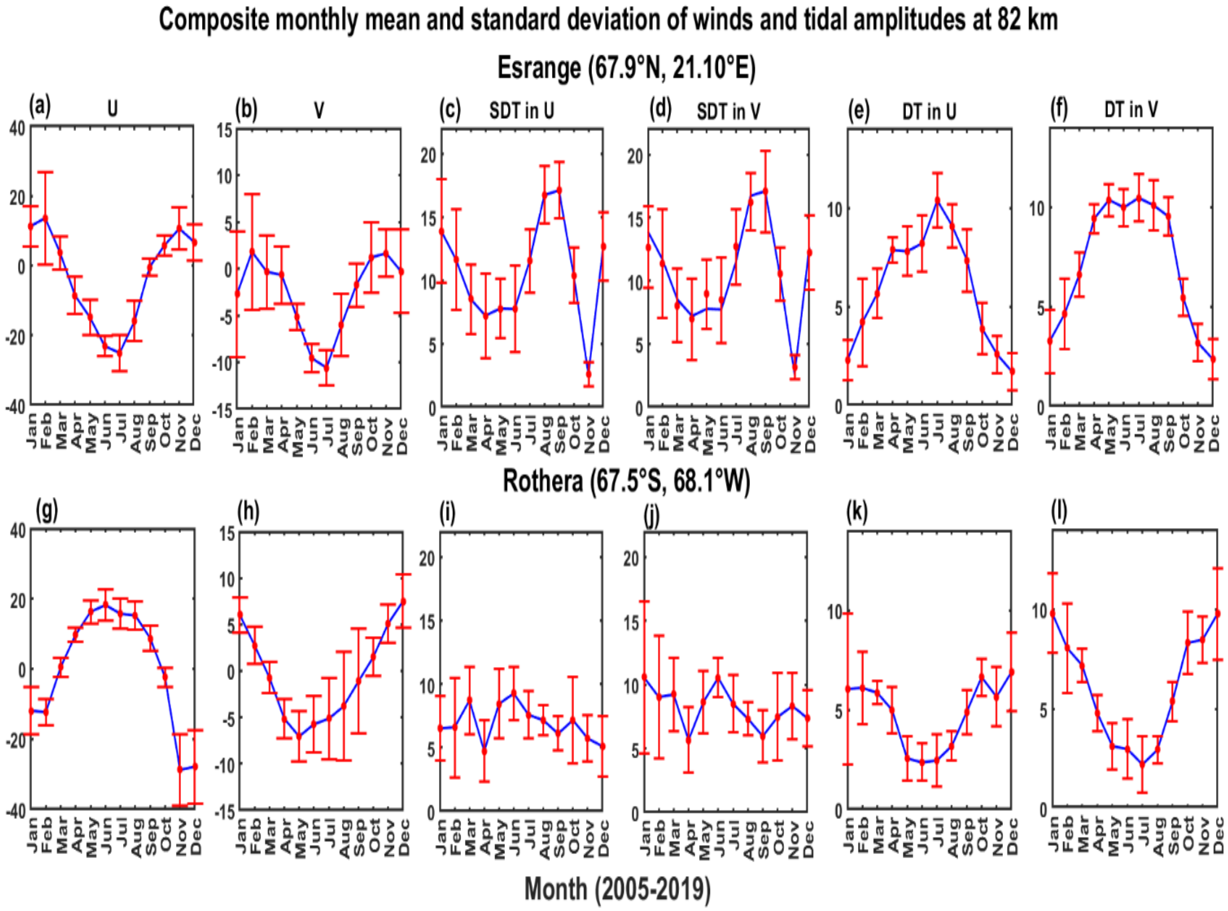

Figure 4.4: Interannual variability of monthly mean (a, g) zonal wind, (b, h) meridional wind, (c, d, i, j) semi-diurnal tidal (SDT) amplitude and (e, f, k, l) diurnal tidal (DT) amplitude at 82 km over (top panel) Esrange and (bottom panel) Rothera for the time period 2005–2019. The blue line denotes the mean wind velocity and vertical red line denotes the standard deviation of winds for each month

The SDT amplitude over Esrange both in zonal and meridional winds shows large amplitude during December–February (10–15 m/s) with the largest interannual variability observed during January–February (3–4 m/s). However, lowest interannual variability (1 m/s) is observed when there is a drop in SDT amplitude in November (2–3 m/s). Large interannual variability over Rothera is observed during January (5.9 m/s) in meridional wind and the least during August (~1 m/s).

In the case of DT amplitude over Esrange, large monthly mean amplitude is observed during summer but the large variation of the mean is observed during February (~2 m/s). Over Rothera, both the DT amplitudes and interannual variability are more during summer (January–February).

Briefly, over Esrange, large year-to-year variability in winds and tidal amplitudes are observed in boreal winter (February) and over Rothera, it is in the austral summer months (except for meridional winds).

4.3.5. Relation between winds and DT amplitude over Esrange and Rothera

Next, we tried to investigate the relation between zonal winds and DT amplitudes, as the strongest westward winds coincided with large DT amplitudes and its decrease with height. For that, the correlation analysis is employed and the scatter plots are shown in Figure 4.5. The correlation coefficient (R) between the zonal wind and DT amplitude, which defines the strength of a linear relationship, is calculated to be -0.74. The p value less than and equal to 0.05 denotes a statistically significant correlation coefficient value. In this study, the correlations are significant as the p-values are found close to 0. Since it is already shown in Figure 4.1 that the westward winds prevail in the background flow when the DT amplitudes are larger, the significant R values between the zonal winds and DT amplitudes also imply the significant linear relationship between the DT amplitude and the zonal wind over Esrange. The R and p-values between the zonal wind and DT amplitude in zonal and meridional winds over Rothera are also calculated and found to be -0.54 (p close to 0) and -0.77 (p close to 0), respectively. Similar to Esrange, significant correlation values between the winds and the DT amplitudes over Rothera also suggest the significant linear relationship between the DT and the zonal winds. The correlation coefficients are found to be larger at lower heights indicating that the DT may be the dominant contributor to the westward background winds.

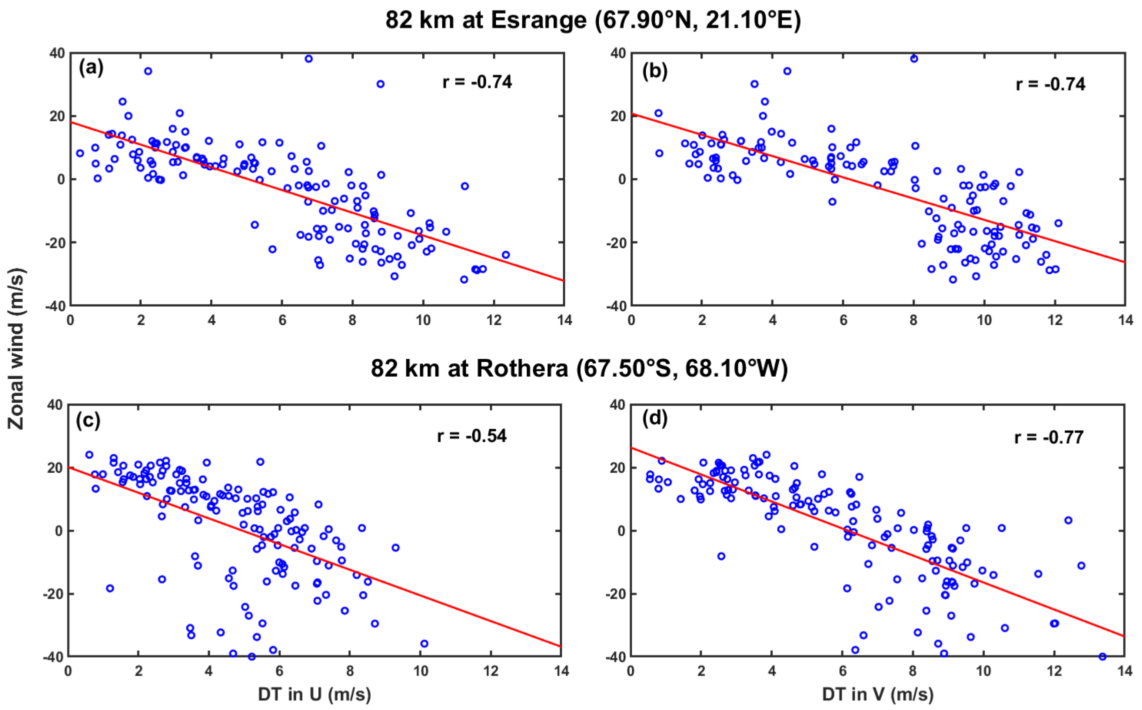

Figure 4.5: Scatter plot of DT amplitude in (a, c) zonal wind and (b, d) meridional wind at 82 km over (a, b) Esrange (67.90°N, 21.10°E) and at 82 km over (c, d) Rothera (67.5°S, 68.1°W) for the years 2005–2019. The red line represents the best fit line

4.3.6. Tidal components in TIMED-SABER temperature

We then focused on investigating whether the migrating DT is responsible for the deposition of momentum in the background winds. Hence the seasonal variation of the westward propagating migrating diurnal tide of wavenumber 1 (DW1) tide at 90 km during 2019 over 60° N (blue line) and 60° S (red line) obtained from the temperature data of TIMED-SABER satellite is shown in Figure 4.6 a. Here, satellite observation is used, as a single station radar data cannot segregate the migrating and non-migrating tidal modes at a particular location. The seasonal variation clearly shows that in the respective summer poles, that is, during May-August (day number 121–221) over 60° N and during December and January (day number 351–365 and 1–21) over 60° S, the DW1 amplitude is more, and its variation is similar to that of the DT amplitude. The similarity in the summer enhancement of DW1 tide like that of the DT indicates that DT may be mostly composed of this westward propagating DW1 tide.

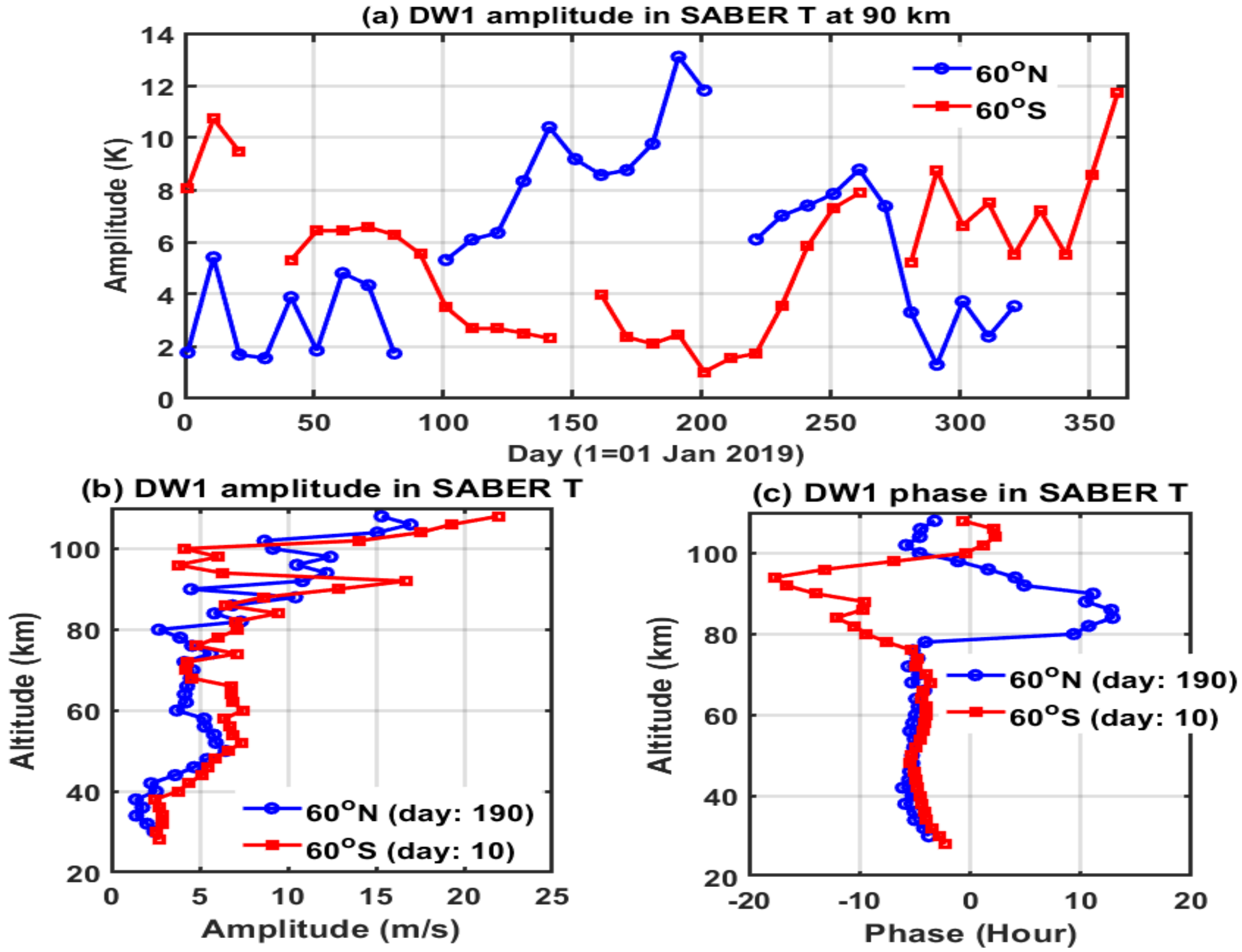

Figure 4.6: (a) Seasonal variation of DW1 tidal amplitude in SABER-TIMED temperature, (b) amplitude-height variation of DW1 from 28 to 108 km and (c) phase-height variation of DW1 from 28 to 108 km at 60°N (blue line) and 60°S (red line) during the year 2019

The altitude profile of the DW1 amplitude (Figure 4.6 b) between 28 and 108 km demonstrates that although DW1 amplitude fluctuates vertically, there is an increasing pattern in the amplitude from 80 to 108 km at 60° N and 76–92 km at 60° S. The clear decrease of the DW1 phase with height (Figure 4.6 c) from 84 to 100 km at 60° N centering around September and 76–98 km around January over 60° S implies the upward propagation of DW1 tide during the summer in the respective polar hemisphere.

Additionally, the seasonal variations of non-migrating tides 90 km during 2019 over 60°N (top panels) and over 60°S (bottom panels) are shown in Figure 4.7. Unlike the DW1 tide, the non-migrating diurnal tides over 60°N and 60°S do not show any clear seasonal variation. However, there is an increased amplitude for DE1 (Figure 4.7 a), DW2 (Figure 4.7 b), and DW3 (Figure 4.7 c) during July and DW2 (Figure 4.7 d) during December. However, except for DE1 tide, the amplitudes of all non-migrating components are lesser than 9 m/s.

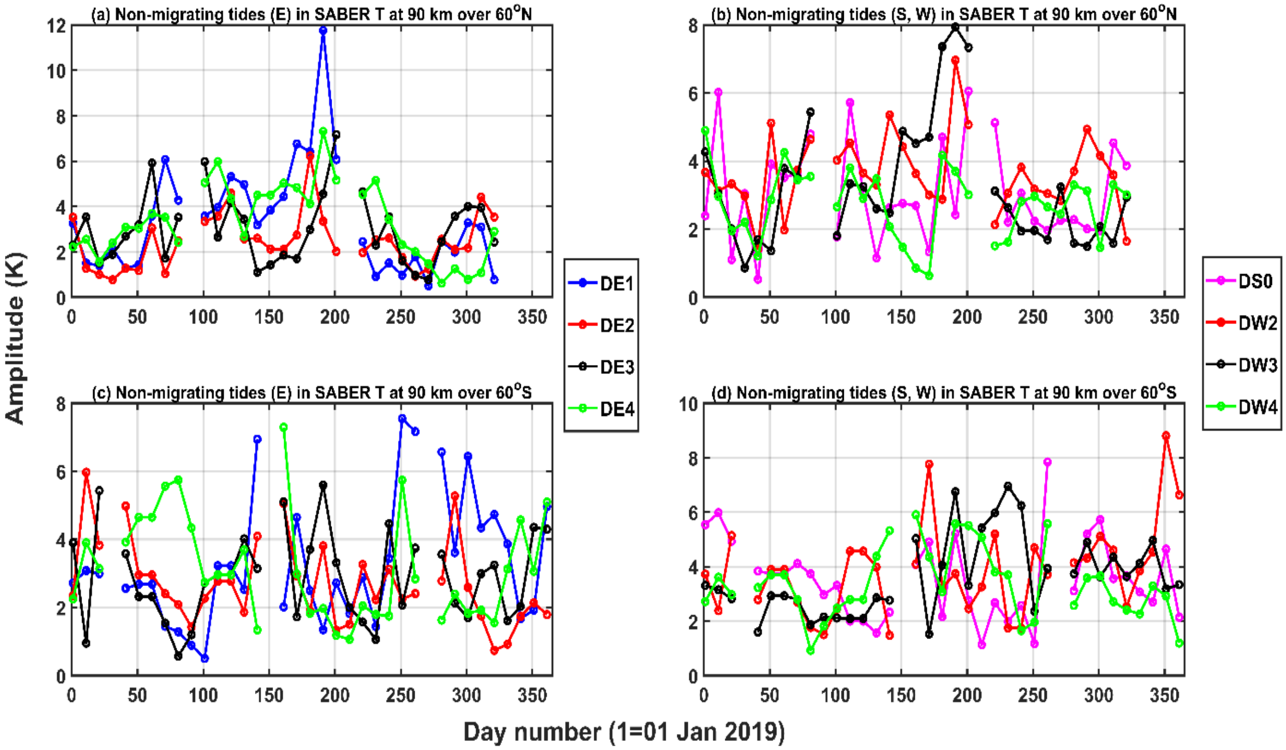

Figure 4.7: Seasonal variation of non-migrating tidal amplitudes at 90 km in SABER-TIMED temperature over (a, b) 60°N and (c, d) 60°S for the year 2019

4.3.7. Wind spectrum over Esrange and Rothera

For investigating the relative dominance of different scales of waves in the wind field (in addition to the solar tides), the amplitude spectra of zonal and meridional winds (covering up to 20 days) over Esrange (top panel) and Rothera (bottom panel), obtained by performing spectral analysis on the monthly wind data, are shown in Figure 4.8. Here two summer months of the polar locations are shown (July 2019 over Esrange and December 2019 over Rothera), in order to determine the dominant wave component in summer months, when there is large westward wind in the background flow.

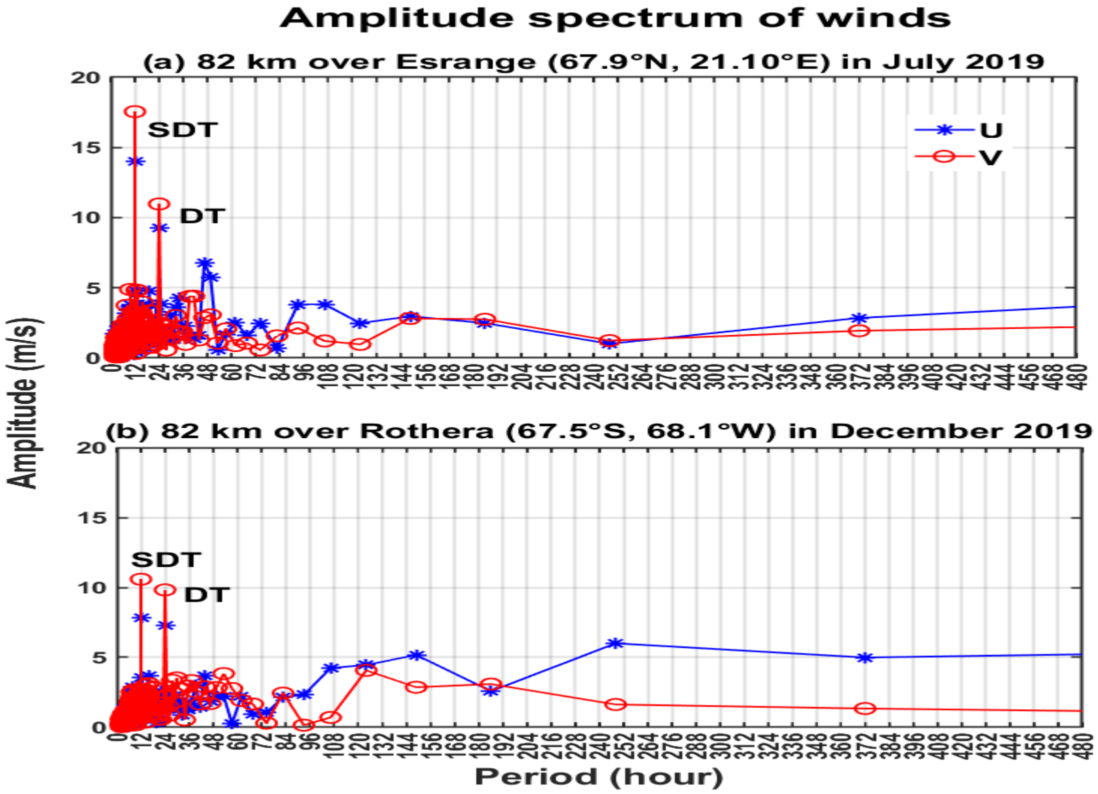

Figure 4.8: Amplitude spectrum of monthly mean zonal and meridional winds at 82 km over (a) Esrange (67.9°N, 21.10°E) in July 2019 and (b) Rothera (67.5°S, 68.1°W) in December 2019

The amplitude spectrum indicates the dominance of SDT component in the both zonal and meridional winds over both the opposite polar latitude stations. Next to the SDT amplitude, the amplitude of DT is larger compared to the waves of other scales (like PW or GW).

Although, it is observed that the wind spectrum is dominated by tides, the role of GW and PW contributing to the momentum deposition in background wind is investigated. For that, the monthly variances of GW and PW during 2019 are calculated from the spectral analysis of horizontal winds after removing the major tidal components.

Over Esrange, the GW variance (Figures 4.9 a,b) shows larger values in winter at higher altitudes (2,720 m^2s^{-2} at 98 km in January). Minimum value is observed in summer, particularly in September 2019 at 82 km. The GW variances over Rothera (Figures 4.9 e,f) also show similar winter enhancement but its magnitude is lesser as compared to Esrange.

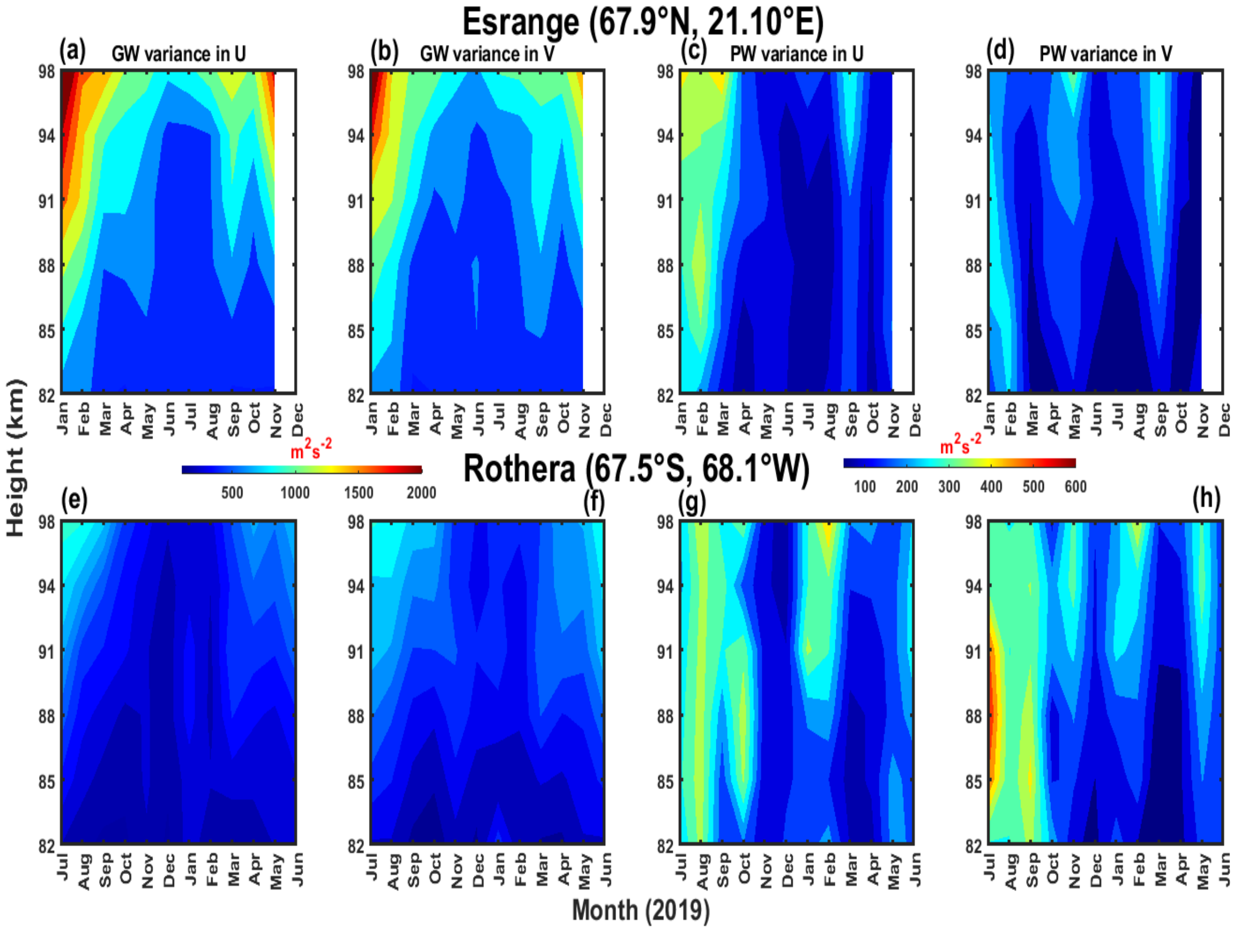

Figure 4.9: (a, b, e, f) Gravity wave variance and (c, d, g, h) planetary wave variance (2–20 days) for the year 2019 from 82 to 98 km over (top panel) Esrange (67.90°N, 21.10°E) and (bottom panel) Rothera (67.5°S, 68.1°W), respectively

In case of PW variance (Figures 4.9 c,d), larger values are observed over Esrange at higher heights during January-March (220–450 m^2s^{-2}) and also for September. Over Rothera (Figures 4.9 g,h), PW variances show large values during winter. Minimum values are observed rest of the times below 88 km. Since, the summer enhancement of GW and PW variances are not observed unlike the DT or DW1 amplitude enhancement, they are unlikely to deposit westward momentum into the background flow, thereby controlling the background winds at UMLT heights. Therefore, westward winds in the summer hemispheres can be attributed to the damping of westward momentum from DT due to DW1 tide over both Esrange and Rothera.

4.4. Discussion

The present study deals with the possible connection between the UMLT winds and solar tides over two opposite polar latitude polar locations Esrange and Rothera, using meteor radar and SABER-TIMED data for the years 2005–2019. Since the radars are present on two opposite latitude stations and are similar in design, so the data obtained from them are free from any biases arising due to the usage of different kinds of measurement techniques or due to differences in latitudes. The zonal winds show large westward wind flow during boreal summer months, that is, during April–September (~-8.5 to -15.9 m/s) over Esrange, and during austral summer months, October–February (~-13.6 to -14 m/s) over Rothera. Stronger westward winds with height are observed over Rothera (-28 m/s at 82 km to -14 m/s at 88 km in December) in comparison to Esrange (-23 m/s at 82 km to -5 m/s at 88 km in June). At lower heights, Sandford et al. (2010) observed strong westward winds (~40 m/s) over Rothera in the month of November–December (2005–2009) and comparatively weaker westward winds (~−25 m/s) over Esrange in June–July (1999–2009). Consistent with our results they also observed westward flow over Esrange below 85 km, unlike over Rothera, where the westward flow can be observed even up to higher heights. In the case of meridional wind, strong equatorward, that is, southward wind prevails over Esrange during May–August (~-5 to -7 m/s) and northward wind over Rothera recorded during November–February (~5–12 m/s), which coincides with the larger westward zonal flow in the background winds. Equatorward winds over both the stations during summertime indicate the wind flow from summer to winter hemisphere. Previously, Kishore et al. (2003) observed that Arctic UMLT winds are predominantly equatorward, whereas the Antarctic UMLT winds are poleward throughout. However, similar to our results Sandford et al. (2010) observed equatorward flow of both Arctic and Antarctic winds throughout the year. They concluded that differences in the mean meridional winds might be due to the usage of MF radar observations by Kishore et al. (2003), which underestimate winds above 90 km (Hines et al., 1993). Later, Kishore Kumar and Hocking, (2010) studied mean UMLT wind and tides over Resolute Bay (75°N, 95° W) and Yellowknife (62.5° N, 114.3°W) and observed westward summer flow at lower heights and a strong equatorward flow in meridional winds, which is consistent with our results. In agreement with the results obtained in the present study, Hibbins et al. (2005) and Dempsey et al. (2021) also noted westward winds in the summer months and eastward winds during the rest of the seasons over southern polar stations.

Venkateswara Rao et al. (2015) have used the Rothera MF radar observations respectively and suggested the selective filtering of the upward propagating GWs in driving the strong westward winds in the UMLT region, when ozone loss processes are dominant over the Antarctic stratosphere. However, in this chapter, we have tried to investigate the influence of solar tides in driving the strong UMLT westward winds prevailing in summer. Particularly, we found that the tides, that is, semi-diurnal followed by diurnal, dominate the wind spectrum. This indicates that these tides can contribute to momentum deposition in the background wind, compared to the waves of other scales. The variances of PW and GW are also checked but those are found to be less during summer over both Esrange and Rothera. Therefore, they can unlikely drive the winds during summertime.

Over Esrange, the SDT amplitude has a semi-annual variation with maximum values during August–September and December–March and over Rothera, it is during March–September mostly at higher heights. Riggin et al. (2003) observed autumnal enhancement of SDT amplitudes over Poker Flat (65° N, 147° W) and Andenes (69° N, 16° E) but weaker over Southern hemispheric sites. Laskar et al. (2016) considered the in-phase interaction between SW2 and SW1 to be responsible for the increase in SDT amplitude during August–September over Andenes (69° N, 16° E) and Juliusruh (54° N, 13° E). Using meteor radar observation and Hamburg Model of the Neutral and Ionized Atmosphere (HAMMONIA), Conte et al. (2018) showed the decrease of SDT amplitude during NH fall transition and they suggested the decrease of both SW2 and SW1 tidal amplitude to be responsible for that. Although, the increase of SDT amplitude with height implies that SDT might not have interacted or deposited energy and momentum into the background winds by mean wind-tidal interaction. In this chapter, the seasonal variation of the DT amplitude exhibits large amplitude during March–September over Esrange and during December–February over Rothera, that is, in the summer months. It is also observed that when the DT amplitude is larger, it decreases with height.

Thus, we have checked the seasonal variation of migrating and non-migrating tides using space borne SABER-TIMED temperature data for the year 2019 to find which tidal component is dominant during the summer season. Results indicated the summer enhancement of DW1 tide, similar to that of the variation DT amplitude observed over Esrange and Rothera. This suggests that the DT must be composed of mostly migrating diurnal tide of zonal wavenumber 1 (DW1).

The phase of the DW1 tide is also observed to decrease with the increase in height from 80 to 100 km, which indicates the upward propagation of the DW1 tide. Although, several studies have shown that at high latitudes, the trapped (evanescent) modes of DT are dominant (MacLeod and Vincent, (1985), Pancheva et al. (2020)), using meteor radar winds over Rothera Dempsey et al. (2021) showed similar upward propagation of DT in several months of the year 2009. The decrease of the DT amplitude with height indicates tidal damping. Unlike the DW1 tide, the non-migrating diurnal tidal modes are not found to show a clear seasonal variation. However, DE1 tide shows an increased amplitude during July over 60° N. It is suggested that it might have transferred eastward momentum to the background winds at higher heights. Still further investigations are required to confirm the same. Becker, (2017) estimated westward Eliassen–Palm flux (EPF) divergence due to tides in the polar UMLT region during summer using a mechanistic middle atmosphere Global Climate Model, which also confirms the role of tides in driving the summer polar UMLT winds. Thus, this chapter provides an observational evidence that westward propagating DT, due to DW1 tidal mode, might have induced westward momentum in the polar UMLT winds during summer due to mean wind-tidal interaction.

Chapter 5: The possible connection between the austral polar SSW and the high occurrence of equatorial valley region irregularities

5.1. Introduction

Radar echoes from the equatorial and off-equatorial low-latitude valley region ionosphere (130–180 km altitude) form a spectacular ‘necklace shape’ in the range-time intensity map with descending and ascending patterns roughly before noon and afternoon respectively, and are known as ‘150-km echoes’ or ‘F1 echoes’. These echoes were first reported by Balsley in the year 1964 (Balsley, (1964)) from the radar observations over Jicamarca (12º S, 76.9º W, 1º dip). The echoes are classified into two types; naturally enhanced incoherent scatter (NEIS or type-A) echoes and field aligned irregularities (FAI or type-B) echoes (Chau and Kudeki, 2013; Patra et al., 2020). The type-A echoes have weaker Signal-to-Noise ratio (SNR), so they can be observed only from highly sensitive radars like Gadanki and Jicamarca. The spectral width of these echoes increases strongly with SNR and they are best observed perpendicular to **B**, but also observed slightly off perpendicular to **B**. The echoes which are off perpendicular to magnetic field possess a wider spectral width (greater than 1000 m/s), but they are weaker compared to that in the perpendicular direction (Chau, (2004)). Their occurrence frequency is largely consistent with the overall morphology of the 150-km radar echoes. The type-B echoes (which have stronger SNR and always embedded and superimposed in type-A echoes) can be even detected with smaller radars including Equatorial Atmosphere Radar (EAR), Indonesia. Chau and Kudeki, (2013) discussed that they occur at a relatively weaker frequency and can be only observed perpendicular to **B**. Although characteristics of these echoes have been studied from different low latitude stations, the generation mechanism for the different types of echoes still remains a mystery. The echo power exhibits quasi-periodic variations indicating the possible role of gravity waves in its generation. Using the height calibrated VIPIR data, Reyes et al. (2020) have shown that the daytime valley region is modulated entirely by the propagation of gravity waves. However, Oppenheim and Dimant, (2016) suggested that the generation of 150-km echoes could be related to the photoelectrons as they are observed only during daytime. It is further supported by their absence during the January 2010 solar eclipse (Patra, (2011)), and their modification by solar flares (Reyes, (2012)). Although, this theory does not explain why maximum occurrence of these echoes is in summer, followed by winter instead of equinox (Pavan Chaitanya et al. (2018)). Recently, Longley et al. (2020) proposed that the upper hybrid (UH) instability could generate the NEIS or type-A echoes.

Several studies have suggested the role of tides has been suggested for the varying occurrence of the 150-km radar echoes. Patra, (2011) suggested that the generation of these FAIs or type-B echoes might be a result of interchange instability on the gradient of the daytime descending ion layer formed by meridional wind shear associated with tides. These tides can act as direct coupling agents between the troposphere and the F region (Lieberman et al. (2013)). The variabilities in the stratospheric ozone, tropospheric water vapor distribution and deep tropical convection significantly influence the tidal variabilities even in the UMLT region (Lieberman and Riggin, (1997)). During the boreal SSW events of 2006 and 2009, studies have also shown that there is an enhancement in the upper mesospheric semi-diurnal tides due to the accumulation of ozone molecules in the equatorial stratosphere. Sridharan et al. (2012) suggested that SSW induces a reversal of meridional circulation towards the equator, which may lead to the transport of ozone from high to low latitudes and prevent the reverse.

Although the link between the tides and type-B has been suggested, no observational study to our knowledge has shown the relation between the echoes and the underlying mesosphere-lower thermosphere tides. To establish this relationship, the present chapter deals with the possible relation of the type-B 150- km echoes, observed by EAR, Kototabang with that of UMLT tides in connection to SSW events that influences the variability of stratospheric ozone.

5.2. Data used

The signal-to-noise ratio (SNR), spectral width and Doppler velocity 150-km radar echoes are obtained from the Equatorial Atmosphere Radar (EAR) deployed over Kototabang, Indonesia. The echo pattern is identified visually with the enhanced power of the necklace pattern lasting at least more than 1 hour. The virtual height of the bottomside F layer (hpF or h'F) data are taken from ionosonde over Kototabang, Indonesia and some sample ionogram observations in order to see the variation of intermediate ion layers at the valley region during some geomagnetically quiet days of September 2019. For hpF variation, data is present nearly continuously for the month of September 2019 and the parameter is scaled at 15 min interval. Stratospheric ozone (9.6 mm channel) values between 1-10 hPa at 10º N, equator and 10º S latitudes and latitudinal temperature data from SABER-TIMED data (for obtaining tidal modes) at 98 km are also used in this chapter. NCEP/NCAR temperature and zonal wind data at stratospheric pressure levels have been used to show the onset of SSW event, which can influence the occurrence of 150 km radar echoes. Details of the ground based, space borne and reanalysis products are provided in chapter 2.

5.3. Results

5.3.1. Percentage of occurrence of type-B 150 km radar echoes

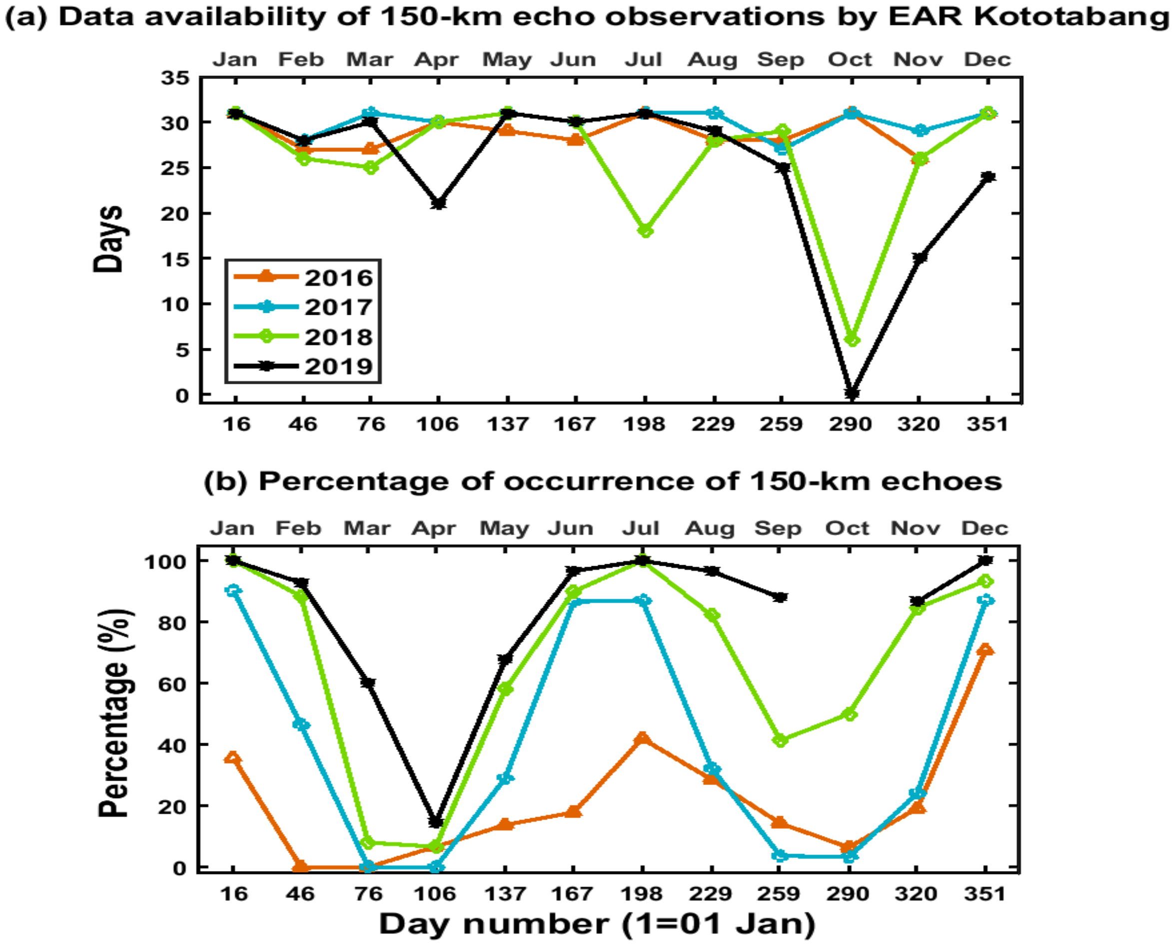

Figure 5.1: (a) Monthly data availability of valley region FAI observations by the EAR at Kototabang (0.2^{o}S, 100.3^{o}E) and (b) monthly variation of percentage of occurrence (PO) of 150-km echoes observed by the EAR for the years 2016–2019

The data availability (Figure 5.1 a) and the percentage of occurrence (PO) of 150-km echoes (Figure 5.1 b) observed by the EAR at Kototabang for the years 2016–2019 are presented in Figure

5.1. The PO of these echoes are larger in boreal summer (June-August), followed by in boreal winter (December-January). In the year 2016, the PO shows becomes large during July (35.4%) and December (48.3%). It is low during October (3.2%) and zero in the months of February–March. In 2017, higher PO is observed during January (67.7%), June-July (more than 67%) and in December (77.4%) and zero during equinox moths. For 2018, PO is 96.7% in January, 94.4% in July and 90.3% in December. For 2019, the large PO is observed throughout the year, when compared to other years, particularly in September (76%), which includes an austral SSW event. Therefore, it can be said that there is a semiannual variation in the PO of these echoes and also the PO increases in magnitude from solar moderate to solar minimum years, that is, from 2016 to 2019. Additionally, in the year 2016, the maximum PO is observed in December and it shifts to summer months as the solar minimum approaches. We have also checked the PO of the echoes during the years 2011–15. No echoes were observed during April, May and October. Very less echoes were seen during other months (PO less than 35%), except in January 2011 (80.6%), February 2011 (52.3%) and July 2014 (55.1%).

5.3.2. Characteristics of type-B 150-km echoes over Kototabang

In order to investigate the high PO of the echoes in 2019, the characteristics of the echoes are studied. It is observed that the echoes have a large day-to-day variability. Figure 5.2 depicts the signal to noise ratio (SNR), spectral width and Doppler velocity of 150-km radar echoes as observed using the EAR at Kototabang on two geomagnetic quiet days, 02 September 2018 and 07 September 2019. The echoes generally start getting visible in the forenoon hours. It descends with time to lower heights and again start ascending in the afternoon hours, that is, they possesses a necklace shape when seen in a range-time intensity plot.

It is observed that on 07 September 2019, the morning descending structure has a high SNR, compared to that in 02 September 2018. It also descends at a faster rate (6.5 km/ hour) and reaches to 140 km height. On 02 September 2018, the echo is weaker. However, for both the days, the spectral width is less, when SNR is larger. The Doppler velocities do not show a clear relationship with SNR, unlike the spectral width. It is negative during both the days, with much lesser value during 07 September 2019. Negative velocity indicates that the irregularities are moving away from the radar. Therefore, to segregate the echoes having different characteristics based on SNR and spectral width relation, the scatter plot of SNR and spectral width for three geomagnetic quiet days of September 2018 (Figures 5.3 a–c) and September 2019 (Figures 5.3 d–f) between 140 and 160 km altitude and 10–15 h local time are shown in Figure 5.3.

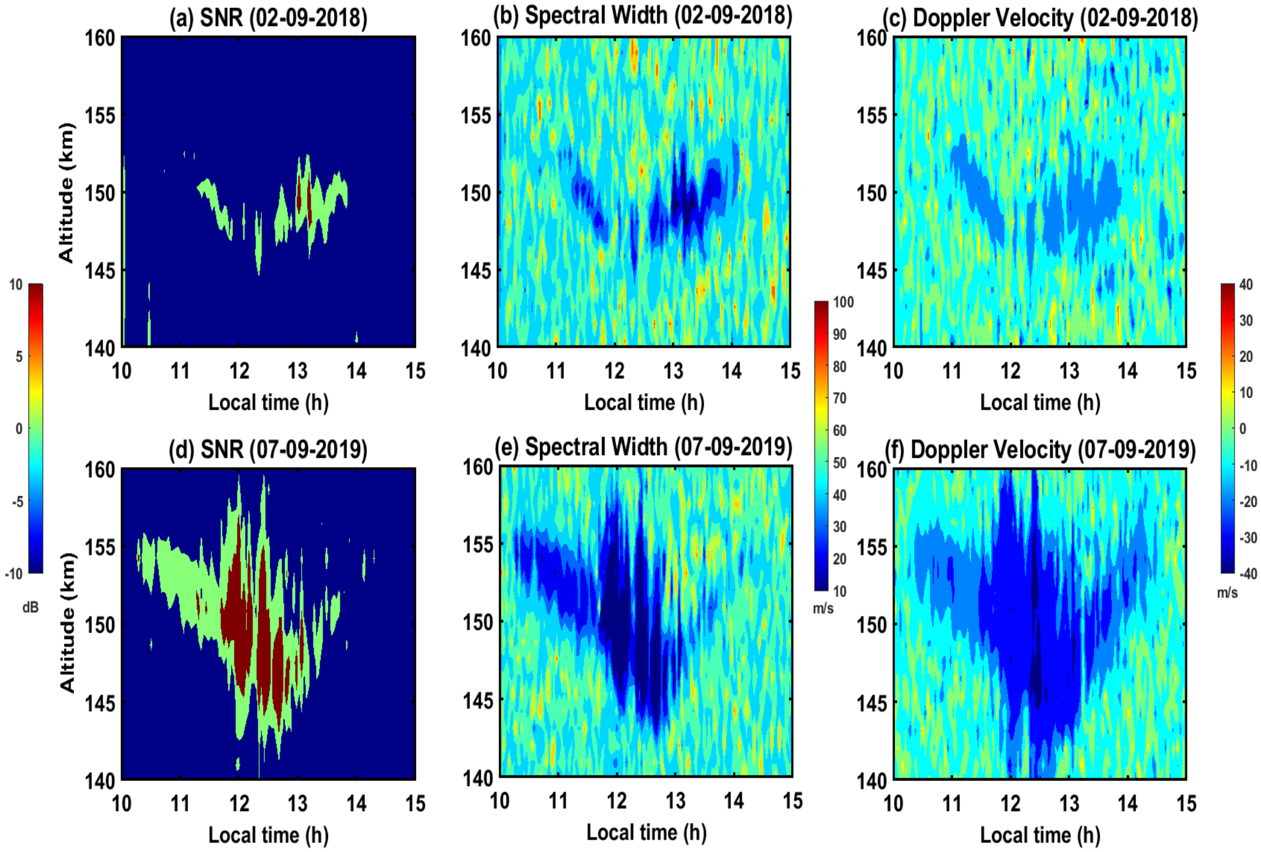

Figure 5.2: Equatorial Atmosphere Radar (EAR) observations of (a,d) SNR (dB), (b,e) Spectral width (m/s) and (c,f) Doppler velocity (m/s) of 150-km echoes on 02 September 2018 and 07 September 2019

It is observed that the echoes having SNR greater than 3 dB (blue dots) possess narrow spectral width (less than 10 m/s), while the echoes having SNR less than 3 dB (red dots) have large spectral spread (10–40 m/s).

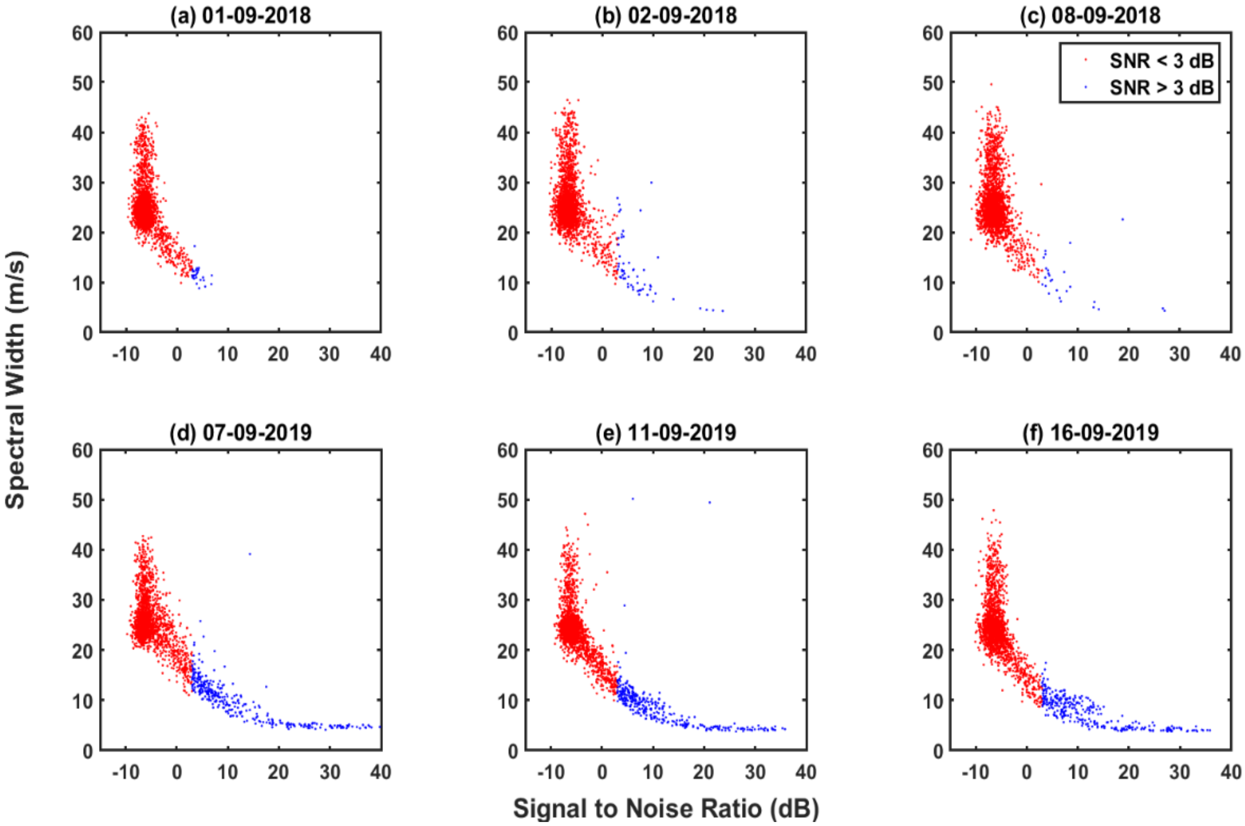

Figure 5.3: Scatter plots of SNR and spectral width for a few geomagnetically quiet days (a–c) 01 September 2018, 02 September 2018 and 08 September 2018 and (d–f) 07 September 2019, 11 September 2019 and 16 September 2019. The SNR less than 3 dB threshold is shown with red dots and greater than 3 dB is shown with blue dots

Therefore, by putting a threshold of 3 dB, the echoes are segregated and their occurrence rate and characteristics are studied further during the same three quiet days of September 2018 (Figure 5.4) and September 2019 (Figure 5.5).

Figure 5.4 depicts the altitude-time cross sections of SNR for some quiet days of September 2018, viz., 01 (Figures 5.4 a–c), 02 (Figures 5.4 d–f) and 08 September 2018 (Figures 5.4 g–i) and September 2019, viz., 07 (Figures 5.5 a–c), 11 (Figures 5.5 d–f) and 16 September 2019 (Figures 5.5 g–i).

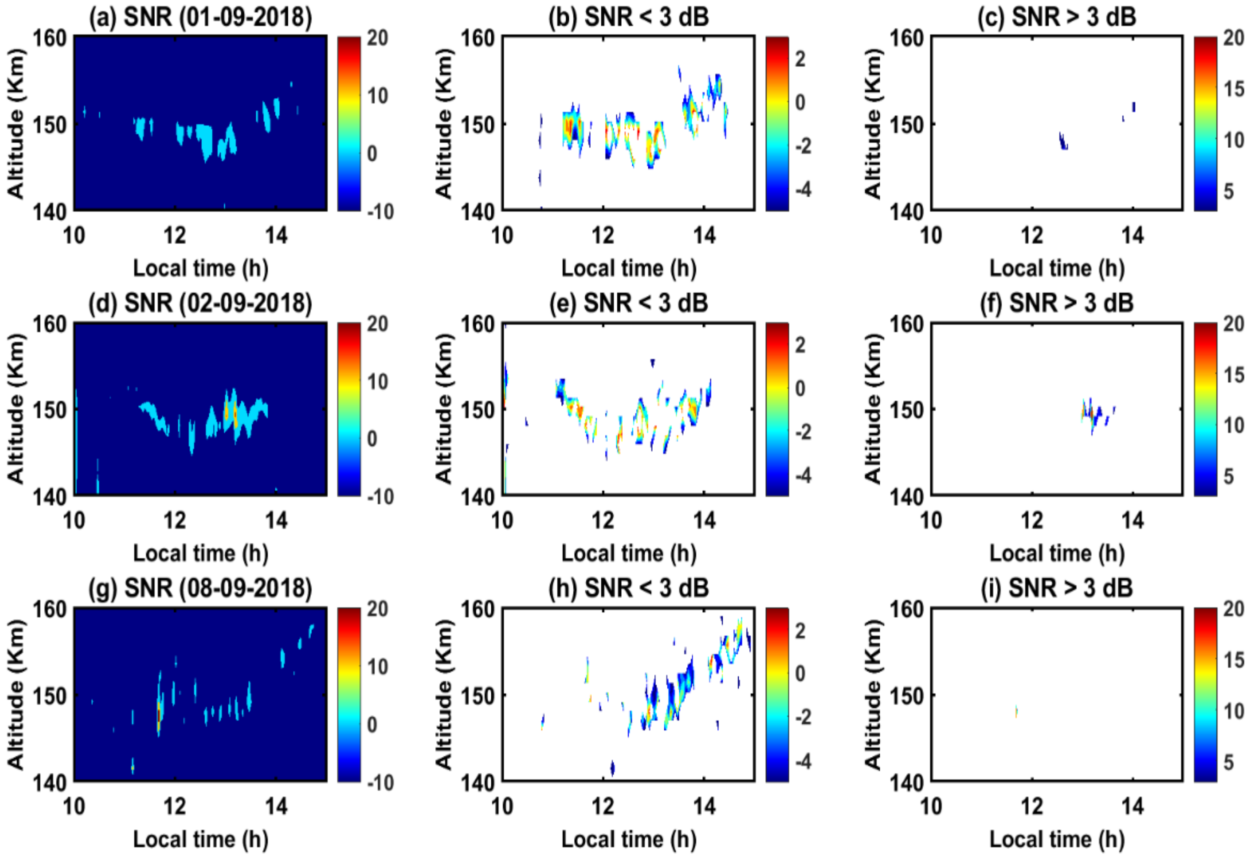

Figure 5.4: Altitude-time cross sections of SNR for a few geomagnetically quiet days (a-c) 01 September 2018, (d-f) 02 September 2018 and (g-i) 08 September 2018. The echoes with SNR less than 3 dB and greater than 3 dB are also shown in middle and right panels respectively

In September 2019, the SNR is larger and extended for both time and altitude compared to the echoes observed in September 2018. Also, the echoes possess a descending structure and they are present in all the quiet days of September 2019. However, except for 29 September 2018, the descending structured high SNR echoes are absent during all the quiet days of September 2018. It is suggested that this large SNR descending structured echoes might have caused the large occurrence of these echoes in 2019. To investigate the same, the PO and the monthly mean SNR (above 3 dB) during the quiet days of 2018 and 2019 are shown in Figure 5.6.

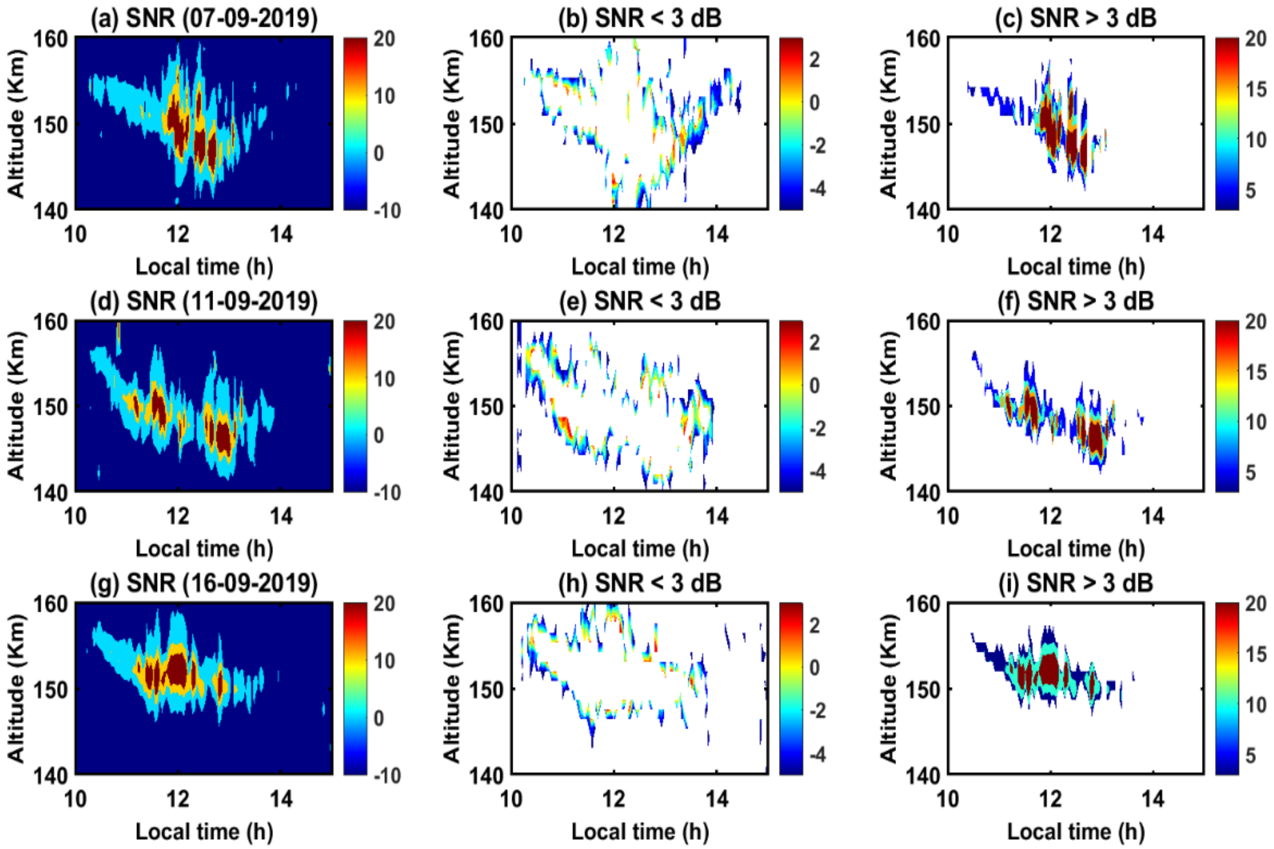

Figure 5.5: Same as Figure. 5.4, but for the quiet days (a-c) 07 September 2019, (d-f) 11 September 2019 and (g-i) 16 September 2019

Figure 5.6 a exhibits the maximum PO of descending echoes during June-August for the solar minimum years (2018–2019). For the month of September, the PO of these echoes is 3.44% for 2018 and 32% for 2019. The highest PO is observed during August 2019 (48.2%). Except for February–March the PO and the monthly mean SNR is larger in 2019 compared to 2018. For September 2018, the mean SNR is seen to be 12.14 dB whereas during September 2019, the mean SNR is found to be around 17.33 dB. Therefore, it is clearly seen from the Figures that the echoes occurring during September 2019 are proportional with more descending layer echoes having stronger SNR, compared to the ones observed during September 2018. It is suggested that the descending structured echoes might be associated with plasma instability developed on the intermediate/descending ion layers as suggested by Patra, (2011). Therefore, their large occurrence might have caused the large PO of these 150-km echoes in September 2019.

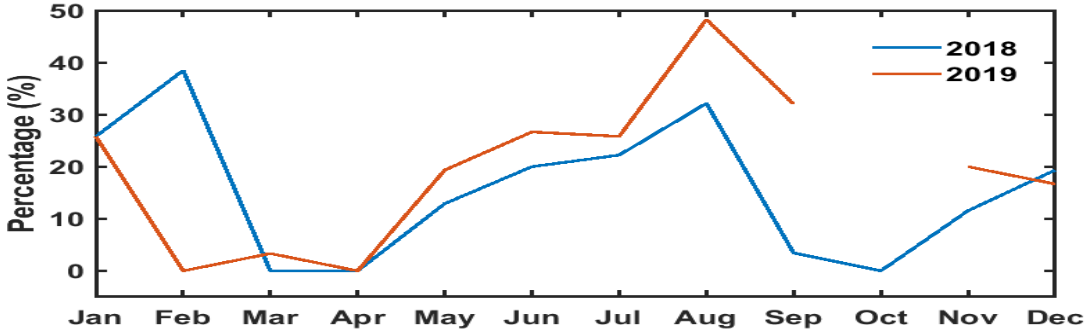
(a) Percentage of occurrence of descending echoing layers

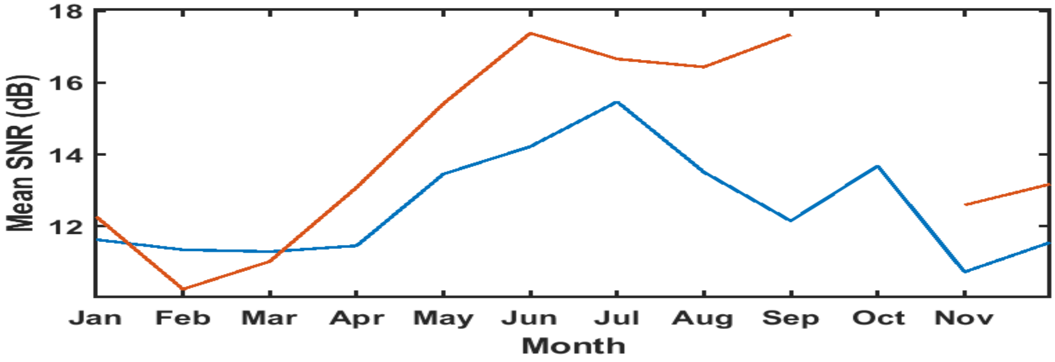
(b) Monthly mean SNR of 150-km echoes above 3 dB threshold

Figure 5.6: Monthly variation of percentage of occurrence (PO) of descending echoing layers and (b) the monthly mean of SNR (dB) of the 150-km echoes above 3 dB threshold present in geomagnetically quiet days of 2018 and 2019

In addition to September 2019, the descending structured high SNR echoes are observed during the boreal SSW of 2018 (December 2018 to January 2019) and also during June-August 2019. The range-time intensity plots of SNR for three quiet days 27 December 2018 (Figures 5.7 a-c) and 04 January 2019 (Figures 5.7 d-f) and 06 January 2019 (Figures 5.7 g-i) and the same for 10 June 2019 (Figures 5.8 a-c), 23 July 2019 (Figures 5.8 d-f) and 08 August 2019 (Figures 5.8 g-i), with a threshold SNR of 3 dB are shown in Figures 7 and 8 respectively.

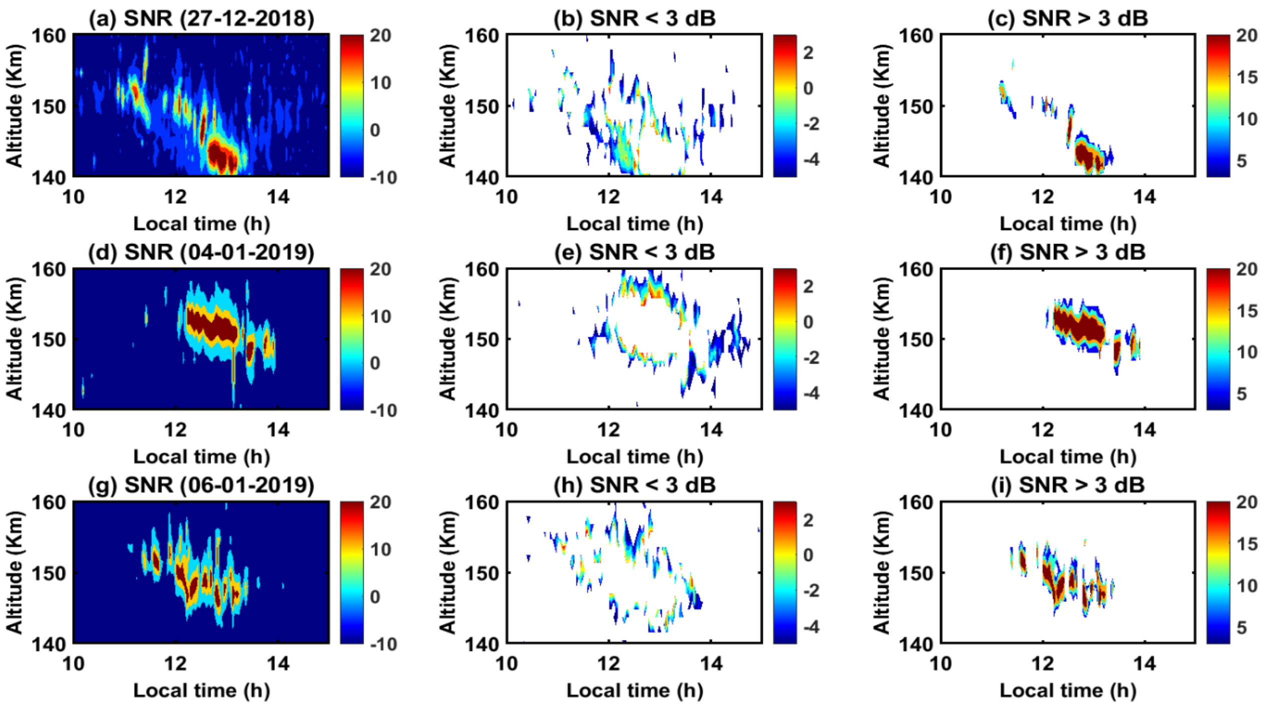

Figure 5.7: Same as Figure. 5.4, but for the quiet days (a-c) 27 December 2018, (d-f) 04 January 2019 and (g-i) 06 January 2019

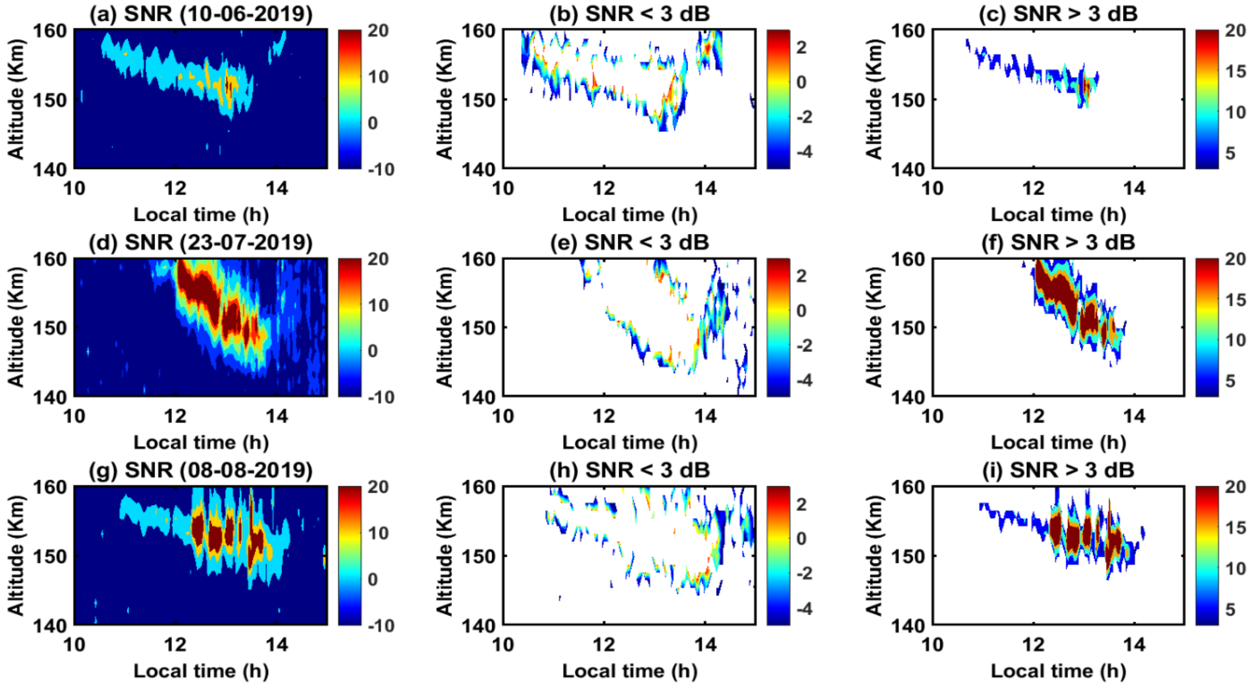

Figure 5.8: Same as Figure. 5.4, but for the quiet days (a-c) 10 June 2019, (d-f) 23 July 2019 and (g-i) 08 August 2019

The high occurrence rate of the echoes (June- August and boreal wintertime) is clearly seen to be associated with echoes having a large SNR that descends with height. The average descending rates of these echoes are calculated to be 6.3 km/hr on 27 December 2018, 6.68 km/hr on 04 January 2019 and 6.75 km/hr on 06 January 2019.

5.3.3. Ionosonde observations over Kototabang

To confirm the presence of intermediate ion layers during the echoing hours, associated with the descending structured echoes, the diurnal variation of virtual height of the bottom side F-layer (hpF or h’F) on the same three geomagnetically quiet days 07, 11 and 16 September 2019, obtained from the ionosonde observations over Kototabang, Indonesia are shown in Figure 5.9.

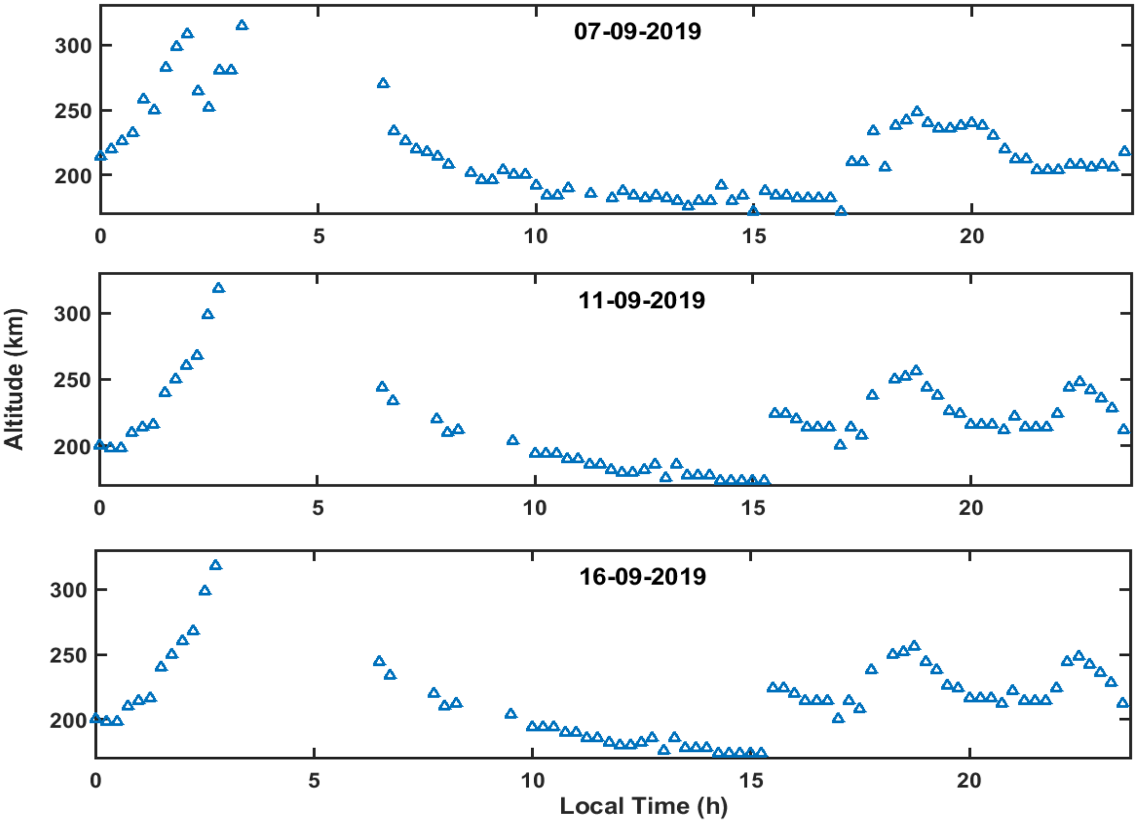

Figure 5.9: Diurnal variations of virtual height of the bottom side F-layer (hpF or h’F) over Kototabang for the geomagnetically quiet days 07 September 2019 (top panel), 11 September 2019 (middle panel) and 16 September 2019 (bottom panel)

The hpF shows a semidiurnal variation with highest values (around 300 km virtual height) during 2–3 h local time. It is followed by a period of low hpF values (below 200 km virtual height) during 10–15 h local time. It is observed that the descent rate of the layers during the echo formation (10–15 h local time) on 07 September is around 5.56 km/h, on 11 September is around 5.3 km/h and on 16 September is around 6.5 km/h, which are close to the mean descending rate of the echoing layers (7 km/h).

Figure 5.10 depicts the sample ionogram observations at the same location, confirming the presence of descending intermediate layers (frequency greater than 3 MHz). The intermediate ion layers are found to be descending to lower heights in the 150 km region during the echoing hours. On 08 September 2019, the density layer was descending from 160 km height and the ion layer was visible for nearly 4 h. For 11 and 12 September 2019, the layers were clearly visible continuously for 2 h and were found to descend from 150 km and 156 km heights respectively. As the rate of descent of both the intermediate ion layers and descending echoing layers are somewhat close to downward phase progression of the semi-diurnal tidal wind, that is ~7km/h **(**Harper, 1977), therefore the possible connection of the semi-diurnal tidal winds with the descending echoing phenomenon can be established.

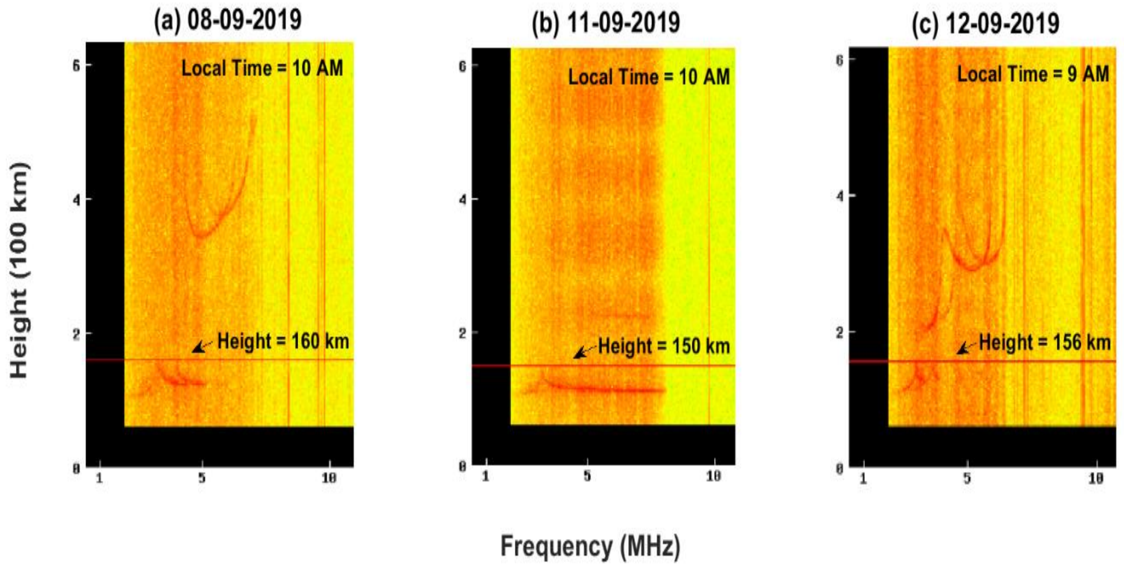

Figure 5.10: Sample ionogram observations over Kototabang on 3 geomagnetically quiet days (a) 08 September 2019, (b) 11 September 2019 and (c) 12 September 2019

5.3.4. Latitudinal variations of migrating and non-migrating tides in TIMED-SABER temperature

As the tidal winds are generated by the meridional wind shear associated with intermediate ion layers, the TIMED-SABER temperature data are subjected to space-time Fourier analysis and the tidal harmonics (with zonal wave-numbers from -4 to 4) are extracted. The latitude time variations of DW1, SW2 and DE3 tidal amplitudes from 60º N to 60º S in TIMED-SABER temperature at 98 km for the years 2016–2019 are shown in Figure 5.11.

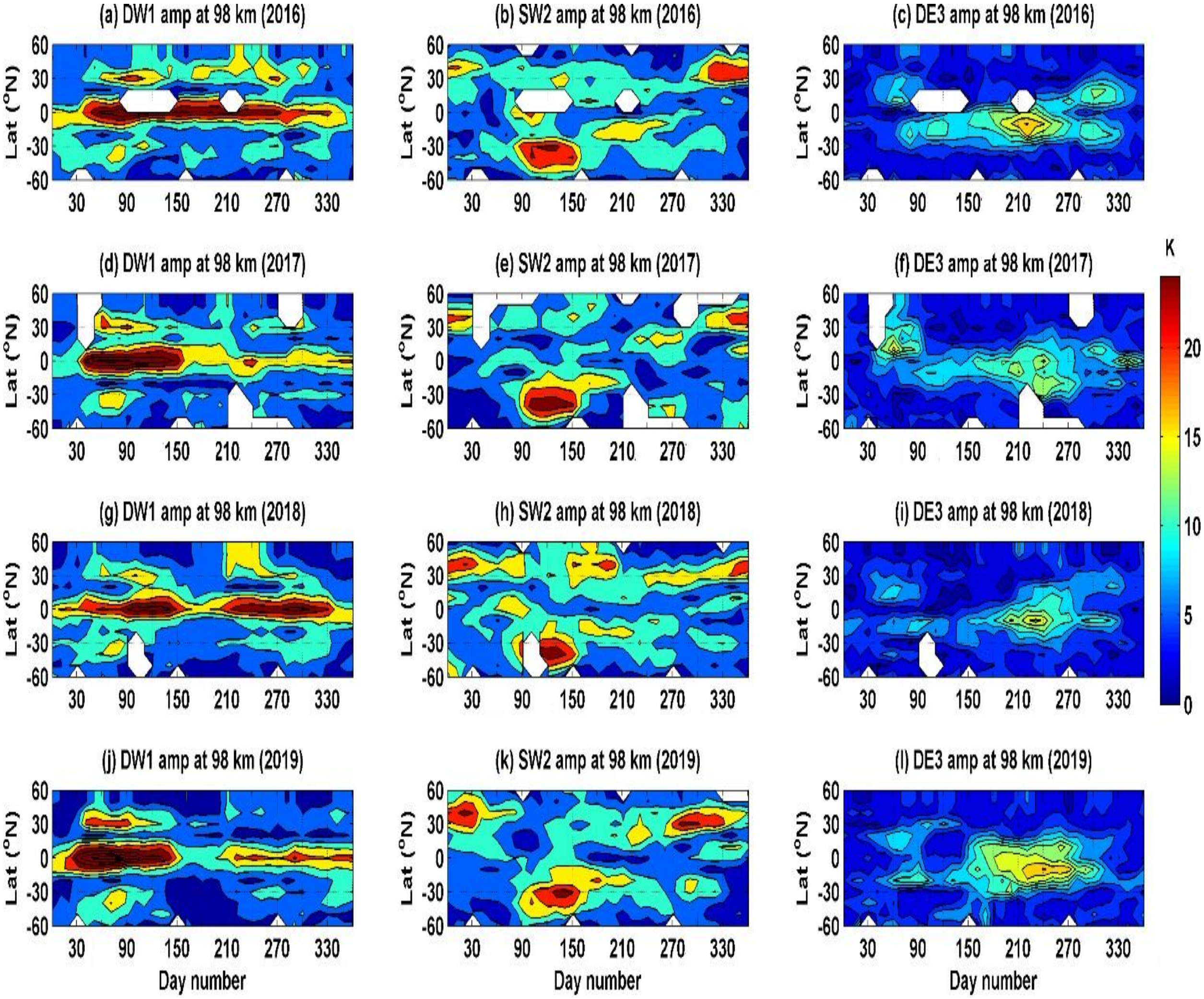

Figure 5.11: Latitude variations of DW1, SW2 and DE3 tidal amplitudes in TIMED-SABER temperature at 98 km for the years 2016–2019

The migrating diurnal tide DW1 shows maximum amplitudes over equator and it varies semi-annually with large amplitudes during equinox months, that is, end of February–May and

September–October (~41–150 and 230–300). During 2016 and 2018, DW1 show comparable amplitudes during equinox, however for 2017 and 2019 the tidal amplitudes during March equinox are much larger than it is during September. Besides, it shows an additional enhancement both over 30° N and 30° S latitudes, particularly during March equinox. Unlike DW1 tide, SW2 tide shows large amplitudes during February–May centered around 30° S–40° S and further extends to August with a peak value at 20° S. In October–February, it is centered around 40° N. Another maximum is observed at northern mid-latitudes during June-July particularly in 2018. The DE3 tide shows very large amplitudes during July-October centered around the equator, particularly during 2019.

5.3.5. Stratospheric ozone variability at different pressure levels

Since the SW2 tide is largely generated by the solar insolation absorption by stratospheric ozone, its variations at latitudes 10° N, Equator and 10° S for different pressure levels (10–1 hPa) are shown in Figure 5.12.

The ozone vmr at 1 hPa shows a semiannual variation with maxima during solstices (5–5.5 ppmv). During the June solstice of 2017 and 2019, the values are slightly larger compared to 2016 and 2018, indicating a quasi-biennial variation of ozone. At 2 hPa, the ozone vmr reaches a maximum of 8 ppmv in January 2019 over the equator, when a major boreal SSW event occurred. The maxima during June–July are nearly comparable in all four years (around 7 ppmv). At 3 hPa, the value of ozone vmr follows the same variation as at 2 hPa with a relatively larger value. The maximum during January is shifted towards equinox months and the secondary peak of June–July is shifted towards September month at 5 hPa and 10 hPa. At 10 hPa, large ozone vmr is observed for the years 2017 and 2019, compared to 2016 and 2018, again indicating a quasi-biennial variability in ozone. The highest ozone vmr is observed during the first week of October 2019, with peak values of 11.3 ppmv at 10° N, 12 ppmv at the equator and 11.7 ppmv at 10° S.

Next, the daily ozone vmr anomaly is checked anomaly at 1 hPa (top panels) and 10 hPa (bottom panels) over 10°N, equator and 10°S for the years 2016-2019 and is shown in Figure 5.13. To obtain the anomaly, the composite daily mean for the years 2007–2019 is obtained and it is subtracted from the daily ozone vmr of each year.

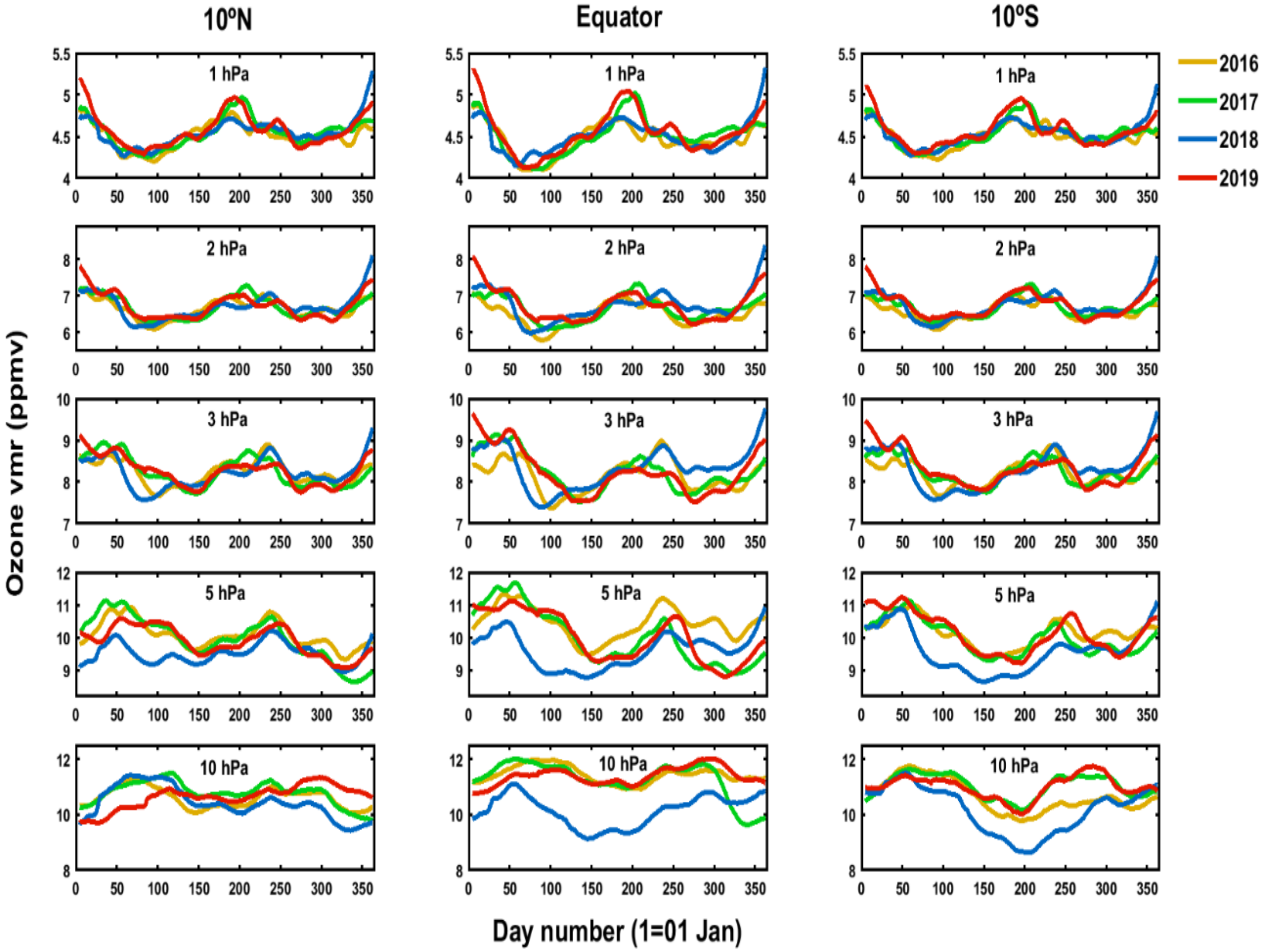

Figure 5.12: Time-height cross-section of the daily averaged zonal mean TIMED-SABER ozone volume mixing ratio (vmr) at 10ºN (left panels), equator (middle panels) and 10ºS (right panels) at different pressure levels from 10 hPa to 1 hPa for the years 2016–2019

From the figure it is observed that the ozone anomaly in the years 2017 and 2019 is largely positive compared to other years. At 1 hPa, ozone anomaly is larger at the beginning of the year (0.46 ppmv at the equator for 2019) and also during July for both 2017 (0.24 ppmv) and 2019 (0.3 ppmv). However, ozone shows a sharper negative anomaly in the month of July for the years 2016 (-0.32 ppmv) and 2018 (-0.19 ppmv), with the lowest at the equator. At 10 hPa, positive anomaly is observed almost throughout the years 2017 and 2019 at 10º S, with a peak anomaly of 1.26 ppmv in September 2019.

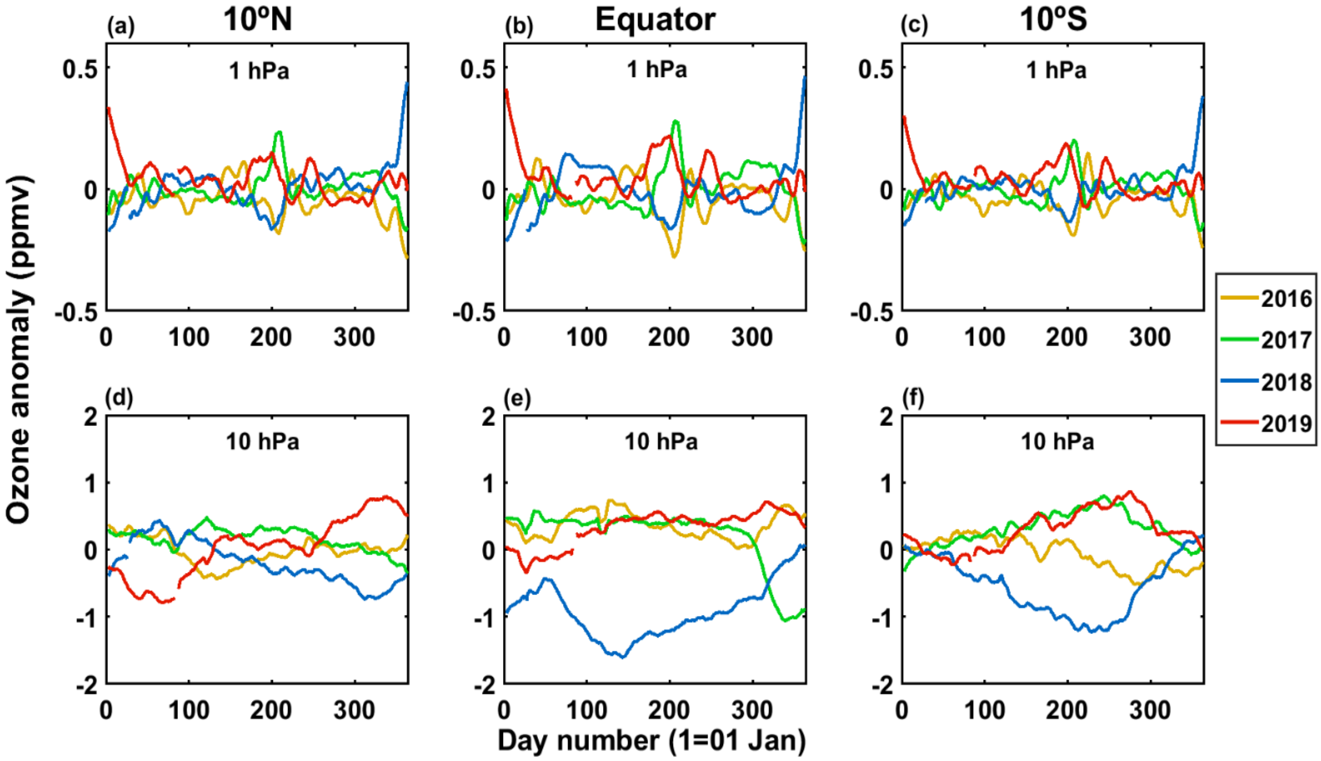

Figure 5.13: Daily averaged zonal mean TIMED-SABER ozone volume mixing ratio (vmr) anomalies at 10ºN, equator and 10ºS, at 1 hPa (top panels) and 10 hPa (bottom panels), for the years 2016–2019

5.3.6. State of northern and southern hemispheric polar stratosphere during 2016–2019

Sridharan et al. (2012) observed an increase of ozone vmr in the equatorial stratosphere which caused the increase in the mesospheric semi-diurnal tidal amplitude and the suppression of diurnal tidal amplitude during the boreal SSWs of 2006 and 2009. Goncharenko et al. (2012) also noted the increase of equatorial ozone mixing ratio at 2 hPa during the tropical stratospheric cooling in response to the major SSW of 2009. Therefore for the identification of status of the polar stratosphere in connection to the SSW, the daily variations of the zonal mean of the temperature (NCEP) difference between 90º and 60º latitudes, zonal mean winds (NCEP) at 60º latitudes and planetary waves of zonal wavenumber 1 at 60º latitudes in the mid-stratosphere (10 hPa) are investigated **(Figure 5.14)**.

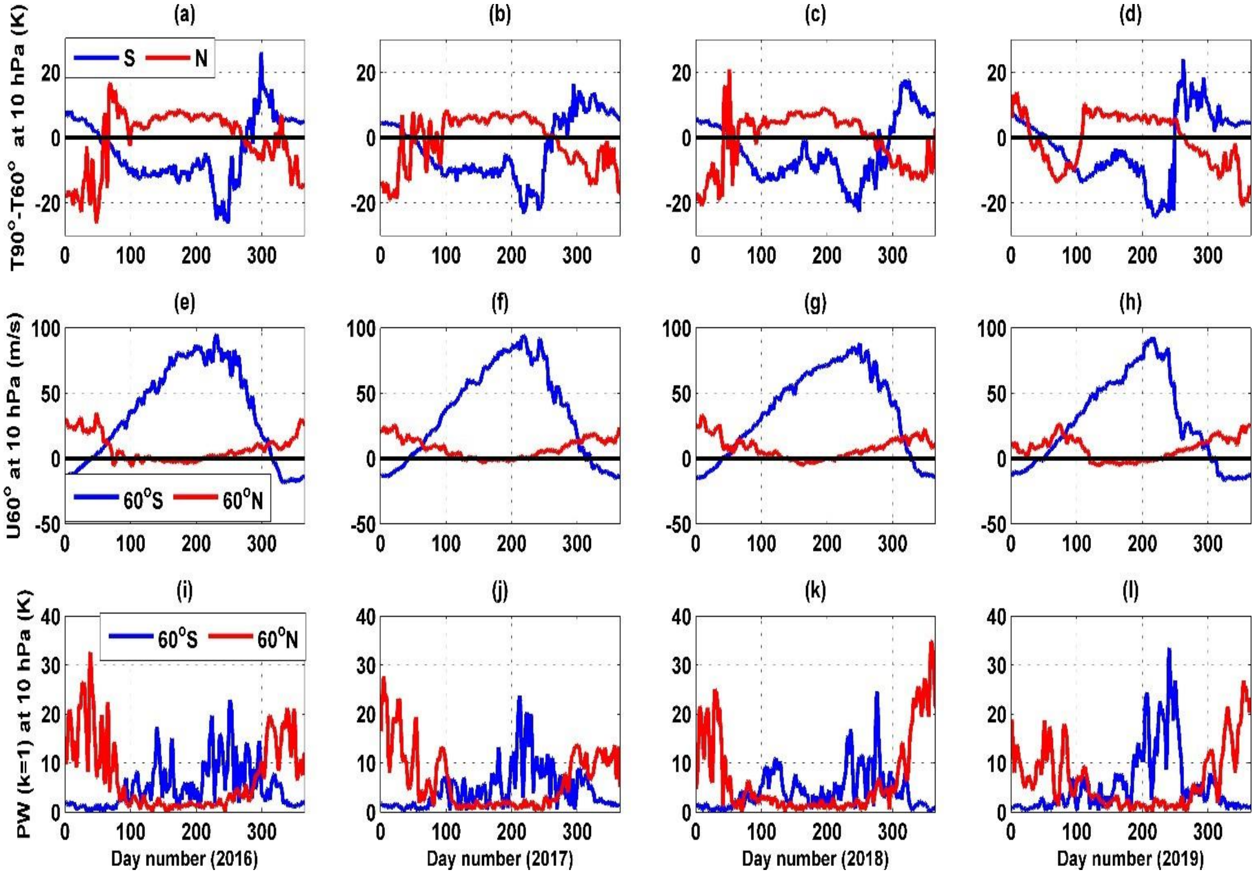

Figure 5. 14: (a-d) Daily variation of the temperature difference (DT) between the latitudes 90° and 60° in the respective northern (N) and southern (S) hemispheres, (e-h) zonal mean zonal wind (U) at 60° latitudes in the respective hemispheres and (i-l) amplitude of the planetary waves of zonal wavenumbers 1 at 10 hPa and 60° latitude in the respective hemispheres for the years 2016–2019

The criteria of zonal wind reversal (from westerly to easterly) during SSW can be relaxed for the southern hemisphere with just a reduction of eastward winds (westerly) to less than 20 m/s as the vortex is stronger over there. The ΔT is normally positive in the boreal polar region during March–September (~59-269) and in the austral polar region during October-February (277-365 and 1-53). It is negative for the rest of the times. The onset of SSW is indicated by the change of negative ΔT to positive during winter-early spring in the respective hemispheres. In the year 2016, the boreal ΔT is positive during day numbers 327– 332 (Figure 5.14 a) followed by only the deceleration of the zonal mean zonal wind (Figure 5.14 e). For 2017, there are three successive SSW events with positive ΔT during day numbers 32–35, 48–51, 54–66 (Figure 5.14 b), with just a decrease in the magnitude of the eastward winds (Figure. 5.14 f). For 2018, the ΔT is positive during day numbers 42–48, 50–54 and 364–365 (Figure 5.14 c) and for 2019, the positive ΔT continues to persist till the day number 29 (Figure 5.14 d). Though there is positive ΔT around day number 255 in 2017 and 280 in 2018, the eastward wind is not reduced to less than 20 m/s (Figures 5.14 f–g). The planetary wave (PW) of wavenumber 1 (PW k=1) is observed to enhance prior to the boreal and austral SSW events. The PW of k = 1 at 60º N increases to above 30 K prior to the 2019 January SSW event, followed by its drastic decrease with the SSW onset (Figure 5.14 k). Similarly, the PW of k = 1 at 60º S is increased to above 30 K prior to the 2019 September austral SSW (Figure 5.14 l). This large enhancement of the PW of k = 1 is not observed for other years during September, indicating the role of PW in causing the SSW events.

5.4. Discussion

The EAR observations over Kototabang show the maximum PO of the type-B 150 km radar echoes during boreal summer (June–August) and boreal winter (December–January) months, with large interannual variability. The seasonal variation of 150 km echoes over Pohnpei and Gadanki also showed a distinct summer maxima of the echoes (Tsunoda and Ecklund, (2004), Patra et al. (2017)). However, the echoes over Jicamarca do not exhibit a clear seasonal variation (Chau and Kudeki, (2006)). From 2016 to 2019, that is from solar moderate to solar minimum years, the PO of these echo are found to increase. Their occurrence is larger throughout the year 2019, particularly during September 2019, when a minor but impactful austral SSW event occurred. It is observed that during September 2019, high SNR descending structured echoes are present. The high SNR echoes are also found to be present during December 2018–Janauary 2019, which again includes a major boreal SSW event. The echoes having high SNR (> 3 dB) have low spectral width and vice versa. The presence of intermediate ion layers during the echoing hours has been observed using sample ionosonde observations. Observations suggest that the intermediate ion layers are mostly composed of molecular ions like NO^+ and O_2^+ and the metallic ions like Fe^+ and Mg^+ (Gardner et al., (1995), Heelis, (1999)). The metallic ions in the intermediate layers are believed to be lifted by the vertical motion from the E region through equatorial E x B plasma drift (Hanson et al. (1972)). Because of their smaller recombination rate than those of the molecular ions, they would give rise to the layer formation. The average slope of the virtual height of the bottom side of F layer (hpF) during the echoing hours is found to be around 5.8 km/h and the average descent rates of these echoing layers are estimated to be around 7 km/h. Since the descent rates of the 150-km radar echoes and the hpF is very much similar to the rate of downward phase progression of semi-diurnal tidal wind (Harper, (1977)), the possible role of the semi-diurnal tidal winds in the echoing phenomenon is suggested. Previous studies reported that the confluence of tides (either the combination of 24-h and 12-h tides or the addition of 6-h tidal component) can cause ‘quasi-stagnation’ or a rapid upward-downward motion of a layer (Morton et al. (1993)). Recently, Krall et al. (2020) also showed that tides could form an ion layer by the wind shear associated with them, which may result in the instability of ion density gradients and plasma irregularities.

In this chapter, it is seen that the semi-diurnal tide at 98 km shows larger amplitudes during June–August months when large PO of these echoes are observed. Though SW2 tidal amplitude shows comparative amplitudes in both September 2018 and September 2019, the DW1 tide is relatively smaller in the second half of the year 2019, when the maximum PO of these echoes were observed. Therefore, for investigating the relationship between the migrating (SW2 and DW1) tides and the PO of the echoes, correlation analysis is employed. In both 2018 and 2019, the correlation coefficient between DW1 tide and the echo occurrence are statistically significant with values -0.7 and -0.79 with p values 0.01 and 0.02 respectively. The p value denotes the probability of getting a correlation as large as the observed value by random chance and the value should be less than 0.05 for a significant correlation. With SW2, the correlation coefficients are 0.46 and 0.36 ($p = 0.1$ and 0.25) for the years 2019 and 2018 respectively. Besides the correlation value are found to be non-significant. The correlation analysis suggests the relative suppression of DW1 tide ($R=-0.7$ and -0.79) is more important in connection to the high occurrence of these echoes during September 2019. It is suggested that the suppression of DW1 tide leads to the relative enhancement in the SW2 tide.

Lindzen, (1972) showed that zonal mean zonal winds and temperature gradients can influence the tidal propagation to mesospheric heights. Moreover, the mesospheric tidal variabilities are governed by tidal forcing, tidal dissipation, tidal-wave interactions and tidal-mean flow interactions. The reduction in the DW1 tide in 2019 may be due to its interaction with planetary waves, which are normally enhanced just before the onset of the SSW event. It is also possible that the DW1 tide may have interacted with the PW of k = 1 to generate DS0 tide **(**Truskowski et al., 2014). The DW1 tide is principally generated from the IR radiation absorption by water vapour in the troposphere, and also due to UV absorption by ozone in the stratosphere. However, they have opposite phases to each other as per the global scale wave model (GSWM) simulations by Hagan, (1996). As larger stratospheric ozone vmr values are observed in 2017 and 2019, it is suggested that the UV absorption by ozone suppresses the IR radiation absorption by tropospheric water vapour, leading to a minimum amplitude of the DW1 tide in 2017 and 2019. This also induces quasi-biennial variability of the DW1 tide in the September equinox and leads to the relative enhancement of SW2 tide in those years.

The semi-diurnal tidal variability at mesospheric heights is largely controlled by the variation of ozone at stratospheric heights. The results from the present chapter show that stratospheric ozone vmr at 10 hPa is the largest (12ppmv) in the year 2019, particularly it is about 10.7 ppmv at 5.62 hPa during September 2019. This explains why semi-diurnal tidal amplitude is slightly larger in 2019 than in 2018. Moreover, because of its larger vertical wavelength, along with the solar minimum conditions of 2019, it can reach the thermosphere without much attenuation (Truskowski et al. (2014)) and can cause semi-diurnal variation in the electric field through the dynamo mechanism. Earlier, Sridharan et al. (2009) noted an enhancement of semi-diurnal tidal amplitude and a reduction in diurnal tidal amplitude from the MF radar wind observations over the magnetically equatorial station, Tirunelveli (8.7ºN, 77.8ºE) during major SSW events. They further demonstrated that the enhancement of the semi-diurnal tidal amplitudes could be due to the accumulation of stratospheric ozone over the equatorial latitudes during the SSW events (Sridharan et al. (2012)). This enhancement is mostly due to the migrating semi-diurnal tide (SW2) and the contribution from the non-migrating semi-diurnal tide is relatively less (Sridharan, (2017)). Therefore, the results in this chapter suggest that the enhancement of equatorial ozone molecules might be related to the austral SSW of 2019. Pedatella et al. (2014) have also shown the enhancement in the solar (SW2) and lunar (M2) tides during SSW 2009 using modeling results (WACCM-X and TIME-GCM).

Although the stratospheric ozone is higher both in 2017 and 2019, the larger PO of 150-km echoes in the year 2019 than in the year 2017 may be due to the fact that the former is a solar minimum year and later is a solar moderate year. The solar minimum conditions might have provided the necessary condition to the SW2 tide for reaching heights above 120 km with relatively less attenuation of its amplitude. However, further investigations are required for its confirmation.

The role of solar radiation in the occurrence of 150-km echoes are confirmed from their strict solar cycle dependence, their presence up to lower heights during solar flare events (Pedatella et al. (2019)), their absence during solar eclipse time **(**Patra et al. (2011)) and their altitude of occurrence, where the formation of photoelectrons maximizes. Recently, Oppenheim and Dimant, (2016) have provided a physical explanation of their source based on high-frequency waves generated by a photoelectron bump-on-tail microinstability, where the electron velocity distribution function is multiple peaked. In an unmagnetized plasma, the shell will not generate instability. If the magnetic field is present in the plasma, it can drive high-frequency electron modes. These wave modes will non-linearly decay into ion waves, which the radars can detect. Longley et al. (2020) suggested that the echoes could be due to photoelectron driven upper hybrid instability. However, it could not explain why the predicted instabilities are at all altitudes; while the observations are limited to around 150-km and why the small-scale features are present. Patra and Chaitanya, (2014) observed that the descending layer type echoes having high SNR are different from the necklace pattern echoes and they resembled the nighttime valley region echoes related to intermediate layer formed by the meridional wind shear associated with the semidiurnal/terdiurnal tidal winds. The former echoes are likely to be driven by semi-diurnal tidal wind shear initiated instability, whereas the latter may be caused by the upper hybrid instability. The former does not appear independently of the latter, while the latter occurs independently of the former (Patra et al. (2017)). Results in this chapter are also consistent with the previous results and the high occurrence of the echoes during September 2019 can be attributed to the high occurrence of descending structured echoes, which is formed by interchange instability on the intermediate ion layer caused by meridional wind shear of semi-diurnal tidal winds, along with solar minimum conditions.

The DE3 tide, which is a diurnal Kelvin wave, is generated due to latent heat release during deep tropical convection and its strong zonal component is similar to a Kelvin wave. Since it has a larger vertical wavelength, it can penetrate deep into the ionosphere (Truskowski et al., 2014). However, its weak meridional component suggests that it can unlikely cause the large meridional wind shear required for the interchange instability related to the formation of the 150-km radar echoes.

Chapter 6: Signature of SSWs in the UMLT region, both on the pole and its antipode

6.1. Introduction

SSW is a wave-driven large-scale middle atmospheric phenomenon, characterized by the rapid amplification of polar stratospheric temperature by several tens of degrees within a short period. The SSW-induced effects extend well beyond polar stratosphere and their impacts is well detected from oceans to the ionosphere (Goncharenko et al. (2010), Liu et al. (2019), Zhang et al. (2022)). Some studies have shown that even as a predictor of several tropospheric weather events, stratospheric harbingers may be used (Julian et al. (1965), Quiroz, (1977)). Effects in the middle atmosphere include elevated stratopause events, enhanced downward transport of trace species from mesosphere, which leads to the increment of NO_x and CO over stratosphere (Siskind et al. (2015)). In the UMLT region, just before the SSW onset (more specifically stratospheric zonal mean wind reversal), Hoffmann et al. (2007) observed high-latitude mesospheric cooling and reversal of mesospheric circulation (eastward to westward winds), which indicate a downward propagation of the circulation disruption from the UMLT region to the stratosphere during major SSW events. The downward propagation of disturbances even to troposphere leads to anomalous cold outbreaks over northern Europe, Asia and in eastern US, associated with a negative phase of Northern Annular Mode (NAM) and North Atlantic Oscillation (Kolstad et al. (2010), Lehtonen and Karpechko, (2016)). However, more pronounced effects of SSWs have been observed for the boreal SSWs, compared to the austral ones as it is less frequent (Hoffmann et al. (2002), Manson et al. (2006), Dowdy et al. (2004)). Using Resolute Bay (75° N, 95° W) Michelson interferometer, Bhattacharya et al. (2004) reported decrease of the semi-diurnal tidal amplitude following the UMLT wind reversal and increased activity of some waves (8hr periodicity) before the peak of the stratospheric temperature. At the time of SSW onset, UMLT gravity wave zonal momentum forcing has also been found to switch from westward to eastward and its reversal is observed during the formation of the elevated stratopause.

Several studies have discussed the global enhancement of waves in connection to the SSW events. An enhancement of semidiurnal lunar tide was noticed at low latitude using a global-scale wave model (GSWM) and meteor radar observations (Stening et al. (1997), Paulino et al. (2012)). Over low latitudes, Sridharan et al. (2009) observed an enhancement of semi-diurnal tidal amplitude and suppression of diurnal tide during the major SSW events as discussed in chapter 5. The enhancement of semidiurnal tide, mostly from SW2 tidal component, was attributed to the increased concentration of ozone over equatorial stratosphere (Sridharan et al. (2012), Goncharenko et al. (2012), Sridharan, (2017)). Jin et al. (2012) observed the increase in TW3 tidal amplitude in the UMLT region from low to mid latitudes during SSW event of 2009.

Interestingly, the effects of Arctic SSWs are observed more in the low and mid latitudes of Southern Hemisphere compared to the high and mid latitudes of Northern Hemisphere (Fagundes et al. (2015), Goncharenko et al. (2022)). Several studies have discussed the modification of the low latitude F region ionosphere during SSWs due to semi-diurnal perturbations in vertical plasma drift velocities, electron density, total electron content and equatorial electrojet (Goncharenko et al. (2010), Chau et al. (2009), Lin et al. (2013), Yamazaki et al. (2012)). Changes in the Southern mid latitude ionosphere has been attributed to the thermospheric wind modulation by semi-diurnal lunar tide. Goncharenko et al. (2022) provided observational evidence for the interhemispheric coupling associated with boreal SSW of 2013 that affected the high latitude mesosphere and ionosphere of the Southern Hemisphere. However, the effects of SSW on the opposite polar UMLT dynamics have been least explored, particularly during the austral SSW. Therefore, motivated by the links between SSW events and the wave-tidal amplitudes changes from low to high latitudes, we aim to look into the impacts of boreal (austral) SSW in the Southern (Northern) polar UMLT region during 2013 and 2019.

6.2. Data used

In this chapter, we have utilized UMLT wind data obtained from meteor radar over Esrange and Rothera, NCEP/NCAR reanalysis products of polar stratospheric temperature and zonal winds, and MLS-Aura satellite dataset for calculating ozone concentration and SD-WACCM model outputs of polar stratospheric winds, temperature and ozone vmr values. The solar and lunar tidal and PW activity is calculated from the meteor radar wind data. The 6-hourly WACCM free run output to calculate the daily temperature at 10 hPa for 90° and 60° latitudes, zonal winds at 10 hPa over 60° latitudes and ozone vmr between 100-1 hPa over 67.5° latitudes. The outputs are compared with satellite and reanalysis products for the SSW event of 2019. The reason behind choosing the 2013 and 2019 events is the simultaneous meteor radar wind data availability over the two sites. The details of the data and methodology are provided in chapter 2.

6.3. Results

6.3.1. Stratospheric temperature, zonal wind and PW during boreal SSW of 2013

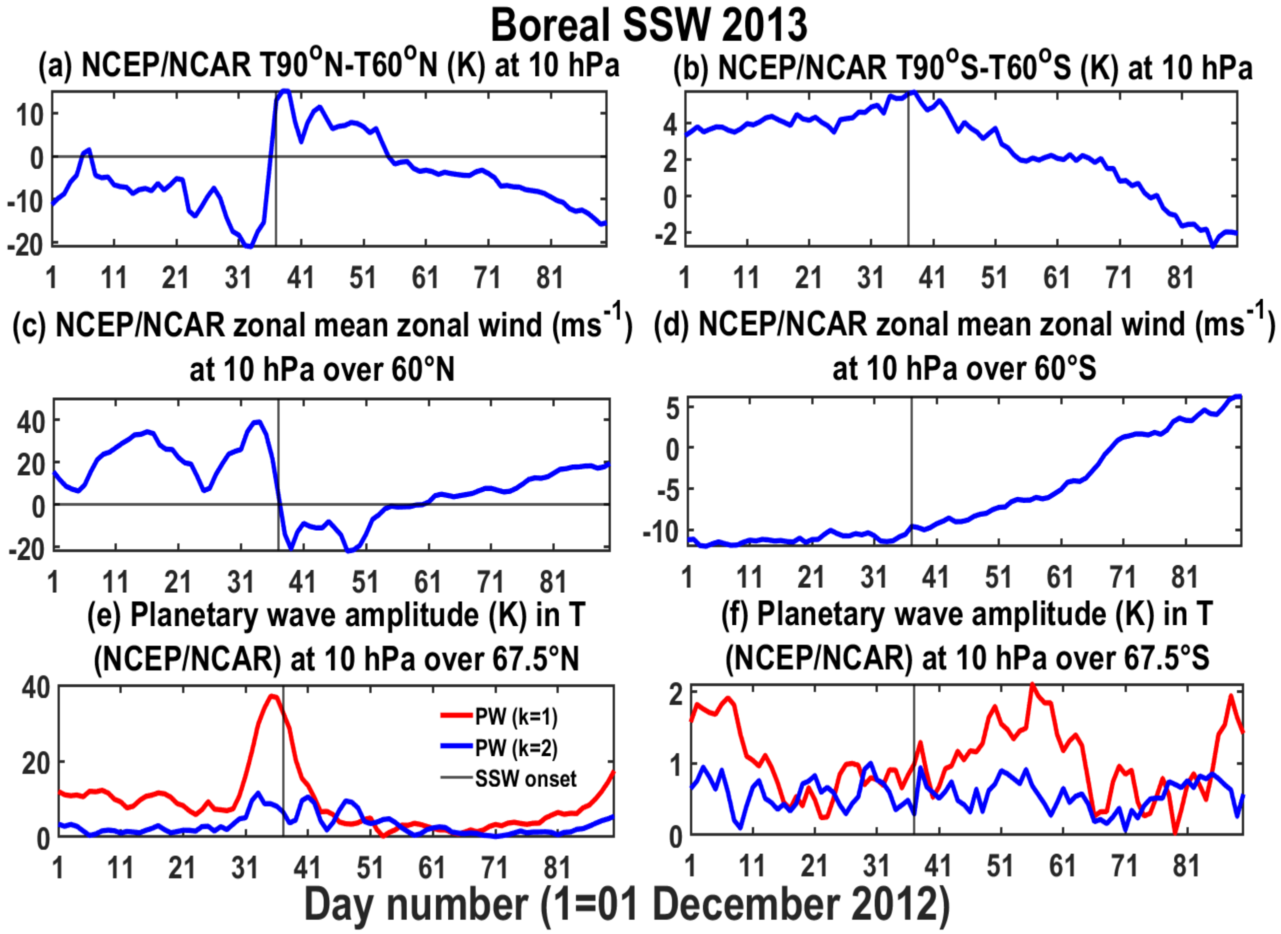

Figure 6.1: (a,b) NCEP/NCAR temperature difference between 90⁰ and 60⁰ latitude at 10 hPa, (b,d) zonal mean zonal wind at 60⁰N and 60⁰S and 10 hPa, (e,f) planetary wave amplitude in temperature at 67.5⁰N and 67.5⁰S and 10 hPa for the days 1-90 starting from 01 December 2012. The vertical black line represents the SSW onset day

To start with, Figure 6.1 depicts the temperature, zonal wind and PW amplitude in temperature obtained from NCEP/NCAR reanalysis products in the same (northern) and opposite (southern) hemispheres associated with the boreal SSW event of 2013. To identify the SSW onset day, the period 01 December 2012 to 28 February 2013 is considered. It is observed that the temperature difference between 90º N and 60º N at 10 hPa (Figure 6.1 a) becomes positive (13 K using NCEP/NCAR) on day number 37 (06 January 2013). Therefore, 06 January 2013 is considered as the 2013 boreal SSW onset day (shown by vertical black lines in the Figure). In the opposite (southern) hemisphere, no significant changes in temperature gradient is observed except for its gradual decrease, which is mostly related to the seasonal variation (Figure 6.1 b).

For identifying whether it is major or minor SSW, the zonal mean zonal wind variation during the SSW time at 60º latitude at 10 hPa is investigated (Figure 6.1 c). It is observed that the zonal mean zonal wind over 60º N changes from westerly (4 m/s) on day number 37 (06 January 2013) to easterly (-14 m/s) on day number 38 (07 January 2013), which indicates that the boreal SSW of 2013 is a major warming event according to the definition provided by WMO. In the opposite (southern) hemisphere (Figure 6.1 d), it is observed that the easterlies gradually become westerlies a few days after the boreal SSW onset (day number 70 or 08 February 2013).

The changes in the PW amplitude in temperature at 10 hPa (Figure 6.1 e) reveal maximum amplitude (37 K) of PW (k=1), just before the SSW onset (day number 35). Whereas the PW (k=2) shows a peak of 11 K on day number 33 (02 Jan 2013). However, the amplitude of PW (k=1) drastically decreases after the onset day, while that of PW (k=2) amplitude shows enhancements on day number 41 and 47 (10 and 16 Jan 2013 respectively). In the opposite polar stratosphere (Figure 6.1 f), PW (k=1) is observed to enhance (~2 K) a few days before (day number 7 or 07 December 2012) after (day number 56 or 25 January 2013) the boreal SSW onset day.

6.3.2. Stratospheric temperature, zonal wind and PW during austral SSW of 2019

The variation of temperature, zonal wind and PW amplitude in temperature from 01 August 2019 to 31 October 2019, associated with the austral SSW of 2019 is shown in Figure 6.2. Here, results obtained from the NCEP/NCAR reanalysis product are compared with the SD-WACCM model outputs. The latitudinal temperature difference between 90º S and 60º S, which determines the SSW onset day, becomes positive, that is, 0.4 K on day number 37 (06 September 2019) and 15 K day number 38 (07 September 2019) as per the NCEP/NCAR reanalysis and WACCM model outputs. Although, the WACCM and NCEP/NCAR products show one-day difference regarding the onset of the austral SSW, the date 06 September 2019 (day number 37) is considered as the onset day for the austral SSW, based on NCEP/NCAR reanalysis product as done in Figure 6.1. For the opposite (northern) hemisphere, the temperature difference (Figure 6.2b) shows negative value and it decreases with time.

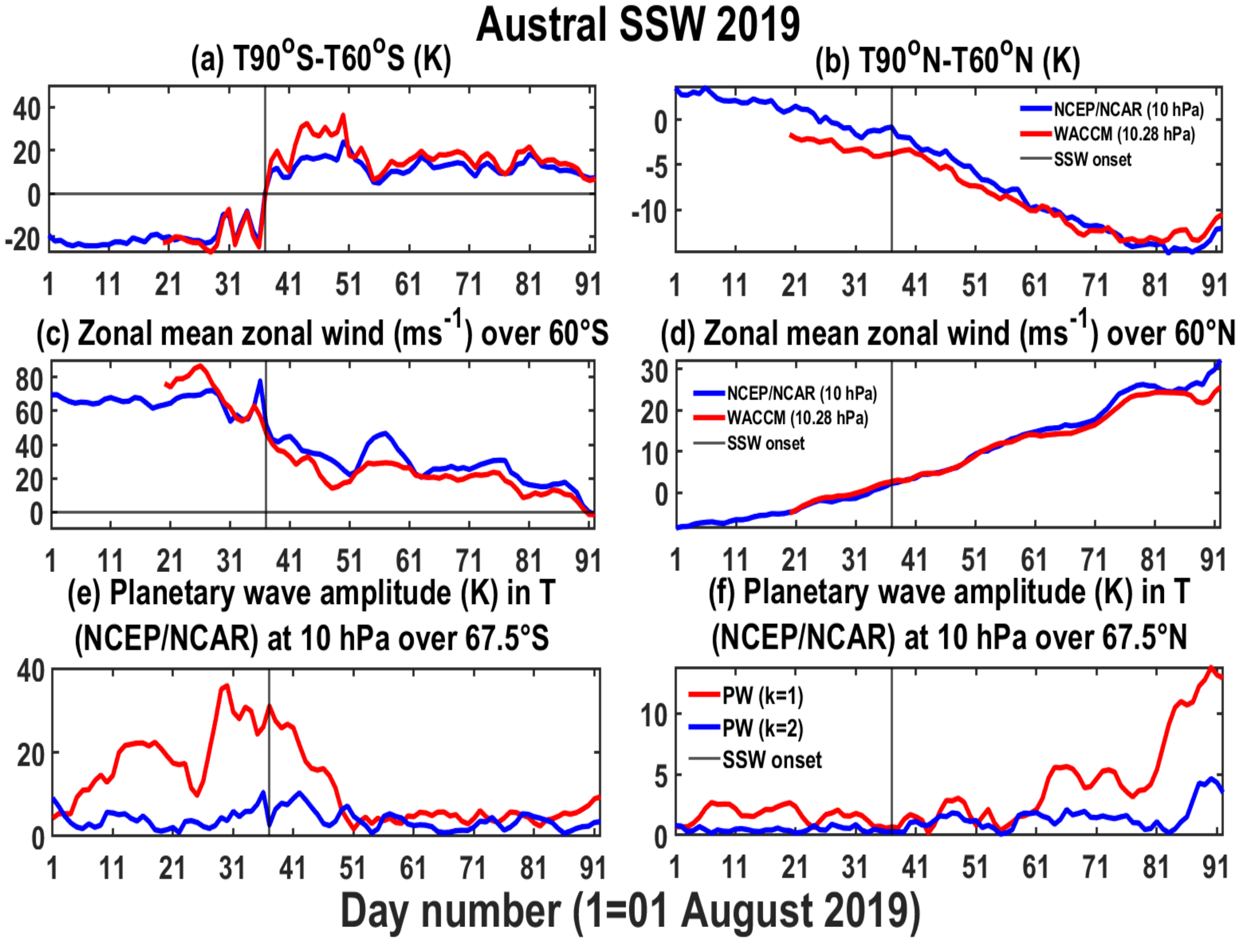

Figure 6.2: (a,b) Temperature difference between 90º and 60º latitude at 10 hPa, (b,d) zonal mean zonal wind at 60ºS and 60ºN and 10 hPa and, (e,f) planetary wave amplitude in temperature at 67.5ºS and 67.5ºN and 10 hPa for the days 1-92 starting from 01 August 2019

The zonal wind speed decreases from day number 36 or 05 September 2019 (78 m/s) to day number 37 or 07 September 2019 (43 m/s) as observed using NCEP/NCAR and day number 35 or 04 September 2019 (63 m/s) to day number 42 or 11 September 2019 (28 m/s) using WACCM (Figure 6.2 c). That is, wind reversal is not observed. Therefore, according to the definition of SSW provided by WMO, the austral SSW 2019 is a minor one. Unlike the boreal SSW of 2013, the change of wind direction from easterly to westerly in the opposite (northern) hemisphere is observed (Figure 6.2 d) prior to the SSW onset (day number 34 or 03 September 2019 for NCEP/NCAR and day number 32 or 01 September 2019 for WACCM).

In Figure 6.2 e, the PW (k=1) at 10 hPa shows a maxima on day number 30 or 30 August 2019 (36 K) and the PW (k=2) on day number 36 or 05 September 2019 (10 K). However, in the opposite polar hemisphere (Figure 6.2f), no significant PW activity is observed centering the SSW onset day.

6.3.3. UMLT solar and lunar semi diurnal tide during boreal SSW of 2013

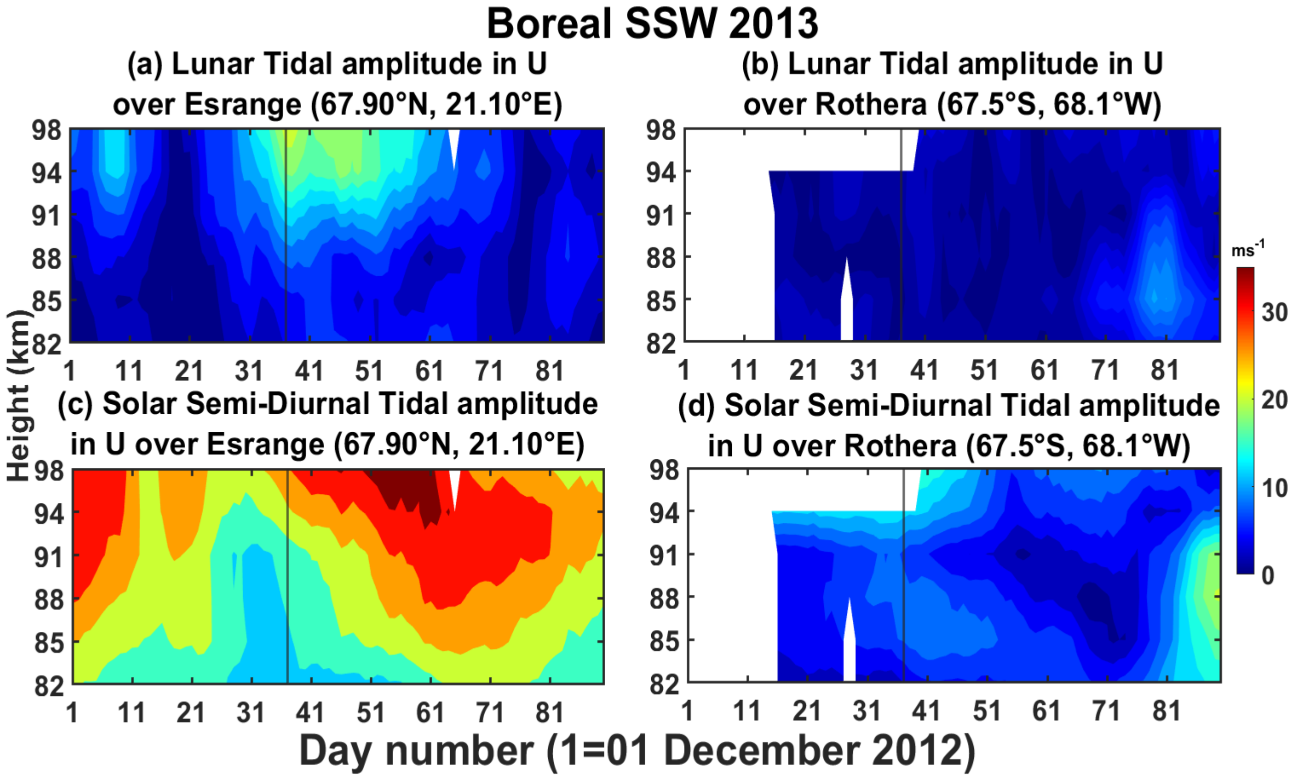

Figure 6.3: (a,b) Lunar and (c,d) solar semi-diurnal tidal amplitudes in zonal wind over (left panel) Esrange (67.9°N, 21.10°E) and (right panel) Rothera (67.5°S, 68.1°W) for the days 1-90 starting from 01 December 2012

Next, to identify the effects of SSW on the UMLT tides, the variability of solar SDT (12 h) and lunar (12.42 h) tides in zonal wind is investigated using a 30-day window (shifted by 1 day) during boreal SSW 2013 (Figure 6.3) and austral SSW 2019 (Figure 6.4). During the occurrence of the boreal SSW, an increase (11-21 m/s) in the amplitude of the lunar tide above 91 km is observed over Esrange (Figure 6.3 a). Although in the opposite hemisphere (Rothera), no notable changes in lunar tidal amplitude is observed (Figure 6.3 b).

In comparison to the lunar tides, the amplitude of the solar semi-diurnal tides (SDT) is observed to be larger over Esrange. In fact, there is an increase in the SDT amplitude over Esrange from day number 36 or 05 January 2013 to day number 60 or 29 January 2013 (27 m/s to 60 m/s), and it is shifted to lower heights with time (Figure 6.3 c). In the opposite hemisphere (Rothera), some large amplitude is observed between 82-91 km for solar tides around the SSW onset day (~9-10 m/s) and also after day number 83 or 21 February 2013 (~10-20 m/s) (Figure 6.3 d).

6.4.4. UMLT solar and lunar semi diurnal tide during austral SSW of 2019

In Figure 6.4 a, an increase of lunar tidal amplitude is observed over Rothera during the austral SSW onset day, however the amplitude appears to be weaker (5–7 m/s) compared to that in 2013. For SDT amplitude, the increase is restricted to above 91 km (Figure 6.4 c).

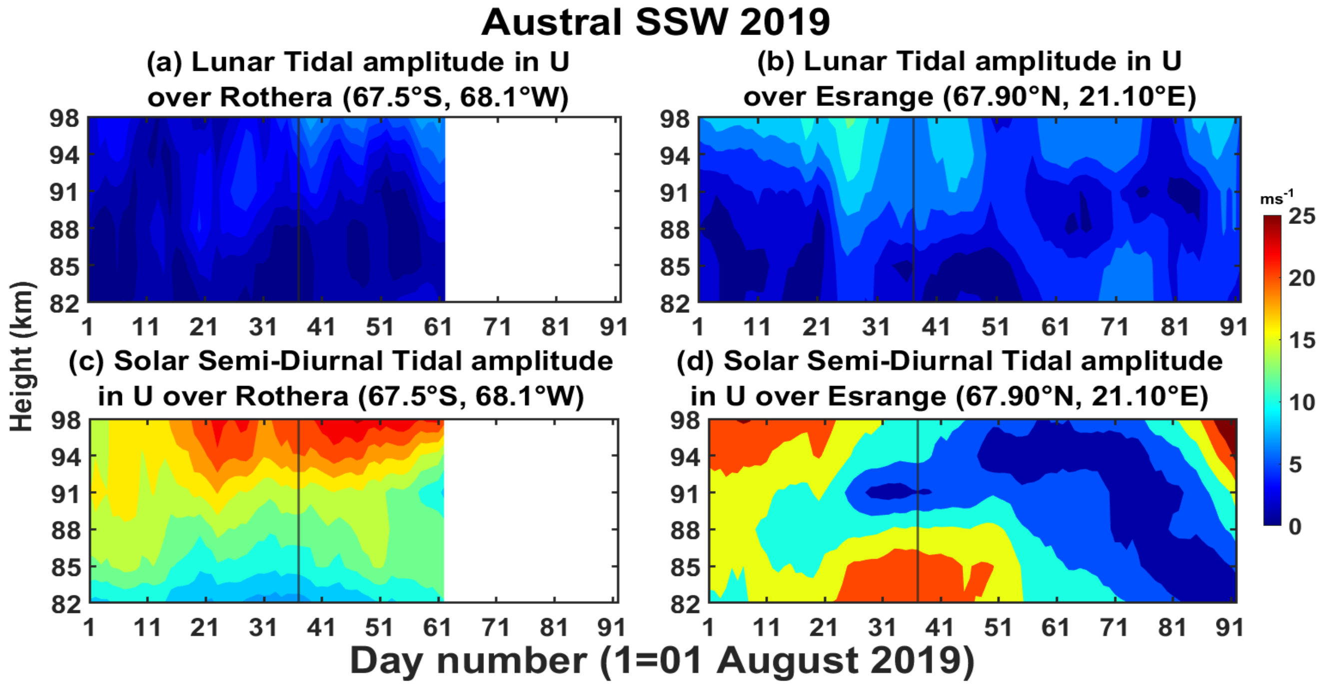

Figure 6.4: (a,b) Lunar and (c,d) solar semi-diurnal tidal amplitudes in zonal wind over (right panel) Esrange (67.9°N, 21.10°E) and (left panel) Rothera (67.5°S, 68.1°W) for the days 1-92 starting from 01 August 2019

The lunar tide in the opposite hemisphere (Esrange) shows large values (7–12 m/s) before and after the SSW onset day (Figure 6.4 b), but it appears to be less than that of SDT. The SDT shows an increase in its amplitude (24 m/s) below 88 km around the austral SSW onset time (day number 23 or 23 August 2019 to day number 47 or 16 September 2019) and also after day number 82 or 21 October 2019 above 91 km (Figure 6.4 d).

6.3.5. Variation of PW and tides in UMLT region during boreal SSW of 2013

Since, the solar SDT mostly appears to be the dominant component in the UMLT winds, we aim to investigate further the variation of solar SDT and PW (2-31 days) in connection to the boreal (Figure 6.5) and austral (Figure 6.6) SSWs in both the hemispheres using spectral analysis of 5-day composite mean winds at 88km.

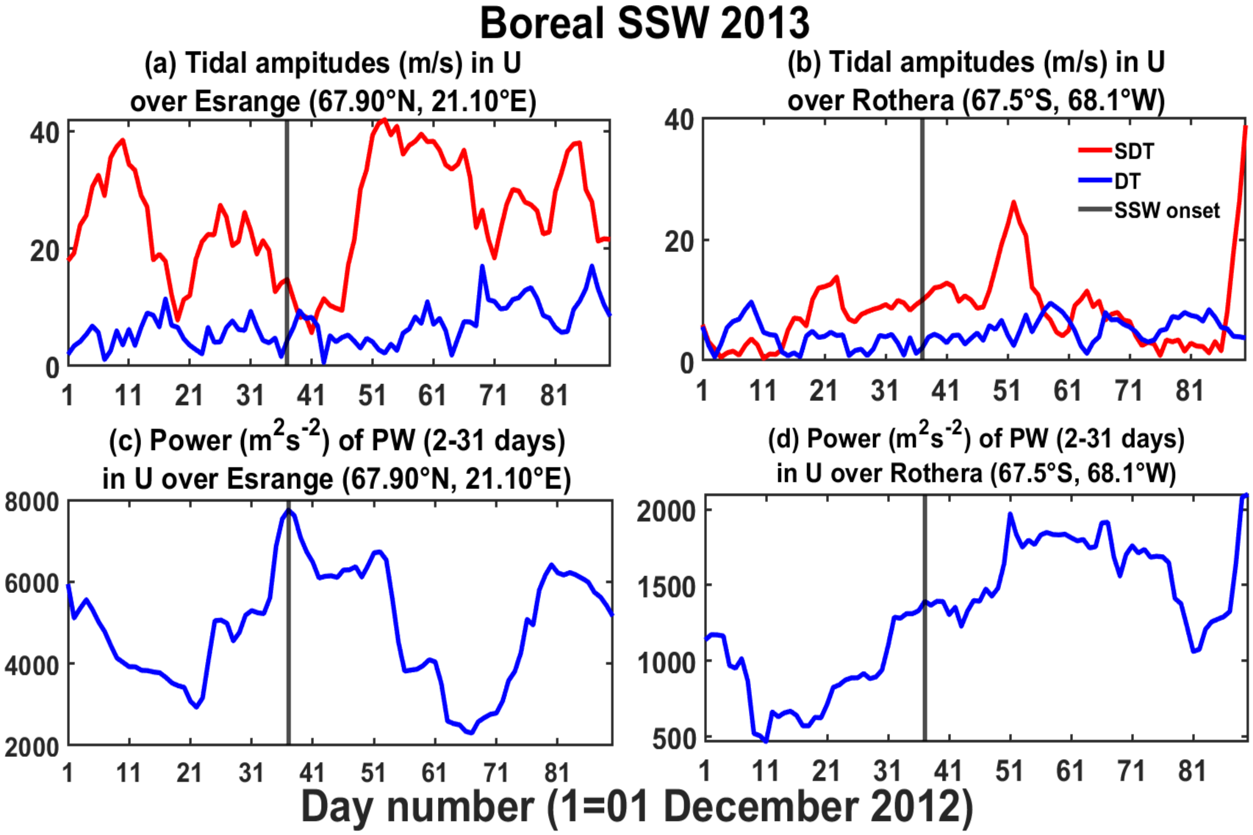

Figure 6.5: Tidal amplitude from harmonic analysis and (c,d) planetary wave (2-31 days) variance over (left panel) Esrange (67.9°N, 21.10°E) and (right panel) Rothera (67.5°S, 68.1°W) at 88 km for the days 1-90 starting from 01 December 2012

The SDT (red line) shows a decreased amplitude (15 m/s) over Esrange during boreal SSW onset day (Figure 6.5 a). However, it peaks during before (day number 10 or 10 December 2012, day number 26 or 26 December 2012) and after the SSW (day number 53 or 22 January 2013, day number 74 or 12 February 2013, day number 86 or 24 February 2013). The DT (blue line) shows a little increase (9 m/s) in its amplitude after the SSW onset day (day number 39 or 08 January 2013) but has smaller amplitude compared to the SDT. The PW activity (Figure 6.5 c) at the UMLT heights also increases (~2932 m^2s^{-2}) from day number 22 (22 December 2012), becomes maximum (7750 m^2s^{-2}) on day number 37 (06 January 2013) and it maintains its large value (6730 m^2s^{-2}) till day number 52 (21 January 2013).

6.3.6. Variation of PW and tides in UMLT region during austral SSW of 2019

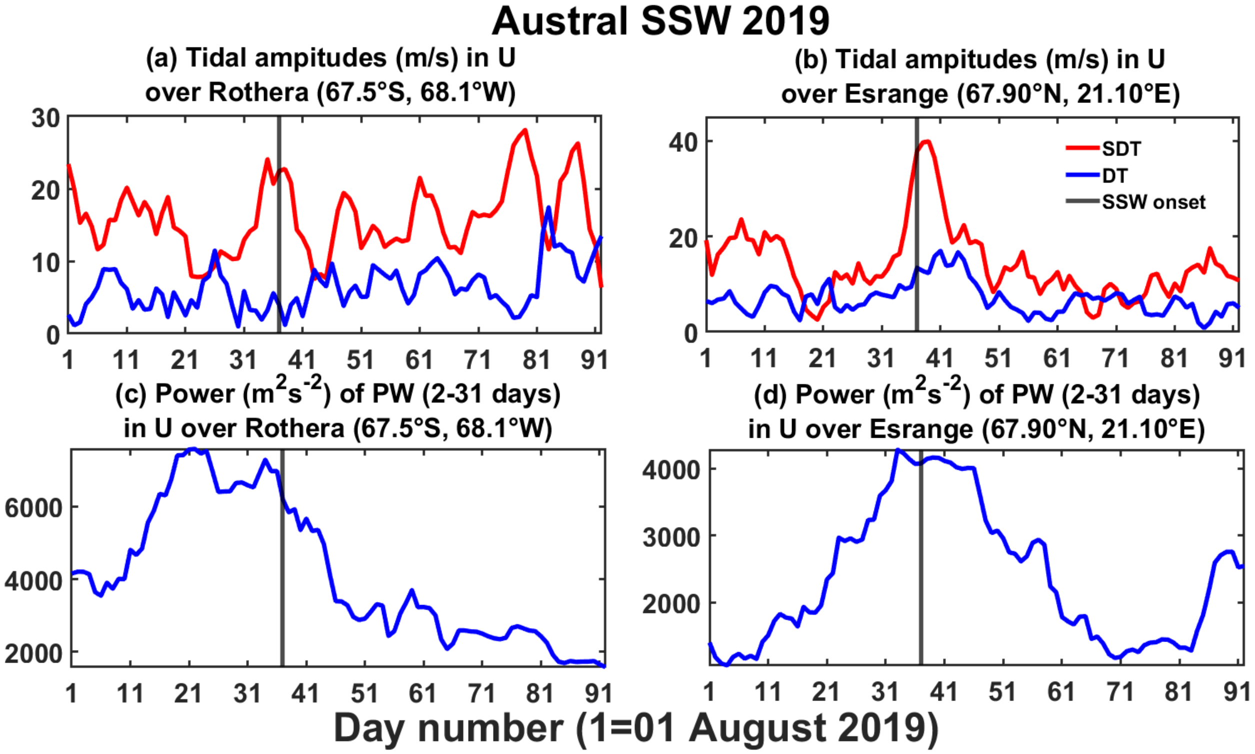

Figure 6.6: (a,b) Tidal amplitude from harmonic analysis and (c,d) planetary wave (2-31 days) variance over (right panel) Esrange (67.9°N, 21.10°E) and (left panel) Rothera (67.5°S, 68.1°W) at 88 km for the days 1-92 starting from 01 August 2019

However, the SDT amplitude over Rothera during the boreal SSW (Figure 6.5 b) exhibits a unique feature. It shows no significant variation near to the SSW onset day, but, a small peak (26 m/s) is observed on day number 52 (21 January 2013), followed by an increased amplitude after day number 86 or 24 February 2013 (8 to 39 m/s). The DT amplitude do not show any significant changes. The PW activity over Rothera (Figure 6.5d) is found to gradually increase much before the SSW onset day and it becomes maximum (2997 m^2s^{-2}) on day number 51 (20 January 2013), featuring a commonality in peaks as observed in SDT on 21 January 2013.

In Figure 6.6, an amplitude of ~24 m/s in SDT (Figure 6.6 a) is observed over Rothera (day number 35-38 or 4-7 September 2019) during the austral SSW. The PW activity (Figure 6.6 c) increases and shows a maximum value (~7588 m^2s^{-2}) on day number 22 (22 August 2019), and then starts to decrease from day number 34 or 03 September 2019.

Similar to the SDT peak over Rothera, a peak (40 m/s on day number 39 or 28 September 2019) is observed over Esrange just after the austral SSW onset day (Figure 6.6 b), but with a comparatively larger amplitude. This peak of the SDT also coincides with the increased value (4280 m^2s^{-2} to 4006 m^2s^{-2}) observed in the PW activity from day number 33 (02 September 2019) to day number 46 (15 September 2019) as observed in Figure 6.6 d. The DT amplitude (Figure 6.6 b) also shows large amplitudes around the SSW onset day, much similar to the peak of SDT, but after two days (day number 41 to 44).

6.3.7. Zonal winds, SDT and their relation with stratospheric ozone during boreal SSW event of 2013

In order to understand what causes the SDT enhancement in the opposite polar UMLT region during the SSW events, the possible modulation of PW periods in the tidal amplitudes and stratospheric ozone variations are investigated. The wavelet spectra of zonal wind and SDT amplitude in zonal wind at 88 km, and the ozone vmr variation (100-1 hPa) are presented in Figure 6.7. The spectra (Figure 6.7 a,c) indicate the presence of 20-25 day periodicity in both zonal wind as well as SDT amplitude at 88 km indicating the possible modulation of SDT amplitude by the PW of 20–25 days. Two other periodicities, 8–14 days and 4–6 days are observed in the zonal winds. The ozone vmr over 67.5° N (Figure 6.7 e) shows an increased value (6–7 ppmv) from 6 to 1 hPa starting from day number 71 or 09 February 2013, the time when the SDT amplitude peak is observed (Figure 6.5 a).

Over Rothera, both zonal wind and SDT amplitude in zonal wind exhibit 8–14 day periodicity for about 10 days centered around the SDT peak day (day number 52 or 21 January 2013) (Figures 6.7 b, d). This 8–14 day periodicity over Rothera (Figure 6.7 d) is similar to that observed in zonal wind over Esrange (Figure 6.7 c). However, ozone vmr over Rothera does not show any enhancement when the SDT peak is observed (Figure 6.7 f) revealing that it is unlikely to contribute for the increase in the SDT.

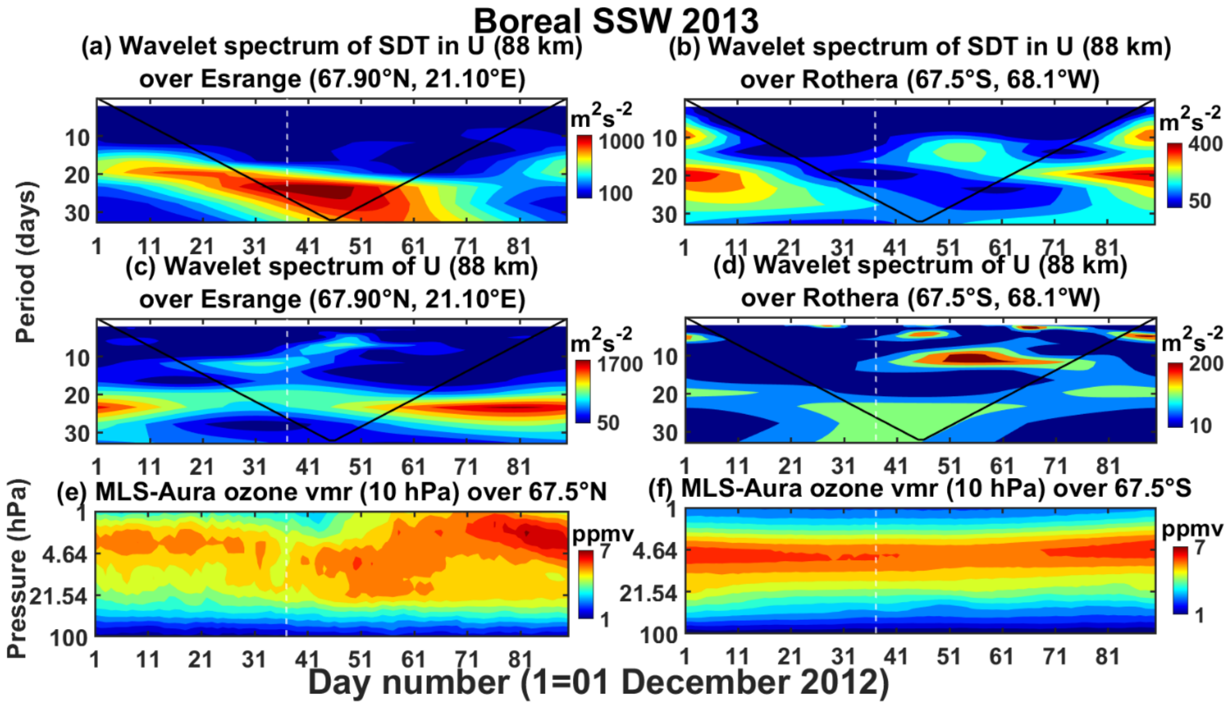

Figure 6.7: (a,b) Wavelet spectra of semi-diurnal tide in zonal wind and (c,d) zonal wind at 88 km. (e,f) Altitude time cross section of ozone volume mixing ratio (vmr) in MLS-Aura over (left panel) Esrange (67.9°N, 21.10°E) and (right panel) Rothera (67.5°S, 68.1°W) for the days 1-90 starting from 01 December 2012. The black line represents the cone of influence (COI) and the vertical white line represent the SSW onset day

6.3.8. Zonal winds and SDT and their relation with stratospheric ozone during austral SSW event of 2019

During the austral SSW, the wavelet spectrum of zonal wind over Rothera reveals the dominant presence of 8–14 day periodicity (Figure 6.8 c). However, SDT amplitude over Rothera shows longer periodicity of 19–23 days (Figure 6.8 a) and another periodicity between 7–11 days. Ozone vmr shows the increased value from day number 31 (31 August 2019) between 21 and 2 hPa

(Figures 6.8 e,g), implying that it is unlikely to govern the SDT variability at upper mesospheric heights. Note that the ozone vmr value is less in the SD-WACCM model outputs.

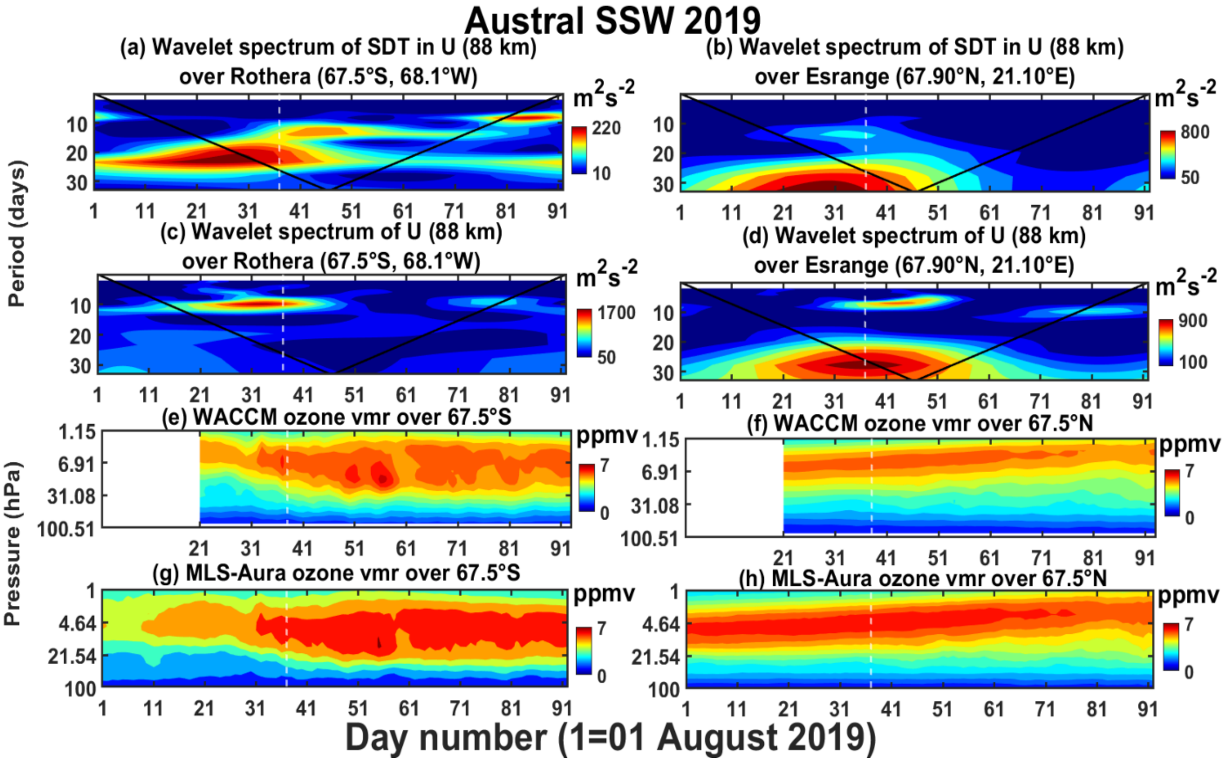

Figure 6.8: (a,b) Wavelet spectra of semi-diurnal tide in zonal wind and (c,d) zonal wind at 88 km. (e,f) Altitude time cross section of ozone vmr in WACCM and (g,h) MLS-Aura over (right panel) Esrange (67.9°N, 21.10°E) and (left panel) Rothera (67.5°S, 68.1°W) for the days 1-92 starting from 01 August 2019

Over Esrange, large periodicity of 23–33 days is observed in both zonal wind and SDT amplitudes (Figure 6.8 b,d) before and during the austral SSW onset day. Additionally, a periodicity of 7–11 days is observed in zonal winds during day number or 40–46 (9–15 September 2019) and for 9–14 days in SDT. This 7–11 day periodicity over Esrange (Figure 6.8 d) is somewhat similar to the 8–14 days periodicity as observed in Rothera (Figure 6.8 c). Although, the 23–33 day oscillation is in both the zonal wind and SDT amplitudes (Figure 6.8 b,d) is absent over Rothera (Figure 6.8 c). For ozone, (Figure 6.8 f, h) increased vmr is present in the height region 10–3 hPa till day number 76 (15 October 2019), whereas it does not show any remarkable enhancement when the SDT amplitudes are larger. Therefore, enhancement in the opposite polar SDT amplitudes associated with both the boreal and austral SSWs is suggested to be linked with PW modulation of tides and less likely to be associated with stratospheric ozone vmr changes.

6.4. Discussion

In this chapter, we have examined the impact of the SSW events on two opposite polar UMLT regions using the meteor wind radar data over Esrange and Rothera, one during the boreal SSW of 2013 and another during the austral SSW of 2019. The temperature data obtained from the NCEP/NCAR reanalysis product and WACCM model output shows the rapid amplification of the temperature gradient between 90º and 60º latitudes, indicating the onset of both SSWs. However, the NCEP/NCAR zonal mean zonal wind data exhibits wind reversal (westerly to easterly) for the boreal SSW of 2013, unlike the austral SSW of 2019, which only exhibits the deceleration of the westerly in the vortex. Hence, 2013 is considered as a major event, and 2019 as a minor one, as per the types of SSW defined by WMO. The dates of the SSW onset days are similar as mentioned in the previous studies (Coy et al. (2015), Liu et al. (2022)). In the antipodal stratosphere, latitudinal temperature difference is observed to decrease gradually and the stratospheric cooling is greater in magnitude for the 2019 SSW, compared to the 2013 event. This is mostly due to the seasonal variation. The boreal SSW occurred during January 2013, when there is summer in the southern hemisphere. Whereas the austral SSW occurred during September 2019 when the northern hemisphere transits from summer to winter seasons and is also an equinox month. This might have led to the colder temperature in the antipodal stratosphere during the 2019 SSW compared to that in 2013. The increase of the stratospheric PW, particularly PW (k=1), is also observed for both events. However, in the opposite hemispheres (67.5º S for boreal SSW and 67.5º N for austral SSW), no remarkable changes are observed in the PW activity at the SSW onset times. Although PW (k=1) increases some days after the SSW onset day.

Next, the tidal variability (12 h, 12.42 h) in the high latitude UMLT region in the same and opposite polar hemispheres is studied in connection to the SSWs. At northern high latitudes (Andøya (69.1° N) and Juliusruh (54° N)), Chau et al., (2015) have shown an increase in the lunar tidal amplitude in the total wind (30–50 m/s) at higher heights (above 91 km) much before the onset of boreal SSW 2009. In this study, we also observed a similar increase during the boreal SSW of 2013 but with a comparatively smaller amplitude (15–25 m/s). The SW2 amplitude variation obtained from total wind magnitude over Andøya (69.1° N) is also similar to the variation of SDT in zonal winds over Esrange (67 °N). Although, the SW2 amplitude showed a larger amplitude (>40 m/s) in comparison to the SDT amplitude (25–35 m/s) observed in this study. Conte et al. (2017) reported similar variability and amplitude of the lunar and solar SDT over Andenes (69° N) consistent with the lunar and solar tidal variability over Esrange (67.5° N) observed in this chapter. However, for the austral SSW of 2019, we observed no significant increase in lunar tide during the SSW event (unlike that in the case of boreal SSW of 2013) and for solar SDT it shows a large amplitude (20–25 m/s) (above 91 km) around the SSW onset day. This shows that that the lunar tidal amplitudes vary differently for different SSWs, unlike the solar SDT, which increases around the onset days during both the SSW events. Additionally, we also observed that the amplitude of the lunar tide during both the SSWs is much smaller (<20 m/s for boreal SSW and <10 m/s for austral SSW) than the solar SDT amplitude (25–35 m/s for boreal SSW and 20–25 m/s for austral SSW) in the same hemisphere. This indicates that the wind field is dominated by SDT when there is a SSW event.

In the opposite hemisphere, Conte et al. (2017) found an increase in the solar SDT amplitude using Davis meteor radar (67º S) and model simulations (TIMEGCM/WACCMX), some days after the onset of boreal SSW of 2013. In our study, we have also observed an increase of the solar SDT over Rothera (67.5º S) from the middle of February, more than one month after the onset of 2013 SSW, but with a smaller amplitude (<20 m/s). Some little (~9-10 m/s) enhancement in SDT is also observed around the SSW onset day. The difference may be attributed to the use of different meteor radars or partly because of the usage of a 21-day window of wind measurement used in their analysis and the 30-day window used in our study. However, we observed no significant variation of lunar tides around the SSW onset day, similar to the results of Conte et al. (2017). Next, for the austral SSW, the lunar tides (above 91 km) show some enhanced amplitude (~10 m/s) before and after the SSW onset day and for solar SDT (below 91 km) it is around the SSW onset day. This again indicates that in connection to the SSW events, there is no specific variation of lunar tides in the opposite UMLT region. However, an increase in the solar SDT amplitudes is observed over both hemispheres around the SSW onset days. Also in the antipodes, the SDT amplitudes are larger compared to the lunar tidal amplitudes, which implies that the wind field is mostly dominated by the solar SDT in both hemispheres during the SSW events.

Next, the daily variation of the solar tides is studied by extracting the tidal amplitudes of SDT and DT from the 5-day composite mean of zonal winds. The tidal variation and its relation with the upper mesospheric PW is also investigated during the SSWs. The SDT showed many peaks (both before and after) over Esrange during the 2013 boreal SSW event, however, there is no significant change on the onset day of SSW. Using Super Dual Auroral Radar Network (SuperDARN) observations (60^0 N) between 1995 and 2016 and NCAR CESM2.0 WACCM-x results between 2000 and 2014, Zhang et al. (2021) showed an amplification of the SW2 amplitude 10 days after the SSW onset day, but not during the onset time, which is quite similar to our result. This is in contrast with the 2019 austral SSW event, where a peak of the SDT is observed at the SSW onset time. This implies that there is no specific variation of SDT in the UMLT region around the SSW onset day. No concurrent ozone vmr changes are observed with the enhancement of the SDT amplitudes. For PW activity (2–31 days) at upper mesospheric heights, the peak power is observed to enhance gradually before the 2013 boreal SSW onset day and persisted till some days after the SSW onset day. Previously, Stray et al. (2015) observed enhancement of the PW of wavenumber 1 and 2 a few (~5) days at 95 km after the stratospheric wind reversal is observed by using eight SuperDARN radars during 2000-2008. Ma et al. (2017) reported the enhancement of Q2DW after the commencement of boreal SSW 2013 using wind data from Mohe (52.5° N, 122.3° E), Beijing (40.3° N, 116.2° E), Wuhan (30.5° N, 114.6° E), and Sanya (18.3° N, 109.6° E) meteor radars. The differences in the results can be attributed to the consideration of 2-31 days in this chaptery to define PW activity in the UMLT region. However, we have found that for the austral SSW, the PW activity enhanced much before and sustained up to the SSW onset day. Consistent with our results, Wang et al. (2021) observed an increase of Q10DW in the UMLT during the 2019 austral SSW onset time over Rothera (67.5° S) and McMurdo stations (77°5 S). Next, from the wavelet spectra, the presence of a 20–25 day periodicity in zonal winds and SDT amplitudes over Esrange in the UMLT region is confirmed. Therefore, the possible modulation of SDT amplitude by the PW over Esrange during the boreal SSW of 2013 is suggested. Modulation of tidal spectrum by PWs is now a well established fact (Forbes et al., (2018, 2020)). Beard et al. (1999) demonstrated that the non linear interaction between waves and tides can lead to the generation of a secondary wave having the frequency which is the sum or difference of the frequencies of the primary waves. Manson et al. (1982) first showed that a Q2DW and SDT can generate a 9.6-hr and 16-hr waves. Pancheva et al. (2003) also observed a 7-day periodicity in UMLT winds and sporadic E critical frequency (f_0Es) on a global scale and suggested that PW can indirectly affect the Es. They further explained that the tides (SDT and DT) which undergo PW modulation due to their non linear interactions with PW at heights below 100 km can play an important role in the formation of the Es layer. Similar to the boreal SSW, a 7–11 day periodicity is observed both in zonal winds and SDT amplitudes over Rothera during the 2019 austral SSW.

On the antipodes, a peak of the SDT is observed, a few days after the onset day of boreal SSW (26 m/s) and immediately after austral SSW (40 m/s), and is further investigated in detail. In the case of boreal SSW, the variation of PW activity and stratospheric ozone is checked in connection to the peak in the SDT, which appeared on 21 January 2013 over Rothera, followed by an abrupt increase in SDT amplitude after 24 February 2013. The ozone vmr does not show any increase during 21 January 2013 and, thus, is less likely to generate a peak in SDT amplitude during 21 January over Rothera. However, PW activity at 88 km shows an increase in amplitude concurrently with the SDT amplitude enhancement; particularly it increased one day before the peak observed in SDT. From the wavelet spectra of the zonal winds and SDT amplitude, it is found that both the wind and SDT amplitude over Rothera showed a similar range of periodicity 8–14 days during 20–21st January 2013, which indicates that the SDT might have been modulated by the PW over Rothera, a few days after the 2013 boreal SSW onset day. Again, for the austral SSW, the wavelet spectra over Esrange reveal the presence of similar periodicity (8–14 days) in both SDT amplitude and zonal wind again indicating the possibility of tidal modulation by PW over Esrange. Also, the PW activity shows an enhancement before the SDT amplitude increases. No significant ozone vmr changes is observed to be associated with the SDT peak over Esrange during the austral SSW.

Additionally, for the boreal SSW, a similar 8–14 days periodicity is observed over Esrange (as observed in Rothera also) prior to the SDT peak over Rothera and a periodicity of 7–11 days in zonal winds in both the hemispheres in case of the austral SSW. It is therefore suggested that the similar PW periodicity (8–14 days for boreal SSW and 7–11 days for austral SSW) observed in the zonal wind over both the hemispheres during the SSW events might have propagated from one hemisphere, where the SSW event occurred (northern for boreal SSW and southern for austral SSW) to the other (southern for boreal SSW and northern for austral SSW). The cross equatorial propagation of PW periodicity in the UMLT region is suggested to have modulated the SDT in the opposite hemisphere after the SSW events. This might have led to the enhancement of both PW and therefore SDT amplitudes in the antipodal UMLT region during both the SSW events. Previously, Day et al. (2011) observed the presence of 16-day PW in the mid and high latitude stratosphere and UMLT region. They suggested that the 16-day wave in the winter UMLT region is ducted across the equator to the summer hemisphere and is modulated by the westerly phased Quasi-Biennial Oscillation (QBO). The method has been also investigated using models (Miyahara et al. (1991), Forbes et al. (1995)) and observations (Epsy et al. (1997), Jacobi et al. (1998)). Previous studies have also provided the evidences of interhemispheric coupling using observations and global scale models (Liu and Robble. (2002), Iida et al. (2014), Laskar & Pallamraju, (2014), Körnich & Becker, (2010), Liu et al. (2013), Laskar et al. (2016), Laskar et al. (2019)). Although, modeling studies have shown different outcomes depending on the choice of the parameterization or forcing schemes. Laskar & Pallamraju, (2014) proposed an additional meridional circulation in neutrals in the mesosphere thermosphere region during the SSWs that extends from pole-to-pole. This circulation is opposite to the pole-to-equator circulation in the stratosphere and lower mesosphere as described in Andrews et al. (1987), p. 276. The role of this meridional circulation on the ionosphere thermosphere system is further discussed in Laskar et al. (2019). It is also observed that the SDT peak occurred immediately for austral SSW and a few days after boreal SSW. It can be attributed to the large value of PW activity observed before the austral SSW onset time compared to the boreal one, which showed a smaller value and also at a much later time. Results in this chapter therefore provide an observational evidence of the cross-equatorial propagation of the PW observed during the boreal and austral SSWs that can modulate the SDT amplitudes in the antipodal UMLT region.

Chapter 7: Summary and scope for future work

7.1. Summary

The thesis gives an overview of the global changes in the wind circulation and the amplitudes of waves of different scales mostly associated with two important polar middle atmospheric phenomena, viz., ozone hole and SSW. The ozone hole is mostly prevalent in the Antarctic and the SSWs are frequent over the Arctic. Until now, Antarctic witnessed SSW during the winters of 2002 and 2019.

Chapter 1 deals with the classification and description of different atmospheric layers based on the vertical thermal structure of the atmosphere, wind circulation pattern in lower and middle atmosphere, chemical composition and the variability of some important chemical constituents, description of major middle atmospheric events which are known to affect the global atmosphere and also the characteristics of the waves associated with it.

Specifications of the ground-based, space-borne instruments, reanalysis products and model outputs used in this thesis and their methodologies are discussed in Chapter 2.

Chapter 3 demonstrates the impact of stratospheric planetary waves on the polar middle atmospheric winds via the ozone loss processes occurring over Southern high latitudes during austral springtime. A term 'meridional heat flux' is calculated in this study, serves to act as a proxy for PW activity at stratospheric heights. It is observed that the years having low values of meridional heat flux during September, owing to PW of zonal wavenumber 1, decreases the polar stratospheric temperature. This reduced temperature subsequently enhances the formation of polar stratospheric clouds and facilitates enhanced stratospheric ozone loss over Southern high latitudes. Analysis of the long term (2005–2020) UMLT winds using meteor radar observations over Rothera reveals large westward wind anomaly (82-98 km) with high interannual variability during November–December of the years 2006-2011, 2015, 2018 and 2020, which are associated with large ozone loss in the Antarctic. Horizontal winds obtained from the ERA-5 reanalysis products also exhibit large interannual variability during October–November of those years, which altogether indicates a possible connection between the ozone loss and middle atmospheric winds. It is suggested that the years having large ozone loss leads to increased latitudinal temperature gradient and can cause large stratospheric eastward winds with height. The background eastward wind may therefore critically filter the upward propagating GWs and only allow the propagation of GWs having westward speed up to the UMLT heights. The westward phased GWs then deposit westward momentum into the background winds, while wave damping and result in the formation of large westward wind anomaly at UMLT heights. It is also observed that the SW2 tidal amplitude anomaly decreases in the years of larger ozone loss, which indicates that in addition to the winds, the Southern high latitude polar ozone loss processes also controls the SW2 tidal amplitudes at upper mesospheric heights.

In Chapter 4, we extended the study further to investigate the relative contribution of PWs, GWs and tides in driving the polar UMLT winds during summertime. In addition to meteor radar present over Rothera, data is also acquired from a similar meteor radar present on its opposite polar latitude, that is, over Esrange. This allows a direct comparison of winds, waves and tides in the polar UMLT region. It is observed that zonal winds are strongly westward during summer (April–September over Esrange and October–February over Rothera). The wind spectrum depicts the dominance of tides in comparison to PWs and GWs in the summer months. The seasonal variation of the SDT amplitudes shows an increase of its amplitudes with height, unlike the DT amplitude, which shows decrement in its value with height. The DW1 tidal mode obtained from SABER-TIMED temperature data exhibits summer enhancement in its amplitude similar to DT over both the polar latitudes, which implies that DT must be mostly composed of DW1. It is suggested that due to tidal mean flow interaction, DW1 tide, which is a westward propagating tide, can drive the large westward wind through its westward momentum deposition into the background flow. The PW and GW variances shows only winter enhancement and increase of the variances with height. Therefore, the PWs and GWs are unlikely drive the strong westward UMLT winds during summer.

The remaining half of the thesis discusses about the variable impact of the SSW events on the equatorial ionosphere and the UMLT tidal variabilities extending up to its antipode. To begin with, Chapter 5 portrays the possible connection between the austral SSW 2019 and the high occurrence of type-B 150-km radar echoes observed over Kototabang, Indonesia. The necklace shaped 150 km radar echoes, occurring only during daytime over low latitude valley region (130-170 km), are classified into type-A and type-B echoes depending on their SNR. The weaker SNR echoes that can occur independently are known as type-A echoes and the echoes showing stronger SNR values which are always embedded and superimposed in type-A echoes are known as type-B echoes. Because of its stronger SNR, type-B echoes can be observed even with low sensitive radars like Equatorial Atmosphere Radar (EAR) over Kototabang. The EAR observations shows a clear seasonal variation of the type-B echoes with a maximum occurrence observed during June-August and December-January (2016–2019). Moreover, the PO is observed to increase from solar moderate to solar minimum years, that is, from 2016 to 2019. Particularly anomalously high occurrence of these echoes are observed during September 2019 (76%), which includes an austral SSW event. The space–time spectral analysis of temperature data obtained in SABER-TIMED satellite reveals that SW2 tide is dominant during June–August, when the PO of the 150-km echoes is maximum, whereas DW1 tide is dominant during equinoxes. Quasi-biennial variability in DW1 tide is also observed probably due to the similar variability in stratospheric ozone. As per the Global Scale Wave Model (GWSM) results it is suggested that the solar insolation absorption of stratospheric ozone and tropospheric water vapor, generating the DW1 tide, has opposite phases. Additionally, the former acts to suppress the latter, which results in lesser value of DW1 tide in September 2017 and 2019, when the stratospheric ozone shows large concentrations. This might have led to the relative dominance of SW2 tide over DW1 tide in those years. The highest ozone concentration over the equatorial stratosphere and large SW2 amplitude during 2019 is also due to austral SSW event of 2019, which occurred during September. The reduction in the DW1 tide may also be due to its interaction with planetary waves, which normally enhances just before the onset of the SSW event. Therefore, it is suggested that the meridional wind shear associated with the increased SW2 tidal amplitude might have resulted in the interchange instability developed on the gradient of daytime descending ion layer along with solar minimum conditions giving rise to plasma irregularities responsible for the high PO of the type-B 150-km radar echoes during September 2019.

In addition to the effects of SSW that is observed over equatorial ozone and tidal variabilities, the impacts are also observed in the opposite hemispheres. Chapter 6 discusses about the tidal amplitude changes associated with one boreal (2013) and one austral (2019) SSW event. The two particular boreal and austral SSW are chosen because of the lack of continuous meteor radar wind observations during other SSWs. During both the SSW events, the dominance of solar SDT amplitudes is observed compared to the lunar amplitudes in both the hemispheres. The solar SDT shows an increase in amplitude in both the polar and the antipodal UMLT region around the onset day of the SSW events. This is in contrast with the lunar tide which exhibits an increase in its amplitude only in the boreal hemisphere. It shows a peak enhancement in its amplitude the opposite UMLT polar region a few days after the onset of the boreal SSW immediately after the austral

SSW event. PW activity at similar mesospheric heights also show increase of amplitude, prior to the SDT peaks. However, the enhancement of stratospheric ozone is not observed concurrent the SDT peak at the antipode. As the SDT amplitudes also reveal similar planetary wave periodicity as observed in zonal wind over both the poles, it is suggested that a cross-equatorial propagation of PW periodicity from one hemisphere to the other, which may results in the modulation of SDT activity in the antipodal UMLT region.

Briefly, Chapter 3 and 4 discuss the changes in the UMLT winds observed during austral springtime (related to ozone depletion process) and summer. Westward momentum deposition by GW and diurnal tides during springtime and summer, respectively, are considered to be responsible for driving the UMLT winds. Chapter 5 and 6 provides an observational evidence for the impact of SSW on the daytime equatorial valley region plasma irregularities and also on the antipodal UMLT tidal variabilities.

Limitations

In this thesis, the influence of polar atmospheric events on the wave and tides from high to low latitudes has been investigated using ground-based, space-borne, reanalysis and model output data. The propagation of tides from lower and middle atmosphere to the equatorial valley region has been suggested to generate plasma irregularities responsible for the formation of 150-km radar echoes. However, the lack of wind observations particularly between mesopause region and equatorial valley region of ionosphere makes it difficult to study the vertical propagation affecting the valley region irregularities. The link between the day-to-day variability in the echoes and the short-term tidal variability can only be studied with wind or temperature data with high temporal resolution at the equatorial valley region. Additionally, due to the lack of a network of observations, it is not possible to monitor latitudinal variation of tidal wave activity and the longitudinal structure of small period wave structures in the upper mesopause region. Satellite data can be used as a proxy for the same, although it has its own limitations like its lack of temporal resolution (hourly or sometimes daily at a particular point), which makes it difficult to study the short-period gravity waves and short-term variations in tidal activity.

7.2. Scope for the future work

The dominant drivers of the middle atmosphere are the GWs, PWs and tides. During propagation or dissipation, they can influence the background wind, temperature and chemical constituents present over there. This thesis has provided evidences of the vertical and horizontal coupling that affect the winds, waves and tides of the middle and upper atmosphere, starting from the role of upward propagating waves in controlling the polar UMLT winds to generating equatorial plasma irregularities. The results discussed here further opens up scope for investigating some scientific studies that can be followed in the near future.

The monthly wave activity in various vertical coupling processes between the lower and upper atmosphere has been investigated using meteor radar and satellite observations. Further, the day-to-day wave amplitudes extracted from ERA-5 wind and temperature data at different heights can be used to study the latitudinal coupling between low and high latitudes.

The possible relationship between the type-B 150-km echoes and UMLT tides are discussed in this thesis. Detailed investigations are required for understanding the role of solar minimum conditions on the occurrence of the type-A and type-B echoes. The role of waves and tides in generating the 150-km radar echoes on a day-to-day basis can be done using the GOLD (Global-Scale Observations of the Limb and Disk) satellite.

Simulation and modelling studies are essential for determining the role of both the Arctic and Antarctic ozone loss processes on the mesopause temperature as well as the UMLT circulation.

The role of tides in driving UMLT circulation has been observed at the polar latitudes. In addition to the observational evidences, the quantification of the tidal momentum deposition in the summer UMLT winds can be done using numerical simulations.

The increase in the occurrence of high latitude polar mesospheric cloud (PMC) and its spreading towards low latitudes is known to be associated with the anthropogenic increase in atmospheric methane (CH_4) and carbon dioxide (CO_2) owing to climate change. Therefore, the study of the connection between the formations of the PMC with the ozone loss processes can provide further insights of the impact of climate change in the upper atmosphere.

For SSW events, the effect on the polar UMLT winds via the upward propagating waves and tides needs further investigation, particularly for the austral hemisphere.

The long-term trend in the Brewer Dobson circulation and it association with both the Antarctic ozone hole and Arctic SSW events via the meridional transport can portray a clear picture of the impact of climate change in the middle atmosphere.

The impact of polar middle atmosphere in affecting the tropical climate is worth pursuing. Recent studies indicate the link between the stratospheric final warming with Arctic Oscillation and the relation between Arctic Oscillation and Indian Summer Monsson. Therefore, the teleconnections between the polar stratospheric final warming on the onset of Indian Summer Monsoon can be studied in details by observations and model simulations.

References

Andrews, D. G., J. R. Holton, and C. B. Leovy (1987), Middle Atmosphere Dynamics, 489 pp., Academic, San Diego, Calif.

Avery, S. K., Vincent, R. A., Phillips, A., Manson, A. H., and Fraser, G. J. (1989). High-latitude tidal behaviour in the mesosphere and lower thermosphere. Journal of Atmospheric and Solar-Terrestrial Physics, 51(7–8), 595–608.

Baldwin, M. P., Ayarzagüena, B., Birner, T., Butchart, N., Butler, A. H., Charlton-Perez, A. J., Domeisen, D. I. V., Garfinkel, C. I., Garny, H., Gerber, E. P., Hegglin, M. I., Langematz, U., and Pedatella, N. M. (2021). Sudden stratospheric warmings, Rev. Geophys., 59, e2020RG000708.

Bartels, J. (1926). “Barometrische Messung der Hochseegezeiten.”. Ann. Hydrogr., Berl., 54: 222–227, 270–273.

Balsley, B.B. (1964). Evidence of stratified echoing region at150 km in the vicinity of magnetic equator during daylight hours. J. Geophys. Res., 69, 1925–1930.

Beard, A.G., Mitchell, N.J., Williams, P.S., et al., (1999). Non-linear interactions between tides and planetary waves resulting in periodic tidal variability. J. Atmos. Sol. Terr. Phys. 61, 363–376.

Becker, E. (2017). Mean-flow effects of thermal tides in the mesosphere and lower thermosphere. Journal of the Atmospheric Sciences, 74(6), 2043–2063.

Beldon, C. L., and Mitchell, N. J. (2009). Gravity waves in the polar mesopause region observed by meteor radar. Journal of Atmospheric and Solar-Terrestrial Physics, 71(8–9), 875–884.

Bhattacharya, Y., Shepherd, G.G., and Brown, S. (2004). Variability of atmospheric winds and waves in the arctic polar mesosphere during a stratospheric warming. Geophysical Research Letters, 31, p. L23101.

Castanheira, J. M., and Barriopedro, D. (2010). Dynamical connection between tropospheric blockings and stratospheric polar vortex. Geophysical Research Letters, 37, L13809.

Charney, J. G., and Drazin, P. G. (1961). Propagation of planetary-scale disturbances from the lower into the upper atmosphere. Journal of Geophysical Research, (1896-1977), 66(1), 83–109.

Chau, J.L. (2004). Unexpected spectral characteristics of VHF radar signals from 150-km region over Jicamarca. Geophys, Res. Lett., 31, L23803.

Chau, J.L., and Kudeki, E. (2006). Statistics of 150-km echoes over Jicamarca based on low-power VHF observations. Ann. Geophys., 24, 1305–1310.

Chau, J., Fejer, B. G., and Goncharenko, L. (2009). Quiet variability of equatorial E x B drifts during a sudden stratospheric warming event. Geophysical Research Letters, 36.

Chau, J.L., and Kudeki, E. (2013). Discovery of two distinct types of equatorial 150-km radar echoes. Geophysical Research Letters, 40 (17), 4509– 4514.

Chau, J. L., Hoffmann, P., Pedatella, N. M., Matthias, V., and Stober, G. (2015). Upper mesospheric lunar tides over middle and high latitudes during sudden stratospheric warming events. Journal of Geophysical Research: Space Physics, 120(4), 3084–3096.

Cohen, J., and Jones, J. (2011). A new index for more accurate winter predictions. Geophysical Research Letters, 38(21), L21701.

Conte, J. F., Chau, J. L., Stober, G., Pedatella, N., Maute, A., Hoffmann, P., et al. (2017). Climatology of semidiurnal lunar and solar tides at middle and high latitudes: Interhemispheric comparison. Journal of Geophysical Research: Space Physics, 122, 7750–7760.

Conte, J. F., Chau, J. L., Laskar, F. I., Stober, G., Schmidt, H., and Brown, P. (2018). Semidiurnal solar tide differences between fall and spring transition times in the Northern Hemisphere. Annales Geophysicae, 36(4), 999–1008.

Coy, L., Nash, E.R., and Newman, P.A. (1997). Meteorology of the polar vortex: Spring 1997. Geophys. Res. Lett. 24, 2693–2696.

Coy Lawrence, and Steven Pawson (2015). The Major Stratospheric Sudden Warming of January 2013: Analyses and Forecasts in the GEOS-5 Data Assimilation System. Monthly Weather Review, 143(2), 491-510.

David, C., Bekki, S., Berdunov, N., Marchand, M., and Me´gie, G. (2005). Classification and scales of Antarctic polar stratospheric clouds using wavelet decomposition. J. Atmos. Sol. Terr. Phys., 67 (3), 293–300.

Day, K. A., Hibbins, R. E., and Mitchell, N. J. (2011). Aura MLS observations of the westward-propagating s=1, 16-day planetary wave in the stratosphere, mesosphere and lower thermosphere, Atmos. Chem. Phys., 11, 4149–4161.

Dempsey, S., Hindley, N., Moffat-Griffin, T., Wright, C., Smith, A., Du, J., and Mitchell, N. (2021). Winds and tides of the Antarctic mesosphere and lower thermosphere: One year of meteor-radar observations over rothera (68°S, 68°W) and comparisons with WACCM and eCMAM. Journal of Atmospheric and Solar-Terrestrial Physics, 212, 105–510.

Dempsey, S. M., Noble, P. E., Wright, C. J., Mitchell, N. J., and Moffat-Griffin, T. (2022). Interannual variability of the 12-hr tide in the mesosphere and lower thermosphere in 15 years of meteor-radar observations over Rothera (68°S, 68°W). Journal of Geophysical Research: Atmospheres, 127(22), e2022JD036694.

de Laat, A.T.J., Van Wheele, M. (2011). The 2010 Antarctic ozone hole: Observed reduction in ozone destruction by minor sudden stratospheric warmings, scientific reports. Nature 1–38.

de Wit, R.J., Hibbins, R.E., Espy, P.J., Orsolini, Y.J., Limpasuvan, V., and Kinnison, D.E. (2014). Observations of gravity wave forcing of the mesopause region during the January 2013 major Sudden Stratospheric Warming. Geophys. Res. Lett. 41, 4745–4752.

de Wit, R.J., Hibbins, R.E., Espy, P.J. (2015). The seasonal cycle of gravity wave momentum flux and forcing in the high latitude northern hemisphere mesopause region. J. Atmos. Sol. Terr. Phys. 127, 21–29.

Dowdy, A J., Vincent, R.A., Murphy, D.J., Tsutsumi, M., Riggin, D.M., and Jarvis, M.J. (2004). The large-scale dynamics of the mesosphere–lower thermosphere during the Southern Hemisphere stratospheric warming of 2002. Geophysical Research Letters, 31, p. L14102.

Engel, A., Strunk, M., Muler, M., Haase, H.-P., Poss, C., Levin, I., and Schmidt, U. (2002). Temporal development of total chlorine in the high latitude stratosphere based on reference distributions of mean age derived from CO2 and SF6. J. Geopys. Res., 107 (D12), 4136.

Espy, P. J., J. Stegman, G. Witt (1997). Interannual variations of the quasi-16-day oscillation in the polar summer mesospheric temperature, Journal of Geophysical Research, 102, pp. 1983-1990.

Fagundes, P. R., Goncharenko, L. P., de Abreu, A. J., Venkatesh, K., Pezzopane, M., de Jesus, R., et al. (2015). Ionospheric response to the 2009 sudden stratospheric warming over the equatorial, low- and mid-latitudes in the South American sector. Journal of Geophysical Research: Space Physics, 120, 7889–7902.

Farman, J.C., Gardiner, B.G., Shanklin, J.D. (1985). Large losses of total ozone in Antarctic reveal seasonal ClOx/NOx interaction. Nature 315, 207–210.

Forbes, J. M. (1995). Tidal and Planetary Waves, in The Upper Mesosphere and Lower Thermosphere: A review of Experiment and Theory, Geophysical Monograph, vol. 87, edited by R. M. Johnson and T. L. Killeen, pp. 67–87, American Geophysical Union.

Forbes, J. M., Hagan, M. E., Miyahara, S., Vial, F., Mason, A. H., Meek, C. E., and Portnyagin, Y. I. (1995). Quasi 16-day oscillation in the mesosphere and lower thermosphere, J. Geophys. Res., 100, 9149–9163.

Forbes, J.M., Wu, D. (2006). Solar Tides as Revealed by Measurements of Mesosphere Temperature by the MLS Experiment on UARS. J. Atmos. Sci. 63, 1776–1797.

Forbes, J.M., Zhang, X., Palo, S., Russell, J., Mertens, C.J., Mlynczak, M. (2008). Tidal variability in the ionospheric dynamo region. Journal of Geophysical Research: Space Physics, 113, A02310.

Forbes, J. M., Zhang, X., Maute, A., and Hagan, M. E. (2018). Zonally symmetric oscillations of the thermosphere at planetary wave periods. Journal of Geophysical Research: Space Physics, 123, 4110–4128.

Forbes, J. M., Zhang, X., and Maute, A. (2020). Planetary wave (PW) generation in the thermosphere driven by the PW-modulated tidal spectrum. Journal of Geophysical Research: Space Physics, 125(5).

Forster, F., Piers, M. D., and Shine, K. P. (1999). Stratospheric water vapour changes as a possible contributor to observed stratospheric cooling. Geophysical Research Letters, 26(21), 3309–3312.

Fritts, D. C., and Alexander, M. J. (2003). Gravity wave dynamics and effects in the middle atmosphere. Reviews of Geophysics, 41(1), 1003.

Fritts, D. C. and Rastogi, P. K. (1985). Convective and dynamical instabilities due to gravity wave motions in the lower and middle atmosphere: theory and observations. Radio Sci., 20, 1247–1277.

Fukao, S., Hashiguchi, H., Yamamoto, M., Tsuda, T., Nakamura, T., Yamamoto, M.K., Sato, T., Hagio, M., and Yabugaki, Y. (2003). Equatorial Atmosphere Radar (EAR): System description and first results. Radio Sci. 38 (3).

Garcia-Comas et al. (2008). Errors in sounding using broadband emission radiometry (SABER) kinetic temperature caused by non-local-thermodynamic equilibrium parameters. J. Geophys. Res. 113(D24).

Gardner, J.A., Viereck, R.A., Murad, E., Knecht, D.J., Pike, C.P., Broadfoot, A.L., and Anderson, E.R., (1995). Simultaneous observations of neutral and ionic magnesium in the thermosphere. Geophys. Res. Lett. 22 (16), 2119–2122.

Garfinkel CI, Hartmann DL, and Sassi F, (2010). Tropospheric precursors of anomalous Northern Hemisphere stratospheric polar vortices. J. Climate, 23, 3282–3299.

Goncharenko, L. P., Chau, J. L., Liu, H. L., and Coster, A. J. (2010). Unexpected connections between the stratosphere and ionosphere. Geophys. Res. Lett. 37.

Goncharenko, L.P., Coster, A.J., Plumb, R.A., Domeisen, D.I.V. (2012). The potential role of stratospheric ozone in the stratosphere-ionosphere coupling during stratospheric warmings. Geophy. Res. Lett. 39 (8).Goncharenko, L. P., Harvey, V. L., Randall, C. E., Coster, A. J., Zhang, S.-R., Zalizovski, A., Galkin, I., & Spraggs, M. (2022). Observations of Pole-to-Pole, Stratosphere-to-Ionosphere Connection. Frontiers in Astronomy and Space Sciences, 8.

Griffith, M. J., and Mitchell, N. J. (2022). Analysis of migrating and non-migrating tides of the Extended Unified Model in the mesosphere and lower thermosphere. Annales Geophysicae, 40(3), 327–358.

Hagan, M.E. (1996). Comparative effects of migrating solar sources on tidal signatures in the middle and upper atmosphere. J. Geophy. Res. 101 (D16), 21213–21222.

Hamilton K., Hertzog A., Vial F., and Stenchikov, G. (2004). Longitudinal variation of the stratospheric quasi-biennial oscillation. J. Atmos. Sci. 61, 383–402.

Hanson, W.B., Sterling, D.L., and Woodman, R.F. (1972). Source and identification of heavy ions in the equatorial F layer. J. Geophys. Res. 77 (28), 5530–5541.

Harper, R.M. (1977). Tidal winds in the 100to 200 km region at Arecibo. J. Geophys. Res. 82 (22), 3243–3250.

Hausler, K., Luhr, H., Hagan, M.E., Maute, A., and Roble, R.G. (2010). Comparison of CHAMP and TIME-GCM nonmigrating tidal signals in the thermospheric zonal wind. J. Geophys. Res. Atmos. 115.

Heelis, R.A. (1999). Ionization layers observed at middle latitudes by Atmosphere Explorer-C. J. Atmos. Solar. Terr. Phys. 61 (5), 407–414.

Hersbach, H., Bell, B., Berrisford, P., Hirahara, S., Hora´nyi, A., Mun˜oz-Sabater, J., et al. (2020). The ERA5 global reanalysis. Q. J. R. Meteorolog. Soc.

Hibbins, R.E., Shanklin, J.D., Espy, P.J., Jarvis, M.J., Riggin, D.M., Fritts, D.C., Lubken, F.-J., (2005). Seasonal variations in the horizontal wind structure from 0–100 km above Rothera station, Antarctica (67ºS, 68ºW), Atmos. Chem. Phys., 5, 2973–2980, 10.5194/acp-5-2973.

Hines, C., Adams, G., Brosnahan, J., Djuth, F., Sulzer, M., Tepley, C., & Baelen, J. V. (1993). Multi-instrument observations of mesospheric motions over Arecibo: Comparisons and interpretations. Journal of Atmospheric and Terrestrial Physics, 55(3), 241–287.

Hocking, W. K., and Thayaparan, T. (1997). Simultaneous and colocated observation of winds and tides by MF and meteor radars over London, Canada (43°N, 81°W), during 1994–1996. Radio Science, 32(2), 833–865.

Hocking, W. K., Fuller, B., & Vandepeer, B. (2001). Real-time determination of meteor-related parameters utilizing modern digital technology. Journal of Atmospheric and Solar-Terrestrial Physics, 63, pp.155-169.

Hoffmann, P., Singer, W., and Keuer, D. (2002). Variability of the mesospheric wind field at middle and arctic latitudes in winter and its relation to stratospheric circulation disturbances. Journal of Atmospheric and Solar-Terrestrial Physics, 64 (2002), pp. 1229-1240.

Hoffmann, P., Singer, W., Keuer, D., Hocking, W.K., Kunze, M., Murayama, Y. (2007). Latitudinal and longitudinal variability of mesospheric winds and temperatures during stratospheric warming events. J. Atmos. SolarTerrestrial Phys. 69, 2355–2366.

Holton, J. R., P. H. Haynes, M. E. McIntyre, A. R. Douglass, R. B. Rood, and Pfister, L. (1995). Stratosphere-troposphere exchange, Rev. Geophys., 33, 403–439.

Huck, P.E., McDonald, A.J., Bodeker, G.E., and Struthers, H. (2005). Interannual variability in Antarctic ozone depletion controlled by planetary waves and polar temperature. Geophys. Res. Lett. 32, L13819.

Iida, C., Hirooka, T., and Eguchi, N. (2014). Circulation changes in the stratosphere and mesosphere during the stratospheric sudden warming event in January 2009. Journal of Geophysical Research: Atmospheres, 119, 7104–7115.

Jacobi, Ch., Schminder, R., KMurschner, D. (1998). Planetary wave activity obtained from long-period (2–18 days) variations of mesopause region winds over Central Europe (52◦N, 15◦E). Journal of Atmospheric and Solar-Terrestrial Physics, 60, 81–93.

Jin, H., Miyoshi, Y., Pancheva, D., Mukhtarov, P., Fujiwara, H., and Shinagawa, H. (2012). Response of migrating tides to the stratospheric sudden warming in 2009 and their effects on the ionosphere studied by a whole atmosphere-ionosphere model GAIA with COSMIC and TIMED/SABER observations. Journal of Geophysical Research, 117(A10).

Jones, M. Jr., Forbes, J. M., Hagan, M. E., and Maute, A., (2013). Non-migrating tides in the ionosphere- thermosphere: In situ versus tropospheric sources. Journal of Geophysical Research: Space Physics. 118, 2438-2451.

Julian, P. R., and Labitzke, K. B. (1965). A study of atmospheric energetics during the January–February 1963 stratospheric warming. Journal of the Atmospheric Sciences, 22(6), 597– 610.

Kal’chanko, B. V. and Bulgakov, S. V. (1973). Study of periodic components of wind velocity in the lower thermosphere above the equator, Geomagn. Aeron., 13, 955–956, 1973.

Kalnay, E., and Coauthors (1996). The NCEP/NCAR 40-Year Reanalysis Project. Bull. Amer. Meteor. Soc., 77, 437–471.

Karlsson, B., Körnich, H., and Gumbel, J. (2007). Evidence for interhemispheric stratosphere-mesosphere coupling derived from noctilucent cloud properties. Geophysical Research Letters, 34, 16.

Sato, K., Hirano, S. (2019). The climatology of the Brewer–Dobson circulation and the contribution of gravity waves. Atmospheric Chemistry and Physics, 19 (7), 4517-4539.

Kishore, P., Namboothiri, S. P., Igarashi, K., Murayama, Y., Vincent, R. A., Dowdy, A., et al. (2003). Further evidence of hemispheric differences in the UMLT mean wind climatology: Simultaneous MF radar observations at Poker Flat (65°N, 147°W) and Davis (69°S, 78°E). Geophysical Research Letters, 30(6), 1336.

Kishore Kumar, G., and Hocking, W. K. (2010). Climatology of northern polar latitude UMLT dynamics: Mean winds and tides. Annales Geophysicae, 28(10), 1859–1876.

Kolstad, E. W., Breiteig, T., and Scaife, A. A. (2010). The association between stratospheric weak polar vortex events and cold air outbreaks in the Northern Hemisphere. Quarterly Journal of the Royal Meteorological Society, 136(649), 886–893.

Körnich, H., and Becker, E. (2010). A simple model for the interhemispheric coupling of the middle atmosphere circulation. Advances in Space Research, 45(5), 661–668.

Krall, J., Huba, J.D., Nossa, E., Aponte, N., Drob, D.P. (2020). SAMI3 Simulations of Ionospheric Metallic Layers at Arecibo. Journal of Geophysical Research: Space. Physics, 125 (3).

Krankowsky, D., Arnold, F., Wieder, H., Kissel, J. (1972). The elemental and isotopic abundance of metallic ions in the lower E-region as measured by a cryogenically pumped quadrupole mass spectrometer. International Journal of Mass Spectrometry and Ion Physics, 8(4), 379-390.

Kuttippurath, J., and Nikulin, G. (2012). A comparative study of the major sudden stratospheric warmings in the Arctic winters 2003/2004–2009/2010. Atmos Chem Phys, 12(17), 8115–8129.

Labitzke K, Kunze M (2009) On the remarkable Arctic winter in 2008/2009. J Geophys Res 114:D00I02.

Langematz, U., Kunze, M., Kruger, K., Labitzke, K., and Roff, G.L. (2003). Thermal and dynamical changes of the stratosphere since 1979 and their link to ozone and CO2 changes. J. Geophys. Res. 108 (D1), 4027.

Laskar, F.-I., and Pallamraju, D. (2014). Does sudden stratospheric warming induce meridional circulation in the mesosphere thermosphere system? Journal of Geophysical Research: Space Physics, 119, 10133–10143.

Laskar, F. I., Chau, J. L., Stober, G., Hoffmann, P., Hall, C. M., and Tsutsumi, M. (2016). Quasi-biennial oscillation modulation of the middle- and high-latitude mesospheric semidiurnal tides during August–September. Journal of Geophysical Research: Space Physics, 121(5), 4869–4879.

Laskar, F. I., McCormack, J. P., Chau, J. L., Pallamraju, D., Hoffmann, P., & Singh, R. P. (2019), Interhemispheric meridional circulation during sudden stratospheric warming. Journal of Geophysical Research: Space Physics, 124, 7112–7122.

Lehtonen, I., and Karpechko, A. Y. (2016). Observed and modeled tropospheric cold anomalies associated with sudden stratospheric warmings. Journal of Geophysical Research: Atmospheres, 121, 1591–1610.

Li, W., Huang, C., and Zhang, S. (2021). Global characteristics of the westward- propagating quasi-16-day wave with zonal wavenumber 1 and the connection with the 2012/2013 SSW revealed by ERA-Interim. Earth Planets Space 73, 113.

Lieberman, R. S., and Hays, P. B. (1994). An estimate of the momentum deposition in the lower thermosphere by the observed diurnal tide. Journal of the Atmospheric Sciences, 51(20), 3094–3105.

Lieberman, R.S., and Riggin, D., (1997). High resolution Doppler imager observations of Kelvin waves in the equatorial mesosphere and lower thermosphere. J. Geophy. Res. 102 (D22), 26117–26130.

Lieberman, R.S., Oberheide, J., and Talaat, E.R. (2013). Nonmigrating diurnal tides observed in global thermospheric winds. J. Geophy. Res. 118 (11), 7384–7397.

Lim, E.-P., Hendon, H. H., Boschat, G., Hudson, D., Thompson, D. W. J., Dowdy, A. J., and Arblaster, J. M.(2019). Australian hot and dry extremes induced by weakenings of the stratospheric polar vortex. Nature Geoscience, 12(11), 896–901.

Limpasuvan, V., Orsolini, Y. J., Chandran, A., Garcia, R. R., and Smith, A. K. (2016). On the composite response of the UMLT to major sudden stratospheric warming events with elevated stratopause. Journal of Geophysical Research: Atmospheres, 121(9), 4518–4537.

Lin, Y.-L. (2007). Mesoscale dynamics, Cambridge University Press, Cambridge. xv, 13.

Lin, C., Lin, J., Chang, L., Chen, W., Chen, C., and Liu, J. (2013). Stratospheric sudden warming effects on the ionospheric migrating tides during 2008–2010 observed by FORMOSAT-3/COSMIC. Journal of Atmospheric and Solar-Terrestrial Physics, 103, 66–75.

Lindzen, R.S. (1972). Equatorial Planetary Waves in Shear. Part II. J. Atmos. Sci. 29 (8), 1452–1463.

Liu, H., Jin, H., Miyoshi, Y., Fujiwara, H., and Shinagawa, H. (2013). Upper atmosphere response to stratosphere sudden warming: Local time and height dependence simulated by GAIA model. Geophysical Research Letters, 40, 635–640.

Liu, H.-L., and R. G. Roble (2002). A study of a self-generated stratospheric sudden warming and its mesospheric–lower thermospheric impacts using the coupled TIME-GCM/CCM3, J. Geophys. Res., 107(D23), 4695.

Liu, J., Zhang, D.-H., Hao, Y.-Q., and Xiao, Z. (2019). The comparison of lunar tidal characteristics in the low-latitudinal ionosphere between east asian and American sectors during stratospheric sudden warming events: 2009–2018. J. Geophys. Res. Space Phys. 124, 7013–7033.

Liu, G., Hirooka, T., Eguchi, N., and Krüger, K. (2022). Dynamical evolution of a minor sudden stratospheric warming in the Southern Hemisphere in 2019. Atmos. Chem. Phys., 22, 3493–3505.

Livesey, N. J., Read, W. G., Wagner, P. A., Froidevaux, L., Lambert,A., Manney, G. L., Millán, L. F., Pumphrey, H. C., Santee, M. L., Schwartz, M. J., Wang, S., Fuller, R. A., Jarnot, R. F., Knosp, B. W., and Martinez, E. (2017). Earth Observing System (EOS), Aura Microwave Limb Sounder (MLS), Version 4.2x Level 2 data quality and description document, Version 4.2x-3.0, D-33509, Jet Propulsion Laboratory, California Institute of Technology, Pasadena, California.

Longley, W.J., Oppenheim, M.M., Pedatella, N.M., Dimant, Y.S. (2020). The photoelectron-driven upper hybrid instability as the cause of 150-km echoes. Geophysical Research Letters 47.

Lossow, S., McLandress, C., Jonsson, A.I., Shepherd, T.G. (2012). Influence of the Antarctic ozone hole on the polar mesopause region as simulated by the Canadian middle atmosphere model. J. Atmos. Solar Terr. Phys. 74, 111–123.

Lubis, S. W., Omrani, N. E., Matthes, K., & Wahl, S. (2016). Impact of the Antarctic ozone hole on the vertical coupling of the stratosphere-mesosphere-lower thermosphere system. Journal of the Atmospheric Sciences, 73(6), 2509–2528.

Luo, Y., Manson, A. H., Meek, C. E., Meyer, C. K., Burrage, M. D., Fritts, D. C., Hall, C.M., Hocking, W.K., MacDougall, J., Riggin, D. M., Vincent, R. A. (2002). The 16-day planetary waves: multi-MF radar observations from the arctic to equator and comparisons with the HRDI measurements and the GSWM modelling results. Ann Geophys 20(5),691–709.

Ma, Z., Gong, Y., Zhang, S., Zhou, Q., Huang, C., Huang, K., et al. (2017). Responses of quasi 2 day waves in the UMLT region to the 2013 SSW revealed by a meteor radar chain. Geophysical Research Letters, 44, 9142–9150.

MacLeod, R., & Vincent, R. A. (1985). Observations of winds in the Antarctic summer mesosphere using the spaced antenna technique. Journal of Atmospheric and Terrestrial Physics, 47(6), 567–574.

Manson, A. H., Meek, C. E., Gregory, J. B., & Chakrabarty, D. K. (1982). Fluctuation in tidal (24-, 12-h) characteristics and oscillations (8-h-5-d) in the mesosphere and lower thermosphere (70-110 km): Saskatoon (52°N, 107°W), 1979-1981. Planetary and Space Science, 30, 1283–1294.

Manson, A. H., Meek, C., Chshyolkova, T., McLandress, C., Avery, S.K., Fritts, D.C., Hall, C.M., Hocking, W.K., Igarashi, K., MacDougall, J.W., Murayama, Y., Riggin, D.C., Thorsen, D., and Vincent, R.A. (2006). Winter warmings, tides and planetary waves: comparisons between CMAM (with interactive chemistry) and MFR-MetO observations and data. Annales de Geophysicae, 24, 2493-2518.

Marsh, D. R., Mills, M.J., Kinnison, D.E., Lamarque, J.-F., Calvo, N., and Polvani, L.M. (2013). Climate change from 1850 to 2005 simulated in CESM1(WACCM). J. Clim., 26, pp. 7372-7391.

Martius, O., Polvani, L. M., and Davies, H. C. (2009). Blocking precursors to stratospheric sudden warming events. Geophysical Research Letters, 36, L14806.

Maruyama, T., Kawamura, M., Saito, S., Nozaki, K., Kato, H., Hemmakorn, T., et al., (2007). Low latitude ionosphere-thermosphere dynam-ics studies with ionosonde chain in Southeast Asia. Annales Geophysicae 25, 1569–1577.

McLandress, C., Jonsson, A.I., Plummer, D.A., Reader, M.C., Scinocca, J.F., Shepherd, T.G. (2010). Separating the dynamical effects of climate change and ozone depletion. Part I: Southern hemisphere stratosphere. J. Clim. 23, 5002–5020.

Mitchell, N. J., Pancheva, D., Middleton, H. R., and Hagan, M. E. (2002). Mean winds and tides in the arctic mesosphere and lower thermosphere. Journal of Geophysical Research, 107(A1), SIA21214.

Mitchell, N., and Beldon, C. (2009). Gravity waves in the mesopause region observed by meteor radar: 1. A simple measurement technique. Journal of Atmospheric and Solar-Terrestrial Physics, 71(8–9), 866–874.

Miyahara, S. (1978a). Zonal mean winds induced by vertically propagating atmospheric tidal waves in the lower thermosphere: Part II. Journal of the Meteorological Society of Japan. Series II, 56(6), 548–558.

Miyahara, S. (1978b). Zonal mean winds induced by vertically propagating atmospheric tidal waves in the lower thermosphere. Journal of the Meteorological Society of Japan. Series II, 56(2), 86–97.

Miyahara, S., Portnyagin, Y. I., Forbes, J. M., & Solovjeva, T. V. (1991). Mean zonal acceleration and heating of the 70- to 100-km region, J. Geophys. Res., 96, 1225–1238.

Miyahara, S., and Miyoshi, Y. (1997). Migrating and nonmigrating atmospheric tides simulated by a middle atmosphere general circulation model. Advances in Space Research, 20(6), 1201–1207.

Mohanakumar, K. (2008), Stratosphere Troposphere Interactions: An Introduction, Springer, New York.

Molina, M.J., Rowland, F.S. (1974). Stratospheric sink for chlorofluoromethanes: Chlorine atomic-catalysed destruction of ozone. Nature 249, 810–812.

Molina, L. T., and M. J. Molina, (1987). Production of chlorine oxide (Cl2O2) from the self-reaction of the chlorine oxide (ClO) radical. J. Phys. Chem., 91, 433–436.

Montzka, S.A., Butler, J.H., Myers, R.C., Thompson, T.M., Swanson, T. H., Clarke, A.D., Lock, L.T., Elkins, J.W. (1996). Decline in the tropospheric abundance of halogen from halocarbons: implications for stratospheric ozone depletion, Science, 272, 1318-1322.

Morton, Y. T., Mathews, J. D., and Zhou, Q. (1993). Further evidence of a 6-h tide above Arecibo, J. Atmos. Terr. Phys., 55(3), 459-465.

Muller, H. G., and Nelson, L., (1978). A travelling quasi 2-day wave in the meteor region, J. Atmos. Terr. Phys., 40 (1978), pp. 761-766.

Newman, P.A., Gleason, J.F., McPeters, R.D., Stolarski, R.S., (1997). Anomalously low ozone over the Arctic. Geophys. Res. Lett. 24, 2689– 2692.

Newman, P.A., Nash, E.R., Kawa, S.R., Montzka, S.A., and Schauffler, S.M. (2006). When will the Antarctic ozone hole recover? Geophys. Res. Lett. 33 (12).

Oberheide, J., Forbes, J.M., HAusler, K., Wu, Q., Bruinsma, S.L. (2009). Tropospheric tides from 80 to 400 km: Propagation, interannual variability, and solar cycle effects. J. Geophys. Res.: Atmos., 114.

Oppenheim, M.M., Dimant, Y.S. (2016). Photoelectron-induced waves: A likely source of 150km radar echoes and enhanced electron modes. Geophysical Research Letters 43, 3637–3644.

Pancheva, D., Haldoupis, C., Meek, C. E., Manson, A. H., and Mitchell, N. J. (2003). Evidence of a role for modulated atmospheric tides in the dependence of sporadic E on planetary waves. Journal of Geophysical Research, 108(A5), 1176.

Pancheva, D., Mukhtarov, P. (2011). Atmospheric Tides and Planetary Waves: Recent Progress Based on SABER/TIMED Temperature Measurements (2002-2007), Springer Netherlands, Dordrecht, pp. 19- 56.

Pancheva, D., Mukhtarov, P., Hall, C., Meek, C., Tsutsumi, M., Pedatella, N., et al. (2020). Climatology of the main (24-h and 12-h) tides observed by meteor radars at Svalbard and Tromsø: Comparison with the models CMAM-DAS and WACCM-x. Journal of Atmospheric and Solar-Terrestrial Physics, 207, 105339.

Patra, A.K. (2011). Descending ion layer property in the Gadanki radar observations of 150-km echoes and its implication to the echoing phenomenon. J. Geophys. Res. 116 (A11).

Patra, A.K., Chaitanya, P.P., Tiwari, D. (2011). Characteristics of 150 km echoes linked with solar eclipse and their implications to the echoing phenomenon. J. Geophys. Res. 116, A05319.

Patra, A. K., Chaitanya, P. P. (2014). Comparative anatomy of the dayand night-time radar echoes from the 130–170 km region of the low latitude ionosphere, Adv. Space Res.

Patra, A.K., Chaitanya, P.P.,. St.-Maurice, J.-P., Otsuka, Y., Yokoyama, T., and Yamamoto, M., (2017). The solar flux dependence of ionospheric 150 km radar echoes and implications. Geophys. Res. Lett. 44, 11257–11264.

Patra, A.K., Chaitanya, P.P., Rao, M.D., Reddy, G.J. (2020). On the Type-A and Type-B 150-km Radar Echoes. J. Geophys. Res. 125.

Paulino, A. R., Batista, P. P., Clemesha, B. R., Buriti, R. A., & Schuch, N. (2012). An enhancement of the lunar tide in the UMLT region observed in the Brazilian sector during 2006 SSW. J. Atmos. Solar-Terrestrial Phys. 90–91, 97–103.

Pavan Chaitanya, P., Patra, A.K., Otsuka, Y., Yokoyama, T., Yamamoto, M. (2018). On the solstice maxima and azimuth-dependent characteristics of the 150-km echoes observed using the Equatorial Atmosphere Radar. J. Geophy. Res. Space Physics 123 (8), 6752–6759.

Pedatella, N. M., Liu, H.-L., Richmond, A. D., Maute, A., and Fang, T.-W. (2012). Simulations of solar and lunar tidal variability in the mesosphere and lower thermosphere during sudden stratosphere warmings and their influence on the low-latitude ionosphere, J. Geophys. Res., 117, A08326.

Pedatella, N. M., Liu, H.-L., Sassi, F., Lei, J., Chau, J. L., and Zhang, X. (2014). Ionosphere variability during the 2009 SSW: Influence of the lunar semidiurnal tide and mechanisms producing electron density variability. Journal of Geophysical Research: Space Physics, 119(5), 3828–3843.

Pedatella, N. M., Chau, J. L., Vierinen, J., Qian, L., Reyes, P. M., Kudeki, E., et al. (2019). Solar flare effects on 150-km echoes observed over Jicamarca: WACCM-X simulations. Geophysical Research Letters, 46, 10,951–10,958.

Pyle, John A., James Keeble, Nathan Luke Abraham, Martyn P. Chipperfield, Paul T. Griffiths, (2022). Integrated ozone depletion as a metric for ozone recovery, Nature, 608, 7924, (719-723).

Quiroz, R. S. (1977). The tropospheric–stratospheric polar vortex breakdown of January 1977. Geophys. Res. Lett., 4, 151–154.

Rao, J., Garfinkel, C.I., Chen, H., White, I.P. (2019). The 2019 new year stratospheric sudden warming and its real-time predictions in multiple S2S models. J. Geophys. Res.: Atmos. 124 (21), 11155–11174.

Riggin, D. M., Meyer, C. K., Fritts, D. C., Jarvis, M. J., Murayama, Y., Singer, R. A. V., and Murphy, D. J. (2003). MF radar observations of seasonal variability of semidiurnal motions in the mesosphere at high northern and southern latitudes. Journal of Atmospheric and Solar-Terrestrial Physics, 65(4), 483–493.

Reyes, P., (2012). Solar flare effects observed over Jicamarca during MSTISR experiments (Master of Science, University of Illinois at UrbanaChampaign). Retrieved from http://hdl.handle.net/2142/31196.

Reyes, P.M., Kudeki, E., Lehmacher, G.A., Chau, J.L., Milla, M.A. (2020). VIPIR and 50 MHz radar studies of gravity wave signatures in 150-km echoes observed at Jicamarca. J. Geophys. Res. Space Phys. 125.

Roy, R., and Kuttippurath, J. (2022). The dynamical evolution of Sudden Stratospheric Warmings of the Arctic winters in the past decade 2011–2021. SN Appl. Sci. 4, 105.

Russell, J.M., III, Mlynczak, M.G.,Gordley, L. Tansock Jr. J.J., Esplin, R.W. (1999). Overview of the SABER experiment and preliminary calibration results, Proc. SPIE,3756, Optical Spectroscopic Techniques and Instrumentation for Atmospheric and Space Research III, (20 October 1999).

Salby, M.L., Titova, E.A., Deschamps, L. (2012). Changes of the Antarctic ozone hole: controlling mechanisms, seasonal predictability, and evolution. J. Geophys. Res. 117(D10), D10111.

Sandford, D. J., Beldon, C. L., Hibbins, R. E., & Mitchell, N. J. (2010). Dynamics of the Antarctic and Arctic mesosphere and lower thermosphere – Part 1: Mean winds. Atmospheric Chemistry and Physics, 10(21), 10273–10289.

Shu, J., Tian, W., Hu, D., Zhang, J., Shang, L., Tian, H., and Xie, F. (2013). Effects of the quasi-biennial oscillation and stratospheric semiannual oscillation on tracer transport in the upper stratosphere. Journal of the Atmospheric Sciences, 70(5), 1370–1389.

Sinnhuber, B.-M., Weber, M., Amankwah, A., and Burrows, J.P. (2003). Total ozone during the unusual Antarctic winter of 2002. Geophys. Res. Lett. 30 (11), 1580.

Siskind, D. E., Sassi, F., Randall, C. E., Harvey, V. L., Hervig, M. E., and Bailey, S. M. (2015). Is a high-altitude meteorological analysis necessary to simulate thermosphere-stratosphere coupling? Geophysical Research Letters, 42(19), 8225–8230.

Smith, C. A., Haigh, J. D., and Toumi, R. (2001). Radiative forcing due to trends in stratospheric water vapour. Geophys Res Lett 28(1):179–182.

Smith, A.K., Garcia, R.R., Marsh, D.R., Kinnison, D.E., Richter, J.H. (2010). Simulations of the response of mesospheric circulation and temperature to the Antarctic ozone hole. Geophys. Res. Lett. 37, L22803.

Smith, A. K. (2012). Interactions between the lower, middle and upper atmosphere. Space Sci. Rev., 168, 1–21.

Solomon, S., R. R. Garcia, F. Rowland, and D. J. Wuebbles, (1986). On the depletion of Antarctic ozone. Nature, 321, 755–758.

Solomon, S. (1999). Stratospheric ozone depletion: a review of concepts and history Rev. Geophys. 37 275–316.

Son, S.-W. et al., (2010). Impact of stratospheric ozone on southern hemisphere circulation change: A multimodel assessment. J. Geophys. Res., 115, D00M07.

Sridharan, S., Sathishkumar, S., Gurubaran, S. (2009). Variabilities of mesospheric tides and equatorial electrojet strength during major stratospheric warming events. Ann. Geophys. 27 (11), 4125–4130.

Sridharan, S., Sathishkumar, S., Gurubaran, S., (2012). Variabilities of mesospheric tides during sudden stratospheric warming events of 2006 and 2009 and their relationship with ozone and water vapour. J. Atmos. Sol.-Terr. Phys. 78–79, 108–115.

Sridharan, S. (2017). Variabilities of low-latitude migrating and nonmigrating tides in GPS-TEC and TIMED-SABER temperature during the sudden stratospheric warming event of 2013. J. Geophys. Res.: Space. Physics 122 (10), 10,748–10,761.

Sridharan, S. (2019). Seasonal variations of low-latitude migrating and nonmigrating diurnal and semidiurnal tides in TIMED-SABER temperature and their relationship with source variations. Journal of Geophysical Research: Space Physics, 124(5), 3558–3572.

Sridharan, S. (2020). Equatorial upper mesospheric mean winds and tidal response to strong El Niño and La Niña. Journal of Atmospheric and Solar-Terrestrial Physics, 202, 105270.

Stening, R. J., Forbes, J. M., Hagan, M. E., and Richmond, A. D. (1997). Experiments with a lunar atmospheric tidal model. J. Geophys. Res. 102 (D12), 13465–13471.

Stolarski, R.S., Cicerone, R.J. (1974). Stratospheric chlorine: a possible sink for ozone. Can. J. Chem. 52, 1610.

Stolarski, R.S., Douglass, A.R., Gupta, M., Newman, P.A., Pawson, S., Schoeberl, M.R., Nielsen, J.E. (2006). An ozone increase in the Antarctic summer stratosphere: a dynamical response to the ozone hole. Geophys. Res. Lett. 33, L21805.

Stray, N. H., Orsolini, Y. J., Espy, P. J., Limpasuvan, V., and Hibbins, R. E. (2015), Observations of planetary waves in the mesosphere-lower thermosphere during stratospheric warming events, Atmos. Chem. Phys., 15, 4997–5005.

Teitelbaum, H., and Vial, F. (1981). Momentum transfer to the thermosphere by atmospheric tides. Journal of Geophysical Research, 86(C10), 9693–9697.

Thayaparan, T., Hocking, W. K., and J. MacDougall (1995), Middle atmospheric winds and tides over London, Canada (43°N,81°W) during 1992-1993, Radio Sci., 30, 1293-1309.

Thompson, D. W. J., Baldwin, M. P., and Solomon, S. (2005). Stratosphere-troposphere coupling in the Southern Hemisphere. Journal of the Atmospheric Sciences, 62, 708–715.

Truskowski, A.O., Forbes, J.M., Zhang, X., Palo, S., (2014). New perspectives on thermosphere tides: 1. lower thermosphere spectra and seasonal-latitudinal structures. Earth, Planets and Space 66 (1), 136.

Tsuda, T., Kato, S., and Vinent, R. A. (1988). Long period wind oscillations observed by the Kyoto meteor radar and comparisons of the quasi-2-day wave with Adelaide HF radar observations, J. Atmos. Terr. Phys., 50, 225–230, 1988.

Tsunoda, R.T., and Ecklund, W.L. (2004). On a summer maximum in the occurrence frequency of 150 km (F1) radar echoes over Pohnpei. Geophys. Res. Lett. 31 (6).

Tung, K. K., and Lindzen, R.S. (1979a), A theory of stationary wave, part I: A simple theory of blocking,Mon. Wea. Rev.,107: 714–734.

Varotsos, C., (2002). The Southern Hemisphere Ozone Hole Split in 2002. ESPR – Environ. Sci. Pollut. Res. 9, 375–376.

Venkateswara Rao, N., Espy, P.J., Hibbins, R.E., Fritts, D.C., and Kavanagh, A.J., (2015). Observational evidence of the influence of Antarctic stratospheric ozone variability on middle atmosphere dynamics. Geophys. Res. Lett., 42, 7853–7859.

Wang, H., Boyd, J.P., Akmaev, R.A. (2016). On computation of Hough functions. Geosci. Model Dev. 9, 1477–1488.

Waugh, D.W., and Randel, W.J., (1999). Climatology of Arctic and Antarctic polar vortices using elliptical diagnostics. J. Atmos. Sci. 56, 1594–1613.

Woollings, T., Charlton-Perez, A., Ineson, S., Marshall, A. G., and Masato, G. (2010). Associations between stratospheric variability and tropospheric blocking. Journal of Geophysical Research, 115, D06108.

Wu, Q., Chen, Z., Mitchell, N., Fritts, D., Iimura, H., (2013). Mesospheric wind disturbances due to gravity waves near the Antarctica Peninsula. J. Geophys. Res.: Atmos. 118, 7765–7772.

Xu, X., Manson, A.H., Meek, C.E., Jacobi, C., Hall, C.M., and Drummond, J. R. (2011). Verification of the mesospheric winds within the Canadian Middle Atmosphere Model Data Assimilation System using radar measurements. J. Geophys. Res. 116, D16108.

Yamazaki, Y., Richmond, A., & Yumoto, K. (2012). Stratospheric warmings and the geomagnetic lunar tide: 1958–2007, Journal of Geophysical Research: Space Physics (1978–2012), 117.

Wang, J. C., Palo, S. E., Forbes, J. M., Marino, J., Moffat-Griffin, T., and Mitchell, N. J. (2021). Unusual quasi 10-day planetary wave activity and the ionospheric response during the 2019 southern hemisphere sudden stratospheric warming. Journal of Geophysical Research: Space Physics, 126(6).

Zhang, J., Limpasuvan, V., Orsolini, Y. J., Espy, P. J., and Hibbins, R. E. (2021). Climatological westward-propagating semidiurnal tides and their composite response to sudden stratospheric warmings in SuperDARN and SD-WACCM-X. J. Geophys. Res.Atmosphere, 126(3).

Zhang, J., Orsolini, Y.J., Limpasuvan, V. et al. (2022). Impact of the Pacific sector sea ice loss on the sudden stratospheric warming characteristics. npj Clim Atmos Sci 5, 74.

Zurek, R.W., Manney, G.L., Miller, A.J., Gelman, M.E., Nagatani, R.M., (1996). Interannual variability of the north polar vortex in the lower stratosphere during the UARS mission Geophys. Res. Lett. 23, 289– 292.